ABSTRACT

Title of Document: AERODYNAMIC ANALYSIS OF AN MAV-SCALE CYCLOIDAL ROTOR SYSTEM USING A STRUCTURED OVERSET RANS SOLVER

Kan Yang, Master of Science, 2010

Directed By: Dr. James D. Baeder, Associate Professor, Department of Aerospace Engineering

A compressible Reynolds-Averaged Navier-Stokes solver was used to investigate the performance and flow physics of the cycloidal rotor (cyclocopter). This work employed a computational methodology to understand the complex aerodynamics of the cyclocopter and its relatively unexplored application for MAVs. The numerical code was compared against performance measurements obtained from experiment and was seen to exhibit reasonable accuracy. With validation of the flow solver, CFD predictions were used to gain qualitative insight into the flowfield. Time histories revealed large periodic variations in thrust and power. In particular, the virtual camber effect was found to significantly influence the vertical force time history. Spanwise thrust and flow visualizations showed a highly three-dimensional flowfield with large amounts of blade shedding and blade-vortex interaction. Overall, the current work seeks to provide unprecedented insight into the cyclocopter flowfield

with the goal of developing an accurate predictive tool to refine the design of future cyclocopter configurations.

Aerodynamic Analysis of an MAV-Scale Cycloidal Rotor System Using a Structured Overset RANS Solver

by

Kan Yang

Thesis submitted to the Faculty of the Graduate School of the
University of Maryland at College Park in partial fulfillment
of the requirements for the degree of
Master of Science
2010

Advisory Committee:

Dr. James D. Baeder, Chairman/Advisor
Dr. Inderjit Chopra
Dr. Kenneth Yu

Dedication

To my parents and stepparents, without whom none of this would be possible.

Acknowledgements

I am incredibly grateful to my advisor, Dr. James Baeder, who has been consistently supportive throughout the course of this work, and from whom I have received so much invaluable academic advice over the past two years. He has helped steer me from confusion and uncertainty as a fresh Bachelors graduate to direction and confidence in my ability to conduct research. With his guidance, I feel much more prepared to tackle obstacles in my future career path, and I feel privileged to have been his student.

I am also extremely indebted to Vinod for his immeasurable help and advice over the past two years. Through thick and thin in the "dark" days of my research, and even during the countless times when I suffered lapses in judgment and asked unreasonable questions, he has always shown an incredible amount of patience in dealing with my problems. I hold him in the highest academic regard and wish him all the best with his professorship; I am certain that he will inspire students for years to come.

I would like to thank Moble, who at every step along the way has helped me to clarify my doubts and better understand my research topic. I also express deep gratitude to Shreyas, who has assisted me with my work and provided excellent suggestions in matters concerning both academia and life. I would like to show appreciation for my committee members Dr. Yu and Dr. Chopra in providing valuable recommendations to help improve my thesis. In addition, I am extremely grateful to Dr. Winkelmann for his wisdom, good humor, and kindness during my first semester at Maryland.

To Aisa, Amie, Christian, and Mary: though we may be separated by vast

distances, your warmth and spirit have kept me going over the past two years. I honestly could not ask for better friends. May and Eddie, who I have known the longest: thank you for all the wonderful memories. You both have helped define such a significant part of who I am. Sebastian, Pranay, Shivaji and Taran: I am incredibly glad to have met all of you, and your friendship has enriched my life here at Maryland. Evan, Sonia, Scott, Jared, Erica, and Jesse: thank you for being such fantastic roommates, and for putting up with my quirks. You have made coming home everyday something I really look forward to. Also, I thank Chen, Mor, Graham, Mel, Brandon, Ben, Ananth, Tim, Kayla, Ron, Andrei, Yashwant, Erika, and Ramya for their camaraderie, support, and incredible generosity.

Finally, I must thank my father, mother, stepfather, and stepmother for all the compassion and love that they have given me. Since childhood, their devotion and encouragement has always been the backbone from which I could grow and strive for my dreams. Without them, I would not be where I am today.

Table of Contents

List of Tables

List of Figures

Nomenclature

a	Speed of sound (m/s)
b	Diameter of the rotor cage (m)
c	Chord length of the airfoil (m)
C_d	Drag coefficient
C_l	Lift coefficient
C_m	Moment coefficient
d	Distance from the wall in Spalart-Allmaras equation
e	Internal energy
f_x, f_y, f_z	Body forces in the Cartesian directions
H	Stagnation enthalpy per unit volume, given by $e + p$
J	Jacobian of the Cartesian to computational coordinate transformation
k	Reduced frequency for a pitching airfoil, defined as $k = \frac{\omega c}{2V_\infty}$
k_c	Coefficient of thermal conductivity
k_{rot}	Rotational frequency for the cyclocopter
M_∞	Freestream Mach number
M_{rot}	Mach number corresponding to rotational speed
p	Pressure (Pa), given by $p = (\gamma - 1)\left\{e - \frac{1}{2}\rho\left(u^2 + v^2 + w^2\right)\right\}$
q	non-dimensionalized second invariant of the velocity gradient tensor, $\frac{\partial u_i}{\partial x_j}\frac{\partial u_j}{\partial x_i}$ (normalized by rotational speed and blade chord)
R	Radius of the rotor cage (m)
Re	Reynolds Number
$s\left(\xi\right)$	Vinokur grid distribution in an arbitrary computational

	coordinate direction, ξ
t	time
T	Temperature, given by $T = \frac{p}{\rho R}$
T_{DU}	Rotation matrix for prescribing structural deformations
T_x	Sidewise Force (grams)
T_y	Vertical Force (grams)
$u_V(\xi)$	Vinokur stretching function in an arbitrary computational coordinate direction, ξ
u, v, w	Velocity components in Cartesian directions
$\underline{u}, \underline{v}, \underline{w}$	Linear deflections in the radial, tangential, and spanwise directions
$\underline{u}', \underline{v}'$	Derivatives for the u, v deflections
V_∞	Freestream total velocity (m/s)
x, y, z	Cartesian coordinates
α	Angle of attack (degrees)
γ	Ratio of specific heats, $\gamma = 1.4$
$\Delta s_0, \Delta s_1$	Dimensionless grid spacings at two ends of Vinokur stretching function
Δt	Timestep size
Δz	Recursive solution to a Vinokur stretching function parameter
θ	Blade pitch (degrees)
μ	Laminar viscosity
ν_t	Turbulent viscosity
ξ, η, ζ	Computational coordinates
ξ_{max}	Maximum incrementation in the ξ coordinate direction
ρ	Density (kg/m^3)
τ_{ij}	Stress term in the ij direction

ϕ	Elastic torsional deformation
ϕ_e	Phase angle for the cyclocopter
ω	Rotational frequency (radians)
Ψ	Azimuthal angle or wake age (degrees)
Ψ_{B1}	Azimuthal angle of Blade 1 (degrees)
Ψ_{B2}	Azimuthal angle of Blade 2 (degrees)

Subscripts

B1	Refers to Blade 1
B2	Refers to Blade 2
max	Refers to the maximum incrementation or distance
rot	Pertains to rotation of the cyclocopter blades
∞	Refers to freestream conditions

Abbreviations

2-D	Two-dimensional
3-D	Three-Dimensional
BL	Baldwin-Lomax Turbulence Model
CFD	Computational Fluid Dynamics
CSD	Computational Structural Dynamics
CWT	Cycloidal Wind Turbine
DES	Detached Eddy Simulation
DNS	Direct Numerical Simulation
FEM	Finite Element Method

FM	Figure of Merit, the ratio of ideal power to actual power
IHC	Implicit hole-cutting
MAV	Micro Air Vehicle
RANS	Reynolds-averaged Navier-Stokes
SA	Spalart-Allmaras Turbulence Model
S-VAWT	Straight-Bladed Vertical Axis Wind Turbine
	(Also denoted in literature as a Straight Wing VAWT, or SW-VAWT)
TSR	Tip Speed Ratio
TURNS	Transonic Unsteady Rotor Navier-Stokes solver
VAWT	Vertical Axis Wind Turbine

Chapter 1

Introduction

1.1 Problem Statement

Since the 1930's, the commercial success of the conventional helicopter rotor has led to iteration after iteration of aerodynamic and structural improvements to optimize its design. Major advances over the last few decades in the understanding of helicopter aerodynamics through the use of new computational and experimental methods have allowed the conventional rotor to become highly efficient for full-scale flight vehicles. Recently, interest has been focused on applying rotor designs for use on Micro Air Vehicles (MAVs). The Defense Advanced Research Projects Agency (DARPA) defines MAVs as vehicles with a characteristic length no larger than 15 cm. (6 in.). Their small size proves attractive for missions such as military surveillance and reconnaissance, border patrolling, topographic mapping, environmental monitoring, and other military and civilian missions. Rotary-wing MAVs are particularly desirable over their fixed- and flapping-wing counterparts due to their ability to hover, quickly maneuver, and vertically take-off and land. In addition, such MAVs can be produced cheaply and in large quantities, thus making them more economically feasible to be used

in high-risk situations rather than larger UAVs or full-scale aircraft.

Rotary-wing MAV research occurs in a different flight regime than full-scale aircraft, and therefore is influenced by vastly different aerodynamic phenomena. The Reynolds number, defined as the non-dimensional ratio of inertial to viscous forces, is between 10,000 - 80,000 for Rotary-wing MAVs. This corresponds to a flow regime where viscous forces are relatively significant, thicker boundary layers result in higher viscous drag, and the flow is more susceptible to separation at low angles of attack. Since conventional rotors on full-scale helicopters are designed for Reynolds numbers on the order of 10^7, such designs cannot be simply scaled down for MAVs. Taking figure of merit (FM), the ratio of ideal power required to actual power required, as a metric for evaluating rotor aerodynamic efficiency, conventional rotors with $FM \approx 0.8$ at full-scale flight Reynolds numbers can only achieve $FM \approx 0.4$ or less at MAV-scale Reynolds numbers. Even with optimization of the rotor design for this flight regime, the optimal FM that can be achieved with a conventional rotor design is ~ 0.6. Thus, there has been increased investigation recently of unconventional rotor designs for MAVs. One such design is the cycloidal rotor, essentially a "horizontal axis rotary wing."

1.1.1 Definition of a Cycloidal Rotor System

A cycloidal rotor system (used synonymously in the current work with the term "cyclocopter") is a propulsive mechanism that consists of several blades rotating parallel to the rotational, or z-axis, as shown in Figure 1.1. In this schematic, the azimuthal angle, Ψ, is measured from the -y axis and this location denotes the bottom of the cyclocopter "cage" – that is, the cylindrical volume swept out by one revolution of the blades. During rotation, the blades pitch at an angle θ

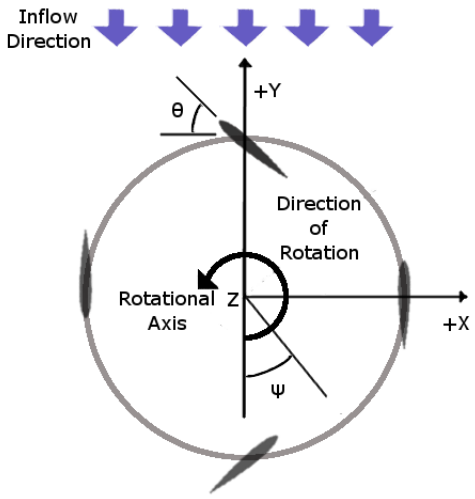

Figure 1.1: Schematic of the hovering cyclocopter.

periodically over one revolution through the use of a passive mechanism causing changes in angle of attack. Through control of the pitch amplitude and phase, the amplitude and direction of thrust for the cycloidal rotor can be specified.

1.2 Previous Work

1.2.1 Experimental Work on Full-Scale Cycloidal Rotors

Though a seemingly novel concept, the cycloidal rotor has been studied since the 1920's although not for MAV-scales, but rather as a means of propulsion for full-scale air vehicles. In 1926, Kirsten [1] at the University of Washington developed in conjunction with the Boeing Company the Kirsten-Boeing Propeller, a six-bladed cycloidal rotor wherein thin, elliptical blades rotated opposite to the direction of thrust of the system, as shown in Figure 1.2(a). The blades also pitched at half the angular velocity of revolution, and therefore would reach 90° at 180° azimuth and 180° at the end of one revolution. Kirsten proposed

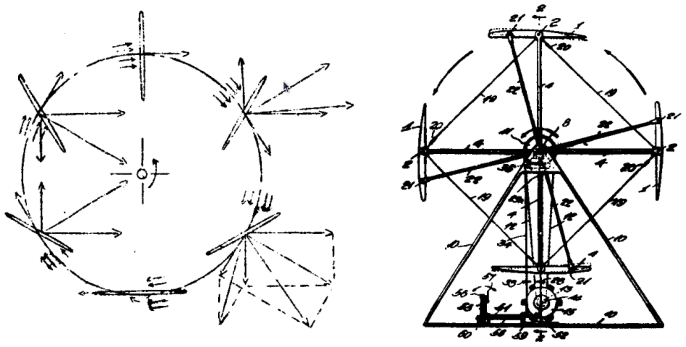

(a) Kirsten, 1926 (Ref. 1) (b) Strandgren, 1933 (Ref. 2)

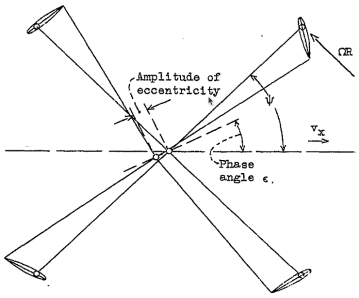

(c) Wheatley, 1933 (Ref. 3)

Figure 1.2: Schematics of early full-scale cycloidal rotor concepts.

this system as a solution to rectify propulsion deficiencies on airships. Though a cycloidal propeller was scheduled to be outfitted on the U.S. Navy airship Shenandoah, the loss of the Shenandoah as well as the subsequent decrease of interest in airships over the following decades prevented such flight tests of the cycloidal rotor from materializing.

Strandgren [2] at NACA in 1933 developed a more complex control system for the "cyclogiro" which allowed change of incidence of the blades about a feather axis parallel to their span such that they could conform to the desired flight mode. Strandgren's schematic is seen in Figure 1.2(b). He further formed a theoretical basis for determining the angle of incidence of each blade with

respect to the freestream, as well as a simple analytical model to evaluate the resultant forces on the blades.

Concurrently, Wheatley [3] at NACA used a double-cam arrangement on a cyclogiro to periodically vary both blade amplitude and phase angle, as shown in Figure 1.2(c). He additionally formed an aerodynamic model for rotor performance based on Momentum Theory with the assumption that the induced velocities were constant in magnitude throughout the rotor center. By varying parameters such as solidity and blade aspect ratio, he was able to refine his design to a more optimized configuration. However, subsequent wind tunnel tests in 1935 by Wheatley and Windler [4] for an 8-foot span and diameter model showed that their simplified theory, while capturing the correct periodic variation of power, severely underpredicted the zero-lift power due to their low profile drag coefficient prediction. Hence, they deduced that the cyclogiro would in forward flight consume an inordinate amount of power, impractical for the powerplants of the day.

The bulk of the work undertaken in this era showed that the cycloidal rotor concept was not very feasible at this scale. The problem, as characterized in the literature, was threefold: a large zero-lift power due to the profile drag from spinning the blades at high incident angles; a large centrifugal force associated with rotor revolution, from which mechanical problems arose in providing anti-torque and damping vibrations; and difficulties characterizing the complex, unsteady flow environment to understand the aerodynamics and predict performance.

1.2.2 Interim work on Cycloidal Wind Turbines

After the loss of interest in cycloidal propellers in the early half of the 20th century, subsequent research into full-scale cycloidal rotors was commenced by the wind turbine community. Cycloidal Wind Turbines (CWT), otherwise known as H-rotors or Giromills, were developed as a new variant of the Vertical Axis Wind Turbine (VAWT) design. Essentially, a CWT consists of a cycloidal rotor mounted to a mast with blades pitching and rotating perpendicular to the ground. A straight-bladed VAWT (often abbreviated H-Darrieus, S-VAWT or SW-VAWT) is essentially a CWT with fixed blade pitch. Since the objective of a wind turbine is to operate in an effective axial descent condition and extract drag power from the freestream wind, large profile drag of the blades is a desirable characteristic, unlike with the cycloidal propeller.

Though VAWTs have existed since antiquity, the first modern design came to fruition in 1931, when Darrieus [5] patented a wind turbine with straight or bent blades and a fixed pitch. A schematic of the two different types of Darrieus turbines is presented in figure 1.3; the left is a conventional Darrieus turbine and the right is a straight-bladed H-Darrieus (note that the CWT resembles the H-Darrieus with a blade pitching mechanism). Sheldahl [6] at Sandia National Laboratories tested various sized Darrieus wind turbines both in wind tunnels and in the field, and tabulated data on their performance. Sheldahl and Klimas [7] also conducted comprehensive tests to determine the steady aerodynamic characteristics of seven different symmetrical airfoil sections from 0° to 180° angle of attack for use in VAWT analysis models. Ferreira et al. [8] systematically performed 2-D PIV visualization of dynamic stall on the suction side of an S-VAWT blade for different Reynolds numbers and tip speed ratios (TSR), defined

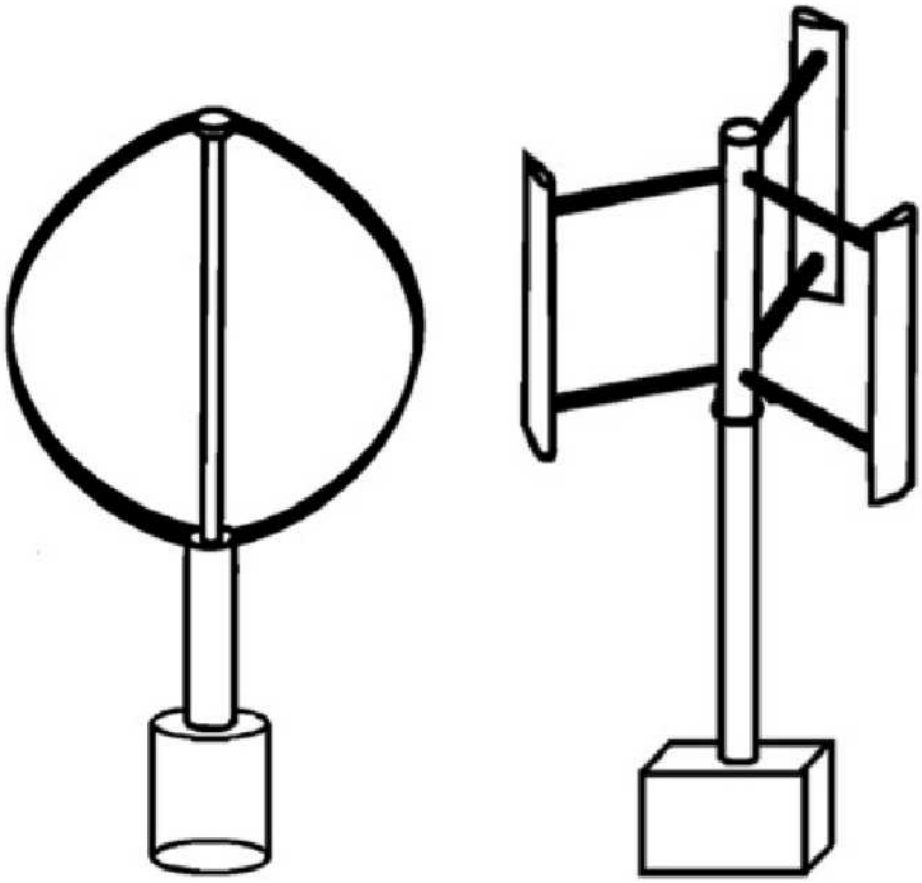

(a) Conventional Darrieus (b) H-Darrieus

Figure 1.3: Schematic of two different vertical axis wind turbine designs.

as the ratio of velocity of the advancing blade to the freestream wind velocity. In addition, significant numerical work has been undertaken to study the VAWT; since modeling of VAWTs is not a focus of this work, a literature review can be found in Appendix A.

Relatively current experimental work on the VAWT and CWT has been undertaken by Takao et al. [9] and Takahashi et al. [10]. Takao tested different

configurations for a directed guide vane row in a wind tunnel to improve performance of an S-VAWT. Takahashi tried various NACA 00-series airfoils and constructed a "wind-lens" structure upstream which collected and accelerated the flow through the S-VAWT to enhance its performance. Both studies found that with regard specifically to the VAWT, at low tip speed ratios the VAWT performed better with increasing TSR due to the blades extracting power at every section of the rotor, but with higher TSR performance degraded quickly because portions of the rotor began consuming, instead of extracting power. With regard to the CWT, Kiwata et al. [11] investigated the effects of using a four-bar linkage mechanism to passively pitch the blades of an S-VAWT, and tabulated the performance changes with variations in pitch amplitude, phase angle, number of blades, and airfoil profiles. He found from his experiments that cambered blades with almost no phasing generated the maximum power.

1.2.3 Experimental Work on MAV-Scale Cycloidal Rotors

Recently, interest has arisen in applying the cycloidal rotor to MAVs. Though mechanics and control problems have largely been unresolved, and a good understanding of the aerodynamics is still lacking, the reduced centrifugal force at these scales may present a large advantage when compared to full-scale. Also, the possibility to instantaneously change the direction of thrust using a cycloidal rotor allows extreme maneuverability, which is useful for MAVs that operate indoors and in closed space environments. Furthermore, the cycloidal concept is very stable in cross-winds and gusts, a problem that plagues many current-day MAVs.

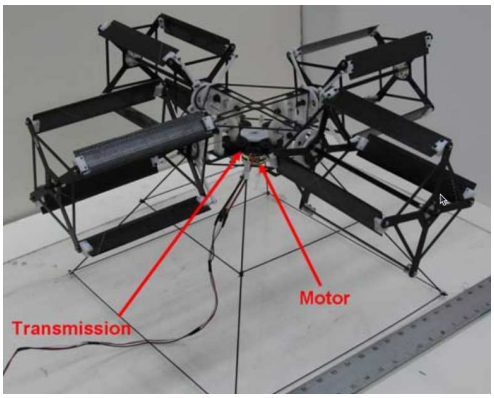

Figure 1.4: The cyclocopter MAV developed by Benedict et al. (Ref. 15)

Previous work on micro-scale aerodynamics of the cycloidal rotor was undertaken by Hwang et al. [12], who designed and subsequently conducted multidisciplinary optimization of a cyclocopter system, resulting in the construction of a successfully-hovering micro-scale four-rotor testbed. They demonstrated that their experimental cyclocopter configuration would produce adequate thrust for both hover, low-speed forward and maneuvering flight conditions.

Yu et al. [13] experimentally tested the parameters of airfoil geometry, taper ratio, and control link length on the hovering cyclocopter. As a metric to evaluate the performance of different cycloidal propeller configurations, they compared power loading vs. disk loading curves to determine which design produced the most thrust per unit power for a given disk area. Yu found that to maximize performance at low Reynolds numbers typical of MAV-scale craft, a flat plate with minimal taper and slightly higher pitch at the bottom rather than the top of the cyclocopter cage is desired. The reasoning behind the last design choice will be discussed in detail later.

A considerable amount of experimental work has been done at the University of Maryland regarding MAV-scale cycloidal rotors. Benedict et al. [14, 15] as-

sembled an experimental model by which he could measure the performance and examine the flowfield of the cycloidal rotor systematically for various numbers of blades and rotational speeds. The MAV-scale cyclocopter developed from this work is shown in Figure 1.4. The weight of the vehicle is $\sim 800g$ and the length is $\sim 24in.$, though the characteristic lengths of blade span and rotor diameter are both $\sim\ 6in.$, thus satisfying the definition of an MAV. Recently, Benedict et al. [16] investigated the effects of pitching axis location, asymmetric blade pitch amplitude, airfoil profile, number of blades, and blade flexibility on his cyclocopter design; by finding the optimized values of these parameters, he achieved a large increase in overall efficiency. Overall, these experimental studies have shown the viability of the cycloidal rotor as a competitive design to conventional rotors for use on MAVs.

1.2.4 Analytical Models of MAV-Scale Cycloidal Rotors

In addition to experiment, simple analytical studies have been conducted in literature to predict performance as well as improve design of the cycloidal rotor. Yun et al. [17] used blade element momentum theory to form a simple algebraic model for estimation of thrust and inflow produced at the top and bottom half of the rotor.

McNabb [18] used the equations of Garrick [19] regarding the unsteady lift and moments of a 2-D airfoil moving in sinusoidal motion and derived equations for simplified unsteady aerodynamics of a cycloidal rotor with realistic four-bar blade pitching motion, both in hover and forward flight. He also modeled the downwash as a constant velocity flow through the rotor because the effect of induced angle of attack on the bottom blade could not be neglected, but relegated

interactions between the blades to first-order analysis. From this, he found that his model could predict to within 10% accuracy the power and total force obtained from the Wheatley wind tunnel tests. In addition, McNabb deduced that the aerodynamic loads were insignificant compared to the inertial loads; and, though susceptible to wind gusts, the resultant force on the cyclocopter was quickly damped out.

Parsons [20] used double-multiple streamtube theory to analyze flow through the cycloidal rotor. In this analysis, "multiple" denotes that the flow through the rotor is subdivided into a number of streamtubes; these streamtubes are aerodynamically independent of each other and have different induced velocities at the upstream and downstream halves of the volume swept by the rotor. For each streamtube, "double" indicates that the rotor is modeled as two thin actuator disks such that the effects of the upstream wake on the downstream blades are captured. The flow through the rotor was assumed to be one-dimensional, incompressible and inviscid. Solving for the conservation equations, Parsons was able to obtain a relatively accurate first-order model to estimate the aerodynamic forces and power of his cycloidal rotor setup.

More recently, Benedict et al. [21] developed an analytical model to predict the performance of their MAV-scale rotor at different symmetric and asymmetric pitching angles, pitch link locations, and rotational speeds. From their results, they found that the thrust prediction correlated well with experiment, but there were discrepancies in power prediction. Though Benedict's and other lower order models described above can predict the performance fairly reasonably, they do not provide much insight into the underlying flow physics.

1.2.5 CFD Studies of MAV-Scale Cycloidal Rotors

CFD can provide a better understanding of the flow physics in the complex cycloidal rotor environment. However, CFD needs to carefully validated against experiments to ensure accuracy of the results. Previously, Hwang et al. conducted both a 2-D and 3-D analysis using STAR-CD (a commercially available CFD solver) with a k-ε turbulence model on a micro scale four-bladed cycloidal rotor. The analysis was run on an unstructured mesh generated with the Patran Command Language, with blade pitching simulated using the moving mesh method. From this, they determined the optimal conditions by which their cyclocopter design operated and calculated a power requirement within 15% of the experimental value. However, though their 3-D analysis predicted performance correctly, it utilized relatively coarse meshes and therefore, could not provide much insight into the flowfield. In addition, the use of the high-Reynolds k-ε turbulence model for such a low-Reynolds application may not have been appropriate.

Iosilevskii and Levy [22] studied both two- and four-bladed cyclocopters using the 2-D EZNSS flow solver assuming laminar compressible flow, with time integration conducted using the implicit Beam-Warming algorithm. Their code was run at low Reynolds and Mach numbers with a micro-scale characteristic chord length, comparable aspect ratio and rotor radius-to-chord ratio to Benedict's work, and pitch angles of 15° - 25°. The blades were simulated with body-fitted C-shaped meshes, then overset with a Chimera scheme on a Cartesian background mesh. From this analysis, they demonstrated that the effectiveness of a cycloidal rotor may be comparable with that of a heavy-loaded helicopter rotor. However, their 2-D simulation assumed infinite span and therefore, did not

capture the complete 3-D flow physics. Furthermore, their use of a relatively coarse Cartesian background mesh also lacked the grid refinement to accurately visualize the flow.

1.3 Objective of Current Work

The current work focuses on developing and validating a CFD based methodology that can help understand the aerodynamics of the cyclocopter and details of the flow physics which was missing in previous works. This entails modifying an existing Reynolds Averaged Navier-Stokes (RANS) compressible solver, previously employed by Lakshminarayan and Baeder [23] in the aerodynamic investigation of micro-scale hovering coaxial rotors, to be applicable to cycloidal rotor geometries. The primary objective is to characterize unsteady performance and provide insight into the flow physics. The secondary objective is to refine the solver to obtain force and power values comparable to MAV-scale cycloidal rotor experiments, thus becoming an accurate predictive tool for performance. A tertiary objective is to apply the understanding of the flow physics obtained from this work to improve rotor design. Due to the difficulty of simulating such a dynamic flow environment, numerical simulation of cycloidal rotors has not been previously studied to a great extent. It is hoped that through this work, the improved predictive capability of the current CFD solver will provide a powerful tool to understand flow physics and benefit future optimization efforts for this rotor configuration.

1.4 Thesis Outline

This thesis is organized into six chapters. Chapter one provides the definition of the problem, previous experimental and numerical work, and the objective of the current research. Chapter two describes details on grid generation, prescribed grid motions and deformations, and specific numerical methods used in the flow solver. Preliminary tests on steady symmetric airfoils and unsteady pitching airfoils that were performed to validate the solver are presented in chapter three, thus allowing confidence to be gained in the accuracy of the flow solution. In Chapter four, the experimental setup of Benedict et al. used for validation of the flow solver on cycloidal rotor geometries is described. Also, it describes cyclocopter-specific overset grid generation, deformations, and blade motion incorporated into the flow solver to provide a high fidelity simulation of the experiment. In addition, Chapter four compares performance of both the 2-D and 3-D CFD solvers to the experiment, and exhibits the strengths as well as shortcomings of both solvers in predicting the thrust and aerodynamic power of the cycloidal rotor at various operational conditions. Chapter five provides insight into the flowfield as predicted by the 3-D flow solver. In particular, it explores the unsteady performance and three-dimensionality of the flowfield in ways difficult to achieve with experimentation. Finally, a summary of results from the present study as well as future work for improving the quality of the CFD predictions for the cyclocopter is proposed in chapter six.

1.5 Key Contributions of the Current Work

As will be presented in the following chapters, the current work provides several key contributions to simulating and understanding of the cyclocopter and its flow physics. Firstly, the simulation incorporated a high-resolution overset mesh system with a realistic "four-bar" grid motion and blade deformations to achieve a highly-detailed model of the experiment. This grid was specifically targeted to resolve the flow physics; this was unprecedented in previous works, which only focused on design. Secondly, it validated the current flow solver with experiments at low-Reynolds flows of interest with large unsteady blade motions at high angles of attack. This reinforced the confidence in the solver to predict accurate results in highly unsteady and separated flows. Thirdly, it compared the flow solver with cyclocopter experiments and noted its predictive capability for both force and power. It also sought to explain the cause for discrepancies between CFD and experiment, and suggested future improvements to the simulation for improvement of accuracy. Finally, this work provided unprecedented insight in understanding the three-dimensionality of the cyclocopter flowfield as well as provided highly detailed flow visualization. It associated specific observed flow phenomena with the trends seen in performance, thus allowing greater advancement in the understanding of the cycloidal rotor aerodynamics.

Chapter 2

Methodology

Computational Fluid Dynamics (CFD) is a powerful tool to provide flow visualization and performance predictions of low-Reynolds number flight regimes. It can allow for insight into the flowfield in ways unattainable or impractical with experiment, as well as provide an inexpensive way for testing new blade designs and rotor configurations to arrive at an optimized design. However, all CFD solvers must be first validated with a baseline experiment to ensure physical results are being produced.

For all CFD approaches, a mesh must first be generated that resolves the geometry, as well as provides sufficient resolution to capture flow features without smearing. Secondly, the governing equations must be chosen such that they are adequate for the flow regime of interest, especially taking into consideration the Reynolds and Mach numbers at which the vehicle operates. Boundary conditions must also be imposed on the geometric surfaces as well as the farfield. Finally, the numerical solver methodologies must be chosen such they they can iteratively solve the governing equations to arrive at a solution which closely matches experiment. This chapter will describe such numerical methodologies with specific focus on those used in the Overset Transonic Unsteady Rotor Navier-Stokes

(OVERTURNS) code [24], the flow solver employed in this work.

2.1 Grid Generation Methods

A well-generated mesh which has sufficient resolution to capture essential flow structures such as tip vortices, while not being too computationally expensive to solve, is crucial for a reliable CFD model. The cycloidal rotor simulation utilized body-fitted C-O blade meshes which were overset onto cylindrical background meshes. On the blade mesh, the airfoil surface is modeled as a viscous, adiabatic wall. The mesh extending from this blade surface contains points in the tangential, or "wrap-around" direction, ξ; the spanwise direction, η; and the normal direction to the blade, ζ. On the cylindrical mesh, (ξ, η, ζ) are defined as the tangential, radial, and spanwise directions respectively. The directions of these coordinates are shown in physical space (i.e. relative to (x, y, z)) for

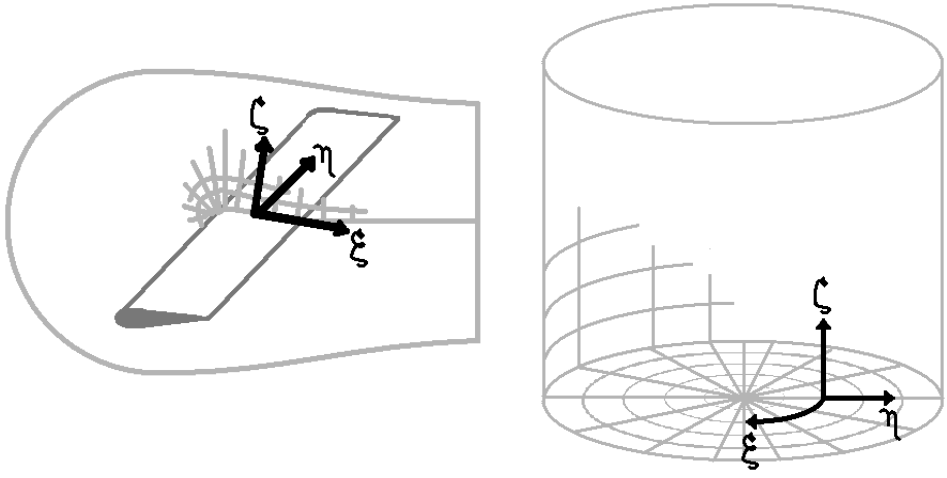

(a) Coordinate system on blade mesh (b) Coordinate system on cylindrical mesh

Figure 2.1: Computational coordinate systems for both blade and background mesh in physical space

both meshes in Figure 2.1. A simple grid transformation from physical space to computational space is used to account for geometric changes and stretching factors used in physical space; one can think of this as "unwrapping" the grid from the airfoil or the background mesh and mapping it onto a Cartesian coordinate system. This process is computationally inexpensive and maintains accuracy; the resultant Cartesian computational grid allows the governing equations to be solved.

For the cyclocopter grids, an algebraic grid generation scheme was employed for the background meshes and a hyperbolic grid generator was used to produce the blade meshes. The following subsections will provide a brief overview of each grid generation methodology.

2.1.1 Algebraic Grid Generation

The cylindrical mesh was generated using algebraic grid generation; an example is shown in Figure 2.2. Points in the tangential direction are distributed evenly. In the radial direction, even spacing is maintained within 4-5 chords away from the cyclocopter "cage"; in the spanwise direction, even spacing extends along the blade length to one chord past the tip of either end. For the remaining sections progressing away from the rotor cage in the radial and spanwise directions towards the outer boundary, the simple one-parameter hyperbolic tangent stretching function of Vinokur [25] is used, as discussed below.

Vinokur developed a general two-sided stretching function which allows arbitrary stretching or clustering to be specified independently at each end of the meshed region. This permits radial distribution of the cylindrical mesh to be defined piecewise, where continuity of grid spacing is maintained at the ends of

each adjacent piecewise segment.

Consider the desire to distribute ξ_{max} points along a distance s_{max} in physical space, where the initial spacing is Δs_0 and the final spacing is Δs_1. ξ, in this case, is an arbitrary direction in computational space, with ξ_{max} being the maximum incrementation of computational points in that direction. Vinokur's procedure ensures that the following prescribed initial conditions are satisfied:

$$\begin{aligned} s\left(0\right) &= 0 & \frac{ds}{d\xi}\left(0\right) &= \Delta s_0 \\ s\left(\xi_{max}\right) &= s_{max} & \frac{ds}{d\xi}\left(\xi_{max}\right) &= \Delta s_1 \end{aligned} \tag{2.1}$$

The equation for distributing the points in the s direction is shown below:

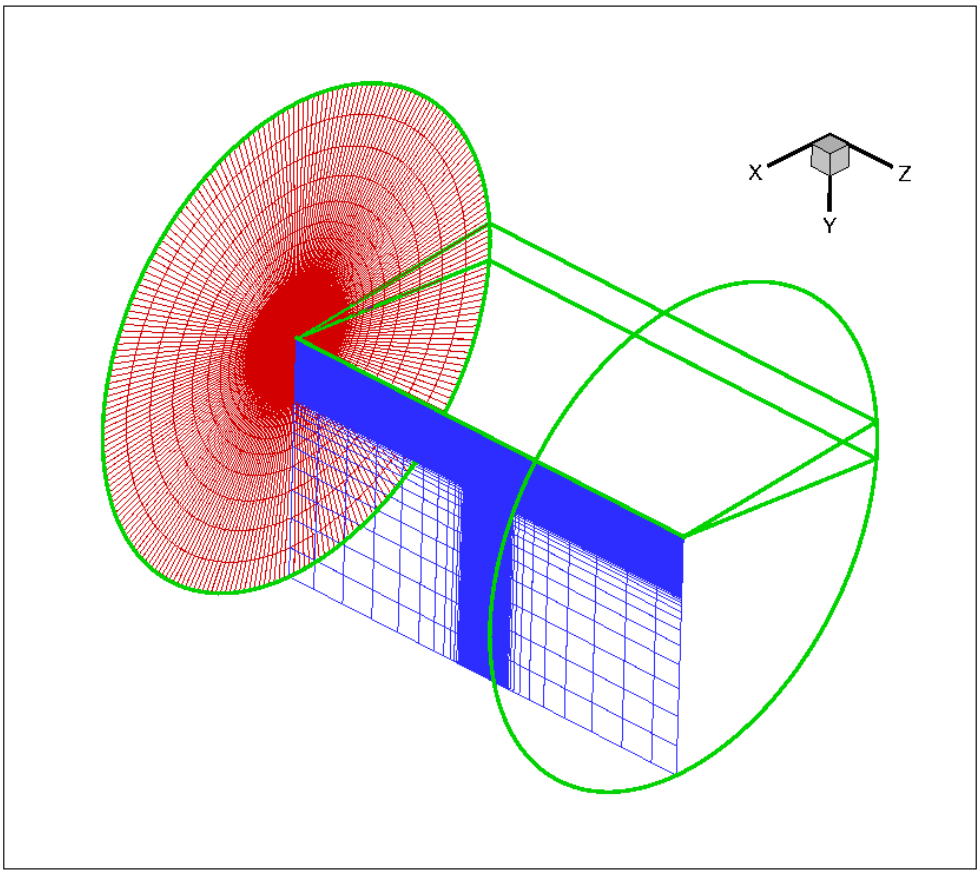

Figure 2.2: An example cylindrical background mesh.

$$s(\xi) = \frac{u_V(\xi)}{A_V + (1 - A_V)\, u_V(\xi)} \tag{2.2}$$

where

$$A_V = \frac{\sqrt{\Delta s_0}}{\sqrt{\Delta s_1}} \tag{2.3}$$

$$u_V(\xi) = \frac{1}{2} + \frac{\tan\left[\Delta z\,(\xi - 1/2)\right]}{2\tan\left(\Delta z/2\right)} \tag{2.4}$$

$$\frac{\sin \Delta z}{\Delta z} = \frac{1}{\xi_{max}\sqrt{\Delta s_0 \Delta s_1}} \tag{2.5}$$

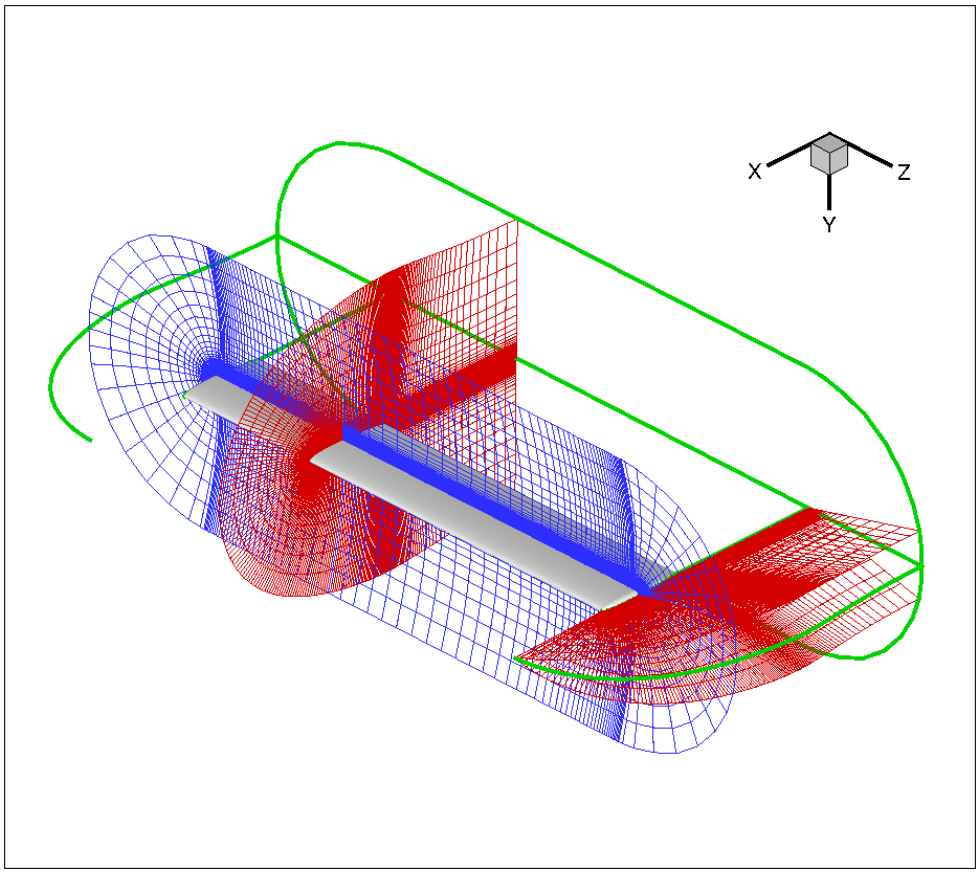

Figure 2.3: An example C-O blade mesh.

In the above equations, A_V is a constant based on a given Δs_0 and Δs_1. Δz is the recursive solution of the transcendental equation Eq. 2.5 and thus is a function of the desired end grid spacings as well as the total number of points to be distributed. When the above series of equations are solved, $s(\xi)$ will describe the distribution of points along a line in physical space as a function of the incrementation in an arbitrary direction of computational space, ξ.

2.1.2 Hyperbolic Grid Generation

Hyperbolic mesh generation was used to create the blade mesh. This type of mesh generation allows a high-quality mesh that maintains orthogonality to be generated from an initial specification of cell size, distance, and surface data. It ensures that the cells close to the surface do not suffer from distortion, as well as allows the transformation of partial differential equations to produce the smallest number of additional terms while retaining the greatest accuracy for numerical differencing techniques [26]. Using these methods, good resolution at the airfoil surface and areas of interest, as well as good cell sizing, are maintained. Further, "local" problems can be avoided such as propagation of initial discontinuities and the formation of grid shocks, thus easing the implementation of turbulence models [27] and increasing computational efficiency.

In the application of a hyperbolic scheme, the mesh is propagated in the normal direction (essentially time-like) from an initial boundary curve (essentially space-like), where each new state is generated from the known conditions at the current state. For the cycloidal rotor blades, these planes are continually extruded from the blade surface until a predefined boundary limit. An example C-O blade mesh is shown in Figure 2.3. More detail on two-dimensional hyperbolic

grid generation can be found in works by Alsalihi [28], Cordova and Barth [29], and Kinsey and Barth [30] ; a generalized method for three-dimensional hyperbolic generation is described by Chan and Steger [31].

For an isolated blade mesh, the hyperbolic generation is allowed to extrude out to at least 20 chords away from the blade surface. However, for a blade overset onto a background mesh, the blade mesh region only extends to at most 2 chords away from the blade surface to avoid overlap in multi-bladed cases.

2.2 Overset Grid Methodology

As discussed in the previous sections, finely-spaced blade meshes are overset onto a coarser background mesh to allow for blade motion and maintain computational efficiency while capturing all of the flow features. An example overset blade/background mesh system for a hypothetical 2-bladed cycloidal rotor with 40° initial blade pitch is shown in Figure 2.4. In this system, information is

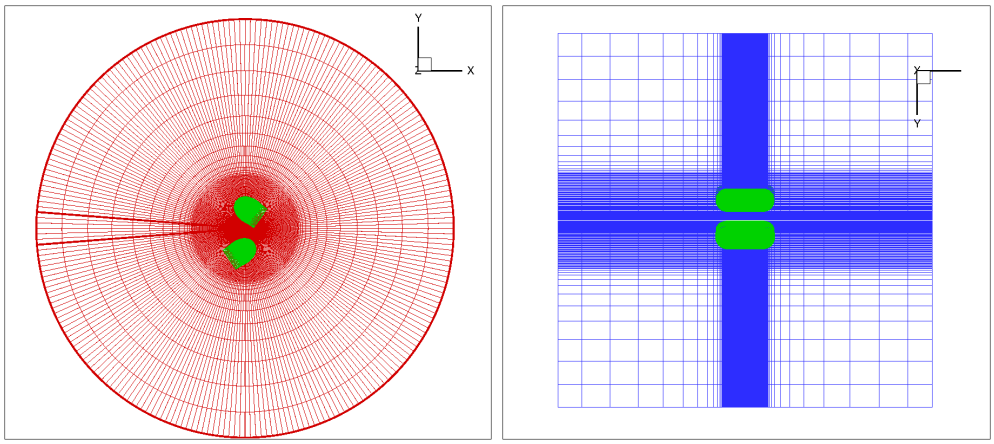

(a) Chordwise view (b) Spanwise view

Figure 2.4: Example overset blade / background mesh system for a 2-bladed cycloidal rotor with 40° initial pitch.

transferred between these two meshes through domain connectivity. In this process, a "donor" cell on one mesh will give information to a "receiver" cell on the other mesh. Significant effort is made to ensure that the donor and receiver cells are roughly equivalent in size, such that information can be interpolated between meshes without loss of too much accuracy. In addition, a "hole" is cut in the background mesh where the blade mesh is located to maintain consistency of solution in the entire computational domain.

In this work, the Implicit Hole-Cutting (IHC) routine developed by Lee and Baeder [32] and refined by Lakshminarayan [24] was used to determine the connectivity information between the blade and background meshes. Lee and Baeder refined the baseline Chimera hole-cutting technique in OVERTURNS, which was capable of handling only two overset meshes. The original overset routine involved specifying a box around the blade and extracting a list of hole fringe points that require information from other grids to serve as boundary conditions. To avoid the effect of invalid hole points on the solution, an array of integers (the *iblank* array) is defined, one for each grid point, with the value 0 for hole and fringe points, and 1 for field points. However, defining such an arbitrary box around the body with the *iblank* array forces the hole to be cut in the same location regardless of differences in grid resolution between the blade and background meshes. Therefore, a large difference in grid resolution could result in hole fringe points interpolating from donors that have extremely different cell volumes from receivers, resulting in a high level of inaccuracies with the interpolation.

Lee and Baeder's approach used an intermediate background mesh to improve transfer of information from the blade mesh to the background mesh, and could

be operated without prior knowledge of where the hole fringe points are. At every point in the grid, the IHC method computes the solution on the cells having the smallest volume, then selects these "best quality" cells in multiple overlapped regions to interpolate to other points, leaving the rest as hole points.

Lakshminarayan improved on the work of Lee and Baeder by implementing an *iblank* array to the IHC routine. The original IHC routine required thick hole fringe layers to completely enclose the body to prevent invalid points, but this required a large number of interpolations, and furthermore sufficiently thick fringe layers were not always guaranteed. The Lakshminarayan approach allowed blanking of the hole fringe points during implicit inversion, thus permitting the use of valid solutions from the blanked out points in the flux calculations by setting *iblank* to -1. Hence, Lakshminarayan's method makes Lee's hole-cutting process less computationally intensive while still maintaining accuracy.

2.3 Grid Motion

An accurate simulation of the cycloidal rotor as consistent with experiment requires that the blade rotation and pitching about the rotor cage be prescribed as a blade grid motion on the background mesh. In addition, the structural deformations due to centrifugal forces from spinning at a high RPM must be prescribed onto the blade mesh as well. The following subsections explore the numerical procedures for incorporating such grid motions into the flow solver.

2.3.1 Grid Rotation

For each physical timestep taken in the flow solver, the blade meshes are rotated azimuthally about the rotor center. The non-dimensional timestep size, Δt, as determined in Table 2.1, is equivalent to the incremental degree of azimuth that the blade meshes are rotated. For example, if non-dimensional Δt was set to 0.25, the blade meshes would move a quarter-degree per iteration. Hence, with this example timestep size, 1440 iterations would correspond to one revolution about the rotor cage.

2.3.2 Numerical Approximation of the Four-Bar Pitching Mechanism

To provide a high-fidelity model of the blade pitch for the flow solver, a numerical approximation was used to prescribe this motion to the blade meshes. The experimental cyclocopter employed a pitching mechanism developed by Parsons and refined by Benedict to passively pitch the blades. This mechanism consists of two pitch bearings, arranged such that they cause an offset between the axis of the rotor shaft and an offset ring; Benedict denotes this distance as L_2. This configuration essentially comprises a crank-rocker type four-bar pitching mechanism, with the offset distance L_2 determining the pitch amplitude. Although this configuration ideally approximates a sinusoidal motion, mechanical limitations result in a pitching motion with about 10° phase offset from a truly sinusoidal curve. Figure 2.5 shows the variation in pitch angle over one rotor revolution with the four-bar mechanism as a function of azimuthal angle, as compared with a pure sinusoidal pitch angle variation, for 35° pitch amplitude. As seen from the figure, the blades achieve a maximum pitch angle in the the

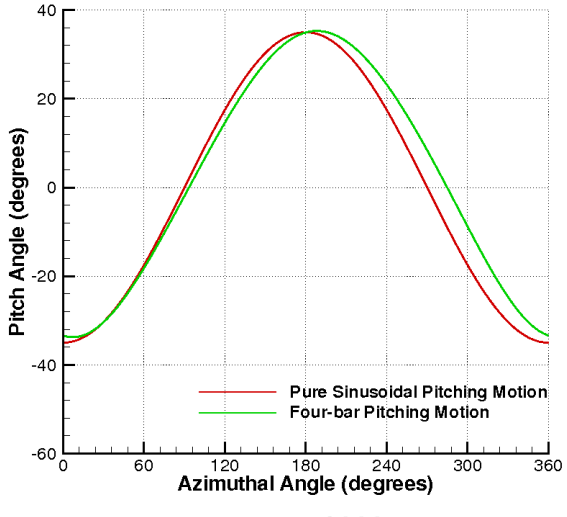

Figure 2.5: Pitch variation with respect to azimuthal angle for the four-bar linkage mechanism.

positive y-direction (with respect to the axis in Figure 1.1) when slightly past the $\Psi = 0°$ and $\Psi = 180°$ azimuthal positions i.e. the "bottom" and "top" of the rotor cage. The "collective pitch amplitude" described hereafter refers to the maximum pitch angle which the blade attains at these two azimuthal locations. At a slight offset past $\Psi = 90°$ and $\Psi = 270°$, which correspond to the "sides" of the cyclocopter cage, the pitch angle goes to zero.

In the flow solver, blade pitch is calculated using numerical approximation to the aforementioned four-bar linkage mechanism, shown below.

$$\theta = \pi/2 + 2\tan^{-1}\Psi_1 \tag{2.6}$$

where

$$\Psi_1 = \frac{\sin\Psi - \sqrt{\sin^2\Psi + (\cos\Psi + L_1/L_2)^2 + f^2}}{\cos\Psi + L_1/L_2 + f} \tag{2.7}$$

$$f = \frac{L_1}{L_4}\cos\Psi + \frac{L_1^2 + L_2^2 + L_4^2 - L_3^2}{2L_2L_4} \tag{2.8}$$

In the above equations, L_1, L_2, L_3, and L_4 represent the non-dimensional lengths of pitch linkages with respect to the blade chord, and determine the pitching motion. θ denotes pitch amplitude and Ψ is azimuthal angle of the blade around the rotor cage. Details regarding the application of this equation to the cyclocopter are provided in Section 4.3.

2.3.3 Blade Deformations

From a structural dynamic perspective, a blade dynamic response distribution can be prescribed onto the numerical grids to ensure accuracy and consistency with experiment. The methodology provided by Sitaraman [33] was modified such that it was applicable to the cycloidal rotor geometry.

A structural dynamic analysis developed by Benedict et al. [21] was used to output blade deformations. Benedict developed an FEM-based aeroelastic analysis by modeling the cycloidal rotor blades as second-order non-linear, isotropic Euler-Bernoulli beams with six spanwise elements undergoing radial bending, tangential bending, and elastic twist (torsion, ϕ) deformations, as shown in Figure 2.6. This was based on the coupled flap-lag-torsion equations of Hodges and Dowell [34]. The blades were assumed to have pin-pin boundary conditions on both ends for bending and fixed-free boundary conditions for torsion due to the rigid pitch link on the root end. In addition, Hamilton's principle was used to develop the equations of motion for the blade. The finite element in time method was used with 60 timewise elements to obtain the steady blade periodic response.

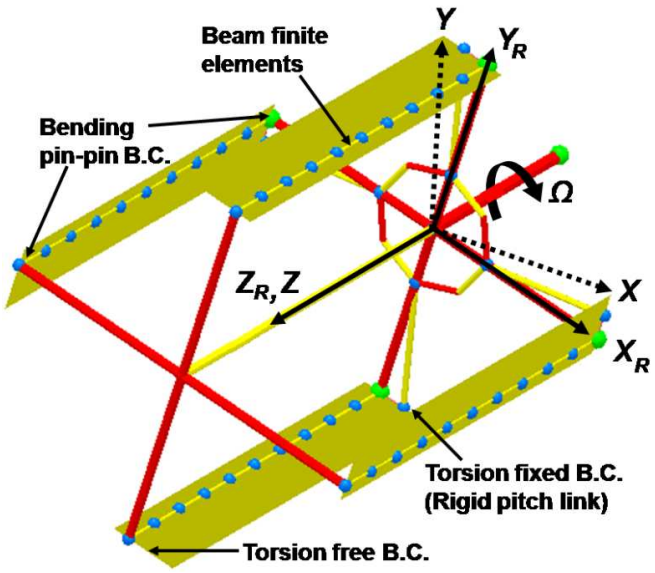

Figure 2.6: Schematic of the FEM model used by Benedict et al. (Ref. 21)

The above computational structural dynamics analysis provides deformations in the form $[\underline{u}, \underline{v}, \underline{w}, \underline{u}', \underline{v}', \phi]^T$, where $\underline{u}, \underline{v}, \underline{w}$ are linear deflections in the radial, tangential, and spanwise directions; $\underline{u}', \underline{v}'$ are the derivatives for the u and v motions, and ϕ is the elastic torsional deformation. After the deformation data is read in, it is interpolated radially using cubic splines and azimuthally using Fourier transforms. The rotation matrix found from these parameters are as follows:

$$T_{DU} = \begin{bmatrix} \left(1 - \frac{\underline{u}'^2}{2}\right)\cos\phi - \underline{u}'\underline{v}'\sin\phi & \left(1 - \frac{\underline{u}'^2}{2}\right)\sin\phi - \underline{u}'\underline{v}'\cos\phi & \underline{u}' \\ \left(1 - \frac{\underline{v}'^2}{2}\right)\sin\phi & \left(1 - \frac{\underline{v}'^2}{2}\right)\cos\phi & \underline{v}' \\ -(\underline{u}'\cos\phi + \underline{v}'\sin\phi) & \underline{u}'\sin\phi + \underline{v}'\cos\phi & 1 - \frac{\underline{u}'^2 - \underline{v}'^2}{2} \end{bmatrix} \tag{2.9}$$

Finally, the deformed mesh coordinates in the blade fixed frame are given by the equation:

$$\begin{bmatrix} x' \\ y' \\ z' \end{bmatrix} = \left(T'_{DU}\right)^T \begin{bmatrix} x \\ y \\ z \end{bmatrix} + \begin{bmatrix} \underline{\mathrm{u}} \\ \underline{\mathrm{v}} \\ \underline{\mathrm{w}} \end{bmatrix} \tag{2.10}$$

2.4 Flow Solver

With the grid generated and the grid motions prescribed, the initial setup for the flow solver is completed. The flowfield properties at each grid point within the overset mesh system can now be obtained by solving the conservation laws of physics for fluid flow. The following subsections describe these governing equations, as well as certain numerical methods to ensure their convergence for low-Mach and Reynolds number flight regimes. This section will conclude with a description of the specific numerical methods used in the OVERTURNS CFD code It should be noted that TURNS refers to the baseline flow solver, whereas OVERTURNS is the overset version of the solver. However, these terms are used interchangeably in this work.

2.4.1 Compressible Navier-Stokes Equations

The Navier-Stokes equations comprise the mass, momentum, and energy conservation governing equations used in the flow solver. These equations solve for compressibility as well as viscous effects, which are particularly important for the low-Reynolds numbers flows pertaining to the cyclocopter MAV. The 3-D compressible Navier-Stokes equations in physical space (i.e. (x, y, z) coordinates) are given by:

$$\frac{\partial Q}{\partial t} + \frac{\partial E}{\partial x} + \frac{\partial F}{\partial y} + \frac{\partial G}{\partial z} = S \tag{2.11}$$

In the above equation, the state vector in conservative form is given by:

$$Q = \begin{Bmatrix} \rho \\ \rho u \\ \rho v \\ \rho w \\ e \end{Bmatrix} \tag{2.12}$$

The flux vectors, E, F, and G, with both inviscid and viscous terms, are given by:

$$E = \begin{Bmatrix} \rho u \\ \rho u^2 + p - \tau_{xx} \\ \rho uv - \tau_{xy} \\ \rho uw - \tau_{xz} \\ uH - u\tau_{xx} - v\tau_{xy} - w\tau_{xz} + k_c \frac{dT}{dx} \end{Bmatrix} \tag{2.13}$$

$$F = \begin{Bmatrix} \rho v \\ \rho uv - \tau_{yx} \\ \rho v^2 + p - \tau_{yy} \\ \rho vw - \tau_{yz} \\ vH - u\tau_{yx} - v\tau_{yy} - w\tau_{yz} + k_c \frac{dT}{dy} \end{Bmatrix} \tag{2.14}$$

$$G = \begin{Bmatrix} \rho w \\ \rho uw - \tau_{zx} \\ \rho vw - \tau_{zy} \\ \rho w^2 + p - \tau_{zz} \\ wH - u\tau_{zx} - v\tau_{zy} - w\tau_{zz} + k_c \frac{dT}{dz} \end{Bmatrix} \tag{2.15}$$

S is the source term vector, expanded as:

$$S = \begin{Bmatrix} 0 \\ f_x \\ f_y \\ f_z \\ uf_x + vf_y + wf_z \end{Bmatrix} \tag{2.16}$$

The definitions for all the variables used in the above equations can be found in the Nomenclature section. The mean stresses are defined as:

$$\tau_{ij} = \mu \left[\left(\frac{\partial u_i}{\partial x_j} + \frac{\partial u_j}{\partial x_i} \right) - \frac{2}{3} \frac{\partial u_k}{\partial x_k} \delta_{ij} \right] \tag{2.17}$$

where μ is the laminar viscosity, evaluated using Sutherland's law [35].

For the flow solver, as discussed in the previous section, the Navier-Stokes equations must be solved in computational space, such that the flux contributions can be defined with respect to the adjacent computational cell faces. Since the equations above are given in physical space (i.e. (x, y, z) coordinates), a curvilinear coordinate transformation must be employed which converts the Navier-Stokes equations to a uniformly spaced Cartesian coordinate system in computational space (i.e. (ξ, η, ζ) coordinates). Now, the transformed equations are given by:

$$\frac{\partial \hat{Q}}{\partial t} + \frac{\partial \hat{E}}{\partial \xi} + \frac{\partial \hat{F}}{\partial \eta} + \frac{\partial \hat{G}}{\partial \zeta} = \hat{S} \tag{2.18}$$

where

$$\hat{Q} = \frac{1}{J} Q \tag{2.19}$$

$$\hat{E} = \frac{1}{J}\left(\frac{\partial \xi}{\partial x} E + \frac{\partial \xi}{\partial y} F + \frac{\partial \xi}{\partial z} G\right) \tag{2.20}$$

$$\hat{F} = \frac{1}{J}\left(\frac{\partial \eta}{\partial x} E + \frac{\partial \eta}{\partial y} F + \frac{\partial \eta}{\partial z} G\right) \tag{2.21}$$

$$\hat{G} = \frac{1}{J}\left(\frac{\partial \zeta}{\partial x} E + \frac{\partial \zeta}{\partial y} F + \frac{\partial \zeta}{\partial z} G\right) \tag{2.22}$$

$$\hat{S} = \frac{1}{J} S \tag{2.23}$$

and J represents the Jacobian of the coordinate transformation, defined as:

$$J = det\left(\frac{\partial(\xi, \eta, \zeta)}{\partial(x, y, z)}\right) \tag{2.24}$$

It should be noted that in OVERTURNS, all the variables in the Navier-Stokes equations have been non-dimensionalized; generally, length scales were non-dimensionalized by blade chord and dependent variables are non-dimensionalized by freestream conditions. Table 2.1 compares dimensional and non-dimensional values. In this table, a_∞ represents the freestream speed of sound, t the time, and c the chord of the airfoil. Effectively, time is non-dimensionalized to correspond to degrees of azimuthal angle in the rotation of the cyclocopter cage. k_{rot} is the cyclocopter-specific rotational frequency, defined as $k_{rot} = \frac{M_{rot} c}{R}$, where M_{rot} is

the Mach number corresponding to the rotational speed, and R is the radius of the cyclocopter cage. Other non-dimensional definitions which are essential for the flow solver are displayed below.

$$\text{Freestream total velocity:} \quad V_\infty = \sqrt{u_\infty^2 + v_\infty^2 + w_\infty^2} \tag{2.25}$$

$$\text{Reynolds Number:} \quad Re = \frac{\rho_\infty V_\infty c}{\mu_\infty} \tag{2.26}$$

$$\text{Mach Number:} \quad M_\infty = \frac{V_\infty}{a_\infty} \tag{2.27}$$

2.4.2 Reynolds-Averaged Navier-Stokes Equations

The solution of the Navier-Stokes equation, in the form given in Eq. 2.18, has no fundamental difficulties with inviscid or laminar flows. However, since the cyclocopter presents a turbulent flight regime, and a direct simulation of turbulence by solving these time-dependent equations (referred to as Direct Numerical Sim-

Dimensional Variable	Non-dimensional Variable
p, e	$p/\left(\rho_\infty {a_\infty}^2\right)$, $e/\left(\rho_\infty {a_\infty}^2\right)$
t	$\frac{t}{k_{rot}} \frac{\pi}{180^\circ}$
T	T/T_∞
μ	μ/μ_∞
ρ	ρ/ρ_∞
(x, y, z)	$(x/c, y/c, z/c)$
(u, v, w)	$(u/a_\infty, v/a_\infty, w/a_\infty)$

Table 2.1: Non-dimensionalizations in OVERTURNS

ulation, DNS) is very computationally intensive, an approximation to turbulence is needed.

For engineering and physics problems, the Reynolds-Averaged Navier-Stokes (RANS) equations represent an approximation that considerably reduces the amount of calculations needed to solve the governing equations. The RANS equations decompose the flow into mean and fluctuating parts, i.e. any flow variable can be written in the form:

$$\phi = \bar{\phi} + \phi' \tag{2.28}$$

$\bar{\phi}$ represents the mean part, which is obtained from Reynolds averaging in the equation:

$$\bar{\phi} = \frac{1}{\chi} \lim_{\Delta t \to \infty} \frac{1}{\Delta t} \int_0^{\Delta t} \chi\phi\left(t\right) dt \tag{2.29}$$

where $\chi = 1$ if $\phi = \rho$ or $\phi = p$, and $\chi = \rho$ for other variables. ϕ' is the fluctuating part of the equation, and its Reynolds average is zero. These decomposed parts, when placed in the Navier-Stokes equations (Eq. 2.18), result in the mathematical description of the mean flow properties. If we drop the bar on the mean flow variables, the resulting equations are the same as the instantaneous Navier-Stokes equations except for additional terms in the momentum and energy equations; these additional terms are denoted as the Reynolds Stress Tensor, and account for the additional stress due to turbulence. However, these additional Reynolds-stress terms are now unknown, and must be approximated using a turbulence model to achieve closure of the RANS equations.

2.4.3 Turbulence Model

The turbulent controibution to viscosity is approximated by the Reynolds Stress Term, shown below:

$$\tau_{ij}^{R} = -\rho\overline{u_i' u_j'} \tag{2.30}$$

Eq. 2.17 showed the Reynolds stresses with the assumption of isotropic eddy viscosity. Although many turbulence models have been developed to obtain turbulent viscosity, this thesis will focus solely on the two models that were used extensively in this work: the Baldwin-Lomax model [36], and the Spalart-Allmaras model [37].

The Baldwin-Lomax (BL) model is a two-layer algebraic 0-equation model which uses boundary layer velocity profile to determine eddy viscosity. At its core, the model uses the equation:

$$\nu_t = \begin{cases} \nu_{t_{inner}}, & \text{if } y \leq y_{crossover} \\ \nu_{t_{outer}}, & \text{if } y > y_{crossover} \end{cases} \tag{2.31}$$

where $y_{crossover}$ is the minimum distance from the surface where $\nu_{t_{inner}} = \nu_{t_{outer}}$. These are respectively given by:

$$\nu_{t_{inner}} = \rho\left[ky\left(1 - e^{\frac{-y^+}{A^+}}\right)\right]^2 \left[\left|\sqrt{\frac{1}{2}\left(\frac{\partial u_i}{\partial x_j} - \frac{\partial u_j}{\partial x_i}\right)^2}\right|\right] \tag{2.32}$$

$$\nu_{t_{outer}} = \rho K C_{CP} F_{WAKE} F_{KLEB}(y) \tag{2.33}$$

Details on the variables found in these equations can be found in [36]. The Baldwin-Lomax model is suitable for high-speed attached flows with thin boundary layers. Though the BL model is not meant for use with unsteady, separated

flows, it can still provide a quick preliminary approach to solving turbulent eddy viscosity, especially in cases where robustness is more important than capturing flow physics details.

The Spalart-Allmaras (SA) turbulence model is a one-equation model given by:

$$\frac{\partial \bar{\nu}}{\partial t} + V \cdot (\nabla \bar{\nu}) = \frac{1}{\sigma}\left[\nabla \cdot ((\bar{\nu} + \nu)\nabla \bar{\nu}) + c_{b2}(\nabla \nu)^2\right] + c_{b1}\bar{S}\bar{\nu} - c_{w1} f_w \left[\frac{\bar{\nu}}{d}\right]^2 \quad (2.34)$$

The SA model relates the Reynolds stresses to the mean strain. The turbulent eddy viscosity, ν_t, is obtained by solving the above PDE for a related variable, $\bar{\nu}$, where the two quantities are related by $\nu_t = \bar{\nu} f_{v1}$. f_{v1} is a function of $\bar{\nu}$ and the molecular viscosity, ν. c_{b1}, c_{b2}, and c_{w1} are constants, d is distance from the wall, and V is the mean flow velocity; further details can be found in [37]. Essentially, after loose coupling of this equation to the Navier-Stokes equations, the turbulent eddy viscosity can be obtained, from which the shear stress in the moment and energy equations can be evaluated, thus providing closure for all the variables.

2.4.4 Spatial Discretization

In OVERTURNS, the baseline algorithm uses a finite volume approach to discretize Equation 2.18 in space and time; the discrete approximation is shown in Equation 2.35. In the finite volume approach, a fictitious control volume is created around each gridpoint; its boundaries are defined by the midpoints of each line joining the current gridpoint to its neighboring gridpoints. At these boundaries, or "faces", of the control volume, the fluxes are evaluated, thus allowing

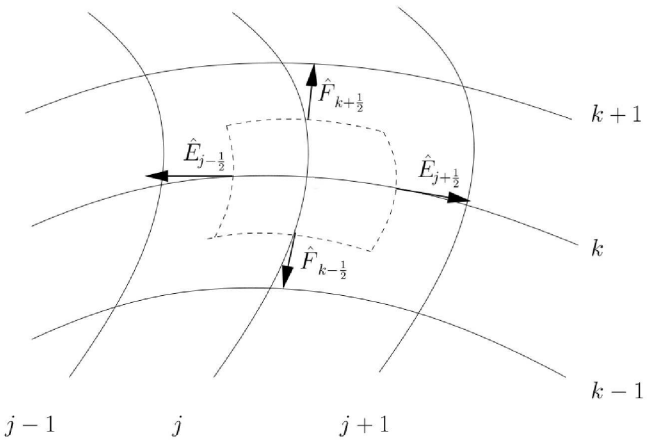

Figure 2.7: Schematic of the computational cell and its boundaries (Ref. 32).

for the conservation equations to be solved within the volume. A schematic is shown in Figure 2.7.

$$\frac{\Delta \hat{Q}}{\Delta t} = -\frac{\hat{E}_{j+\frac{1}{2}} - \hat{E}_{j-\frac{1}{2}}}{\Delta \xi} - \frac{\hat{F}_{k+\frac{1}{2}} - \hat{F}_{k-\frac{1}{2}}}{\Delta \eta} - \frac{\hat{G}_{l+\frac{1}{2}} - \hat{G}_{l-\frac{1}{2}}}{\Delta \zeta} + \hat{S}_{j,k,l} \tag{2.35}$$

where (j, k, l) are the computational indices corresponding to the (ξ, η, ζ) coordinate directions. The $(j \pm \frac{1}{2}, k \pm \frac{1}{2}, l \pm \frac{1}{2})$ subscripts denote the values at the cell face. Thus, in the spatial discretization, the inviscid and viscous fluxes are obtained by calculating the fluxes at the interfaces for every cell (j, k, l) in the computational domain.

For the inviscid terms, the flux at the interface is computed using van Leer's Monotone Upstream-Centered Scheme for Conservation Laws (MUSCL) [38] scheme. This is a two-step upwind scheme in which the wave propagation property of the inviscid equations is accounted for in the flux calculation, thus making it highly stable. The first step involves evaluating the left and right state at each cell interface using a reconstruction from the respective cell centers of each state. The second step is to calculate the fluxes at the interface by defining a local Rie-

mann problem using the left and right states. In TURNS, Roe flux-difference splitting [39] is used to solve for the flux at the interface:

$$F\left(q^L, q^R\right) = \frac{F\left(q^L\right) + F\left(q^R\right)}{2} - \left|\hat{A}\left(q^L, q^R\right)\right| \frac{q^R - q^L}{2} \tag{2.36}$$

In the above equation, $\hat{A}$ denotes the Roe-averaged Jacobian matrix and L and R superscripts indicate the left and right states, respectively. Typically Roe's scheme is modified by Turkel to become the Roe-Turkel scheme [40] in order to better approximate low Mach number flow.

In low-Reynolds flows with thick boundary layers and large amounts of separation, the viscous terms in the spatial discretization cannot be neglected. Thus, an example viscous term of the form:

$$\frac{\partial}{\partial \xi}\left(\alpha \frac{\partial \beta}{\partial \eta}\right) \tag{2.37}$$

is discretized in TURNS using a second-order central differencing scheme:

$$\frac{1}{\Delta \xi}\left[\left(\alpha_{j+\frac{1}{2},k} \frac{\beta_{j+\frac{1}{2},k+1} - \beta_{j+\frac{1}{2},k}}{\Delta \eta}\right) - \left(\alpha_{j-\frac{1}{2},k} \frac{\beta_{j-\frac{1}{2},k} - \beta_{j-\frac{1}{2},k-1}}{\Delta \eta}\right)\right] \tag{2.38}$$

where

$$\alpha, \beta_{j\pm\frac{1}{2},k} = \frac{\alpha, \beta_{j,k} \pm \alpha, \beta_{j\pm1,k}}{2} \tag{2.39}$$

2.4.5 Preconditioning

Since the cyclocopter operates in low-Mach and low-Reynolds Number flight regimes, it is necessary to employ a low-Mach preconditioner to help maintain accuracy and converge the compressible Navier-Stokes flow solver. The discretized

form of the compressible Navier-stokes equations does not converge upon the incompressible solution as Mach number approaches zero. Thus, use of the preconditioner resolves this issue and achieves several specific goals, among which two are listed below.

- Since there is a large difference between eigenvalues in low Mach flows, the solution is computationally stiff and therefore requires more time to reach a steady-state solution. The preconditioner accelerates convergence by bringing the magnitude of the acoustic eigenvalues closer to the convective eigenvalues, thereby reducing stiffness.

- A low-Mach preconditioner removes scaling inaccuracies between dissipation terms. This is most beneficial near the stagnation term and near surface boundary layers, since the preconditioner makes the pressure terms and convective terms more consistent to each other.

2.4.6 Implicit Time Marching and Dual Time-Stepping

The spatial discretization as described earlier solves for the fluxes at the right-hand side (RHS) of equation 2.35. Now, the conservative variables, $\hat{Q}$, can be evolved in time. In most CFD solvers, implicit time marching is preferred over explicit schemes due to the lack of a numerical stability limit. Explicit schemes only solve the governing equations at a later timestep $t + \Delta t$ using information from the current state of the system. However, they require an impracticably small Δt to converge stiff problems while keeping the error bounded, and can diverge with a larger timestep size. Implicit methods, conversely, solve simultaneously at both at the current timestep, t, and the next timestep, $t + \Delta t$. Hence, implicit schemes do not suffer from the same stability problems, and a

larger timestep can be taken to converge the solution faster. When Equation 2.35 is written in a generic discretized 'delta form' using an implicit algorithm, the following expression is obtained:

$$LHS\Delta\hat{Q}^n = -\Delta t RHS \tag{2.40}$$

Where the right-hand side (RHS) represents the fluxes that comprise the "physics" of the problem, and the left-hand side represents the implicit scheme which comprise the "numerics" and determine the rate of convergence. n denotes the current timestep. The implicit algorithm produces a large sparse banded matrix, which is then solved to obtain a solution for $\Delta\hat{Q}^n$. Typically, approximate factorization methods are used to solve such sparse systems.

For time-dependent calculations, such as the unsteady moving mesh problems associated with rotorcraft, dual timestepping [41] may be used to aid in convergence. With dual time-stepping, a series of "pseudo-timesteps" are introduced per physical time step, such that the unsteady problem becomes a pseudo-steady problem. Thus, certain advantages of a steady-state problem are attained. However, care must be taken to ensure that the dual timestepping scheme undergoes enough sub-iterations such that an accurate transient solution is achieved. Typically, a drop in the unsteady residual of two orders of magnitude is sufficient to ensure that each physical timestep is well-converged.

2.4.7 Boundary Conditions

Figure 2.8 shows a schematic of the different types of numerical boundary conditions encountered in the overset blade/background mesh system. The following list describes the various boundary conditions shown in the schematic and their

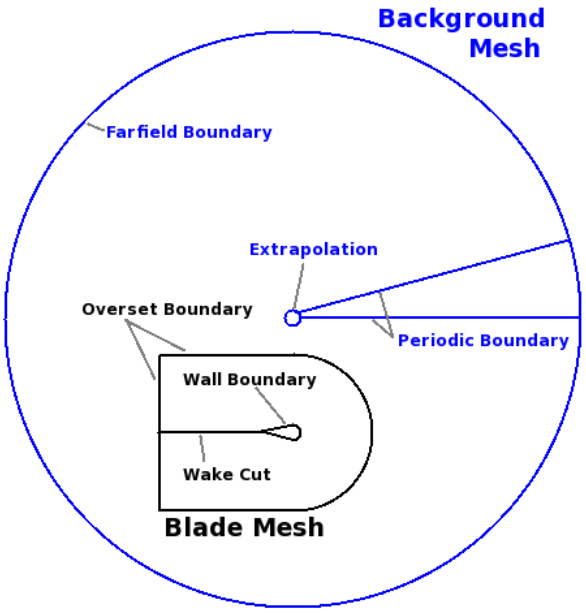

Figure 2.8: Boundary conditions in the overset blade and background mesh system.

treatments in the flow solver.

- Wall Boundary: At the blade surface, a viscous wall boundary condition is used to ensure no slip at the walls. This requires that the fluid velocity at the wall be equal to the surface velocity. Density is extrapolated and pressure is solved based on the normal momentum equation.

- Wake Cut: Behind the trailing edge of the blade and at the root and tip, the grid planes collapse onto each other. Hence, the treatment is such that an average of the solution from either side of the wake cut is used.

- Periodic Boundary: The overlapped periodic boundary in the circular background mesh is used such that numbering scheme in computational space is arbitrary at either end of the mesh. In other words, the solution "re-

peats" from the maximum point in the tangential direction, ξ_{max}, to the first point, ξ_1. A boundary condition vector is not needed, since all information is interior to the mesh. Thus, periodicity is maintained by replacing the data at the edges with their corresponding interior information in the overlap region.

- Extrapolation: The boundary condition around the center of the cylindrical mesh entails a first-order extrapolation of all the surrounding values to the exact centerline of the cylinder.

- Farfield Boundary: The farfield boundary on the background mesh is placed as far away in the radial direction from body surfaces as computationally practical such that the conditions at these mesh points are very close to freestream. Characteristic-based Riemann invariants [42], which are extrapolated from the interior or the freestream and are based on the direction of the velocity vector and sonic velocity, are used to determine these boundary conditions. Hence, this ensures that there are no spurious wave reflections at the boundary. It should be noted that for the 3-D background mesh, the farfield boundary is also applied to the "top" and "bottom" $x - y$ planes of the cylinder.

- Overset Boundary: The overset boundaries are determined by the Implicit Hole-Cutting code, and are used to provide connectivity information between the blade and background meshes. Further details were described earlier in Section 2.2.

2.4.8 Specific Methods used in OVERTURNS

The OVERTURNS structured overset solver uses the diagonal form of the implicit approximate factorization method developed by Pulliam and Chaussee [43] with a preconditioned dual-time scheme to solve the compressible RANS equations. Computations were performed in the inertial frame in a time-accurate manner. A third-order MUSCL scheme with Roe flux difference splitting and Koren's limiter was used to compute the inviscid terms, and second-order central differencing was used for the viscous terms. These were discussed previously in Section 2.4.4. The low-Mach preconditioner [40] based on Turkel's method accelerated the convergence and ensured accuracy of the solution. The Spalart-Allmaras [37] turbulence model for RANS closure was utilized in 3-D calculations. However, due to convergence problems with the Spalart-Allmaras model in the 2-D CFD simulation, the Baldwin-Lomax [36] model was employed. Specific details beyond the scope of this work with respect to the spatial and temporal discretization as well as other numerical schemes used in OVERTURNS can be found in [24].

2.5 Summary

In this chapter, the major steps that must be taken for all CFD approaches were discussed. These steps are enumerated and summarized in detail below:

1. A mesh must first be generated that resolves the geometry and provides sufficient resolution to capture the flow features. For the cyclocopter, the body-fitted curvilinear C-O blade mesh was generated with hyperbolic grid generation, and the cylindrical background mesh was generated with al-

gebraic methods, specifically Vinokur's stretching procedure in the radial and spanwise directions away from the rotor cage.

2. To determine the connectivity information for overset meshes, "donor" and "receiver" cells must be found which are relatively equivalent in size to interpolate information between meshes without loss of too much accuracy. For this work, the Implicit Hole-Cutting procedure of Lakshminarayan was used.

3. A high-fidelity model of the cyclocopter experiment required the unsteady motion of the blade and its deformations to be prescribed. To this end, a global rotational motion was imposed on the blade mesh and the numerical approximation to the four-bar mechanism used by Parsons and Benedict was used to define the pitching motion. Structural deformations were prescribed onto the blade mesh in TURNS using the methodology developed by Sitaraman.

4. The flow solver uses the compressible Reynolds-Averaged Navier-Stokes (RANS) equations, which comprise mass, momentum, and energy conservation, to solve for the flowfield. The Baldwin-Lomax and Spalart-Allmaras models were both used in this work to provide closure to the RANS equations. These equations are then are converted from physical space to computational space via a curvilinear coordinate transformation such that the flux contributions can be defined with respect to adjacent cell faces. The finite-volume approach is used in TURNS for discretization, and cell interface fluxes are evaluated to allow for the conservation equations to be solved within the volume. Preconditioning is employed to help

convergence of the compressible RANS equations at low Mach numbers. An implicit time discretization is used with dual time-stepping to maintain accuracy.

5. Boundary conditions must be prescribed onto the grid before starting the flow solver. Types of boundary conditions used specifically in this work are wall boundaries, wake cuts, periodic boundaries, extrapolations, farfield boundaries, and overset boundaries.

Utilizing the above numerical methods together, a flow solution can be obtained for a desired computational mesh. However, before solving for a complex case such as the cyclocopter, the flow solver must first be validated on simpler geometries.

Chapter 3

Validation of the Flow Solver

To validate the accuracy of the numerical methods as described in the previous chapter, the flow solver must first be run for simpler problems. The intent for this chapter is to gain confidence that the solution algorithm produces correct, physical results. For the cycloidal rotor, if we imagine the chord length to be infinitely small compared with the circumference of the rotor, then essentially the cycloidal pitching motion can be thought of as a symmetric airfoil pitching in freestream. Thus, the chapter will consist of three validation sections, performed with the 2-D flow solver assuming infinite span:

- Steady flow with freestream conditions at different angles of attack, simulated at Cyclocopter MAV-scale Reynolds numbers. This essentially corresponds to a non-pitching cycloidal rotor with infinitely small chord-to-rotor-circumference ratio.

- Unsteady pitching motion for a symmetric airfoil. However, an extensive literature search did not reveal any suitable validation cases for a purely pitching airfoil at low Reynolds number undergoing dynamic stall. Thus, due to the dearth of such experiments, a higher Reynolds number case is

used for validation.

- Unsteady rotational motion of a symmetric airfoil at low Reynolds numbers. This examines the capabilities of the solver to produce accurate results at high angles of attack and explores the highly separated flowfield characteristic of this type of unsteady blade motion. As there were no MAV-scale cycloidal rotor cases in experiment for comparison, a VAWT result is used.

CFD simulations were also performed for an unsteady pitching NACA 0010 airfoil at $Re = 30,000$, $M_\infty = 0.047$ corresponding to the flight regime of Benedict et al.'s experiments [14], there was no experimental validation for this work. The predictions of unsteady time histories for C_l, C_d, and C_m from this simulation are shown in Appendix B. Without verification from experiment, though, the results presented in that section should only be treated as computational predictions and not definitive, accurate results.

3.1 Steady Airfoil Validation

The low-Reynolds number airfoil experiments of Lutz et al. [44] were used to validate the steady 2-D solver. Lutz took lift and drag measurements as a function of angle of attack for a symmetric NACA 0009 airfoil at $Re = 50,000$ and $M_\infty \approx 0.02$.

A 2-D TURNS steady simulation was undertaken with low-Mach preconditioning and the Baldwin-Lomax turbulence model for determination of eddy viscosity. The grid was a 209×154 C airfoil mesh with outer boundaries at 15 chords away from the blade surface, as shown in Figure 3.1. The clustering at

the nose and the trailing edge are displayed in detail in 3.1(c) and 3.1(d). The timestep size employed was $\Delta t = 2.0$ and the simulation was run for $50,000$ iterations or until a drop in the residual of three orders of magnitude was achieved.

The results obtained from the simulation and their comparison with experimental data are shown in Figure 3.2(a), which plots the coefficient of lift as a function of angle of attack; and Figure 3.2(b), the drag polar. As seen from the figure, the computational results correlate very well with experiment. At angles lower than $\alpha = 3^\circ$ in the experiment, the slope of the lift curve is much less than the theoretical inviscid lift slope ($dC_l/d\alpha = 2\pi$ for a flat plate) due to nearly completely laminar flow with correspondingly thick boundary layer. This phenomenon is captured well in the CFD results, but for slightly lower magnitudes than obtained from experiment. From angles $3^\circ < \alpha < 7^\circ$, a laminar separation bubble forms and moves upstream with increasing angle of attack, causing a steep increase in C_l followed by a region of constant 2π lift slope; this is captured well by CFD. As the airfoil nears stall at angles above $\alpha = 7^\circ$, however, the CFD results increasingly err away from experiment. Past $\alpha = 10^\circ$, the solver cannot predict the post-stall performance well. Indeed, it is very difficult for steady numerical simulations to predict separated flow in post-stall flight regimes.

For the drag polar plot, the results from TURNS again capture C_l vs. C_d values very closely as compared to experimental measurements. The subcritical range between $-0.2 < C_l < 0.2$ is predicted extremely well by CFD due to to the predicted very small values of turbulent viscosity. For the region where the formation of the laminar separation bubble and subsequent turbulent reattachment occurs between $-0.5 < C_l < -0.2$ and $0.2 < C_l < 0.5$ TURNS does not capture the experimental trend as well. This was seen also in 3.2(a), where the

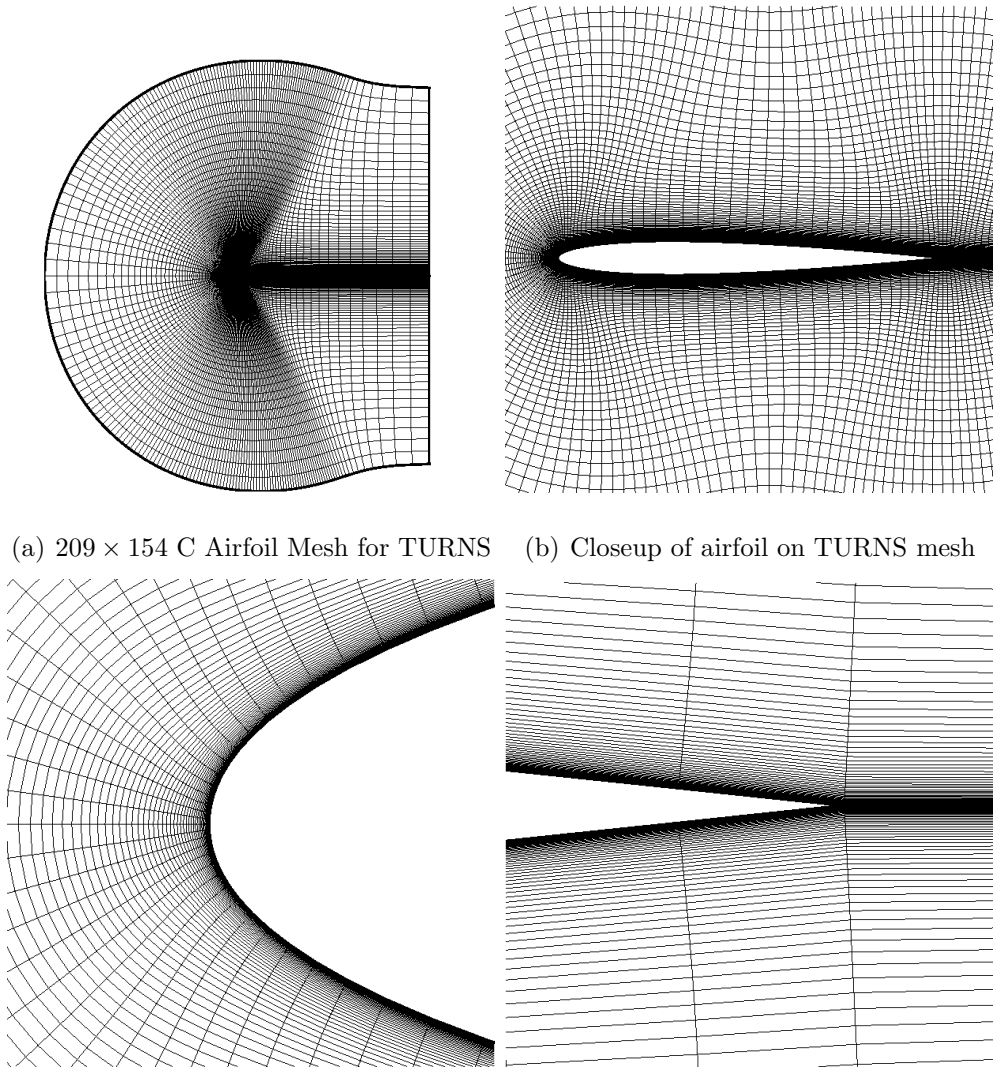

(a) 209×154 C Airfoil Mesh for TURNS

(b) Closeup of airfoil on TURNS mesh

(c) Closeup of leading edge

(d) Closeup of trailing edge

Figure 3.1: Blade meshes used for validation of TURNS flow solver against the Lutz et al. NACA 0009 steady airfoil case.

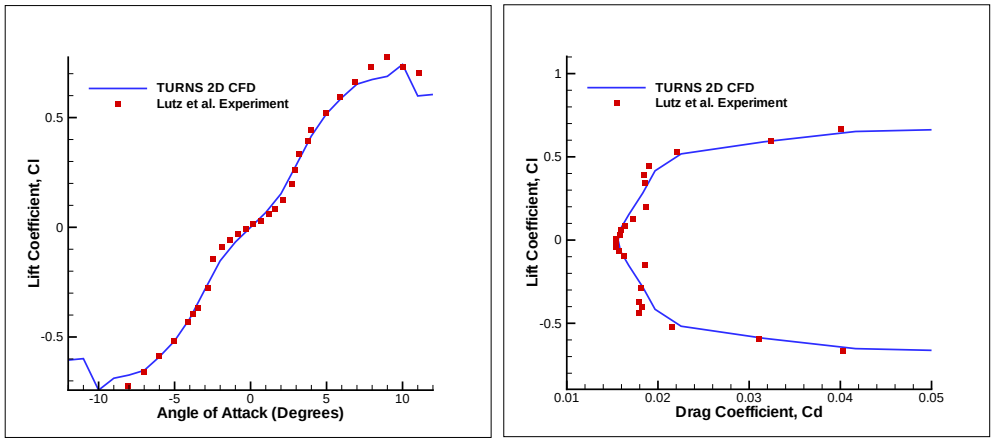

(a) Lift Coefficient vs. Angle of Attack (b) Drag Polar

Figure 3.2: Comparison of CFD vs. Experiment for a steady NACA 0009 airfoil at $Re = 50,000$, $M_\infty = 0.02$

magnitude of lift was slightly overpredicted in the region with the formation of the laminar separation bubble. In addition, contributing to the inaccuracy in this region is an underprediction of drag for $0.016 < C_d < 0.018$ and an overprediction for $0.018 < C_d < 0.02$. For regions below $C_l < -0.5$ and above $C_l > -0.5$ until stall, TURNS results correlate closely with experiment. Overall, TURNS performs extremely well in predictions of symmetric airfoil performance for steady flow at low Reynolds numbers.

3.2 Unsteady Pitching Airfoil Validation

The experimental studies of McAlister et al. [45] and the numerical studies of Tuncer et al. [46] were used to validate the accuracy of TURNS for pitching airfoils in freestream. McAlister used a NACA 0012 airfoil undergoing pitch oscillations about its quarter-chord, where its motion is defined by the equation:

$$\alpha = \alpha_{min} + \frac{1}{2}(\alpha_{max} - \alpha_{min})(1 - \cos\omega t) \tag{3.1}$$

where α_{min}, the minimum angle attained in the oscillation, is 4.86° and α_{max}, the maximum angle attained in the oscillation, is 24.74°. As seen from the equation, the variation in blade motion over time is sinusoidal. The Reynolds number is 0.98×10^6, the freestream Mach number M_∞ is 0.072, and ω, the frequency of the motion, is attained by the equation for reduced frequency, k, as discussed in the nomenclature section. For the case tested in this work, $k = 0.099$.

Tuncer conducted a full viscous flow analysis for McAlister's pitching airfoil based on the unsteady, incompressible RANS equations with negligible body forces. Tuncer reformulated the RANS equations to account for vorticity generation, convection and diffusion, eventually arriving at the vorticity transport equation in a rotating frame attached to the solid body. For discretization, he used a first-order backward difference scheme for the unsteady term, a second-order upwind differencing scheme for convection, and a second-order central for the diffusion terms. The numerical solution was based on the successive line under-relaxation scheme on an 80×60 gridpoint blade O-mesh with a cylindrical coordinate system. The Baldwin-Lomax turbulence model was used to provide closure to the RANS equations.

Similarly, TURNS was also run with the Baldwin-Lomax turbulence model. The simulation was completed as a second-order time-accurate calculation with 10 sub-iterations per physical timestep, along with the other numerical details the same as described earlier. The grid for this simulation is extremely similar to the one used for the steady calculation, except for a NACA 0012 geometry.

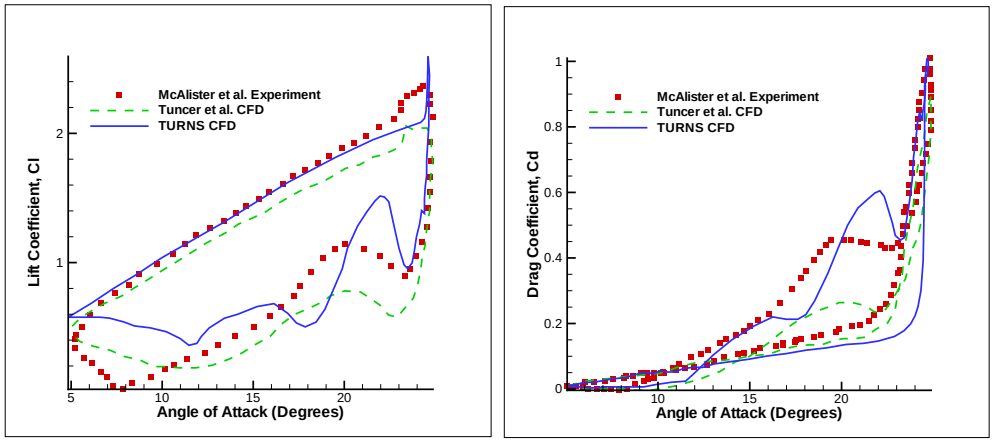

(a) Lift Coefficient, C_l (b) Drag Coefficient, C_d

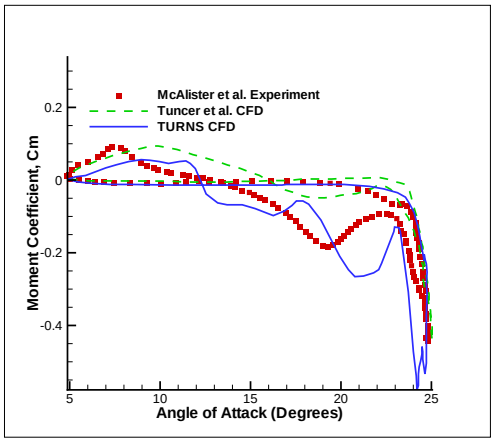

(c) Moment Coefficient, C_m

Figure 3.3: Comparison between numerical and experimental solutions for an unsteady pitching NACA 0012 at $Re = 0.98 \times 10^6$ and $M_\infty = 0.072$.

It should be noted that this grid has a higher resolution than Tuncer's grid with clustering at the leading and trailing edges such that more detailed flow features could be captured. The comparison between McAlister's experiment, Tuncer's numerical result and TURNS output is given in Figure 3.3.

From the figure, it can be seen that the TURNS results match very closely with experiment. During the upstroke, the linear trends observed in both the

lift and moment coefficients are better predicted by TURNS (with respect to experimental data) than Tuncer's simulation. As the leading edge vortex forms near $\alpha = 25°$, TURNS captures but overpredicts the peak in lift and moment; it predicts the peak in drag well, but does not capture the upper hysteresis loop. As the leading edge vortex travels down the chord of the airfoil, it "bursts" at the trailing edge and sheds clockwise vorticity; this drop is also caught by TURNS. However, the second local maximum in lift, drag, and negative moment, obtained on the downstroke at around $\alpha = 22°$, is overpredicted by TURNS, whereas it was previously underpredicted by Tuncer's results. This local maximum is due to the suction generated by the trailing edge vortex, and Tuncer offers a reason as to why this is not well predicted in the numerical simulation: the Baldwin-Lomax turbulence model does not perform well in the wake region.

Past the shedding of the trailing edge vortex, the lift curve steadily decreases in experiment due to the reattachment of the trailing edge and the formation of secondary vortex structures. The flow reattaches on the upper surface past $\alpha = 7°$, and the lift reaches a global minimum before increasing. Again in both numerical models, the lift curve is not predicted well here, although the drag and moment curves are slightly improved. Due to the fully turbulent flow assumption, the flow solvers may be forcing the reattachment of the boundary layers earlier than experiment, thus leading to an overpredicted global maximum. After the suction on the leading-edge is established, then both flow solvers gravitate towards the steady-state value of lift, drag, and moment. Overall, though, the correlation between TURNS and experimental results are fair.

3.3 Validation of 2-D Unsteady Flow Separation from Airfoil Rotation

The experimental results for dynamic stall on a VAWT were used to validate TURNS' predictive capability in a highly separated flowfield. Such a flow environment is characteristic of airfoil movement around a rotor cage with a high chord-to-rotor-circumference ratio. Ferreira et al. [8] at the Delft University of Technology conducted Particle Image Velocimetry (PIV) measurements to visualize flow within an H-Darrieus type straight-bladed vertical axis wind turbine with no blade pitch, originally developed by Coene [47]. The experimental setup consisted of a single NACA 0015 airfoil with a chord of 0.05 m, a rotor diameter of 0.4 m, a rod with a diameter of 0.05 m at the rotational axis, and an aspect ratio of 20 to produce an almost 2-D case. Flow measurements were taken for two different mean Reynolds numbers, 52000 and 70000 and three tip speed ratios, $\lambda = 2,3,4$, corresponding to each. Furthermore, Ferreira conducted a CFD simulation [48] using Fluent (a commercial CFD package) for a 7.5 m/s, $\lambda = 2$, and 52000 mean Reynolds number case using different turbulence models and varying spatial and temporal resolution to validate against PIV data.

A blade shape-conforming mesh of 209 x 94 points on a circular background mesh of 321 x 251 points with a five-point overlapped boundary condition was used in OVERTURNS for verification of this case. A schematic of the computational domain as well as the overset grid system is shown in Figure 3.4(a) and 3.4(b), respectively. The wind tunnel walls are not replicated in the OVERTURNS simulation, as Ferreira et al. stated that the effect of the walls was negli-

gible on the numerical results. OVERTURNS was run with the Spalart-Allmaras turbulence model for 10 blade revolutions until the simulation converged upon a periodic solution.

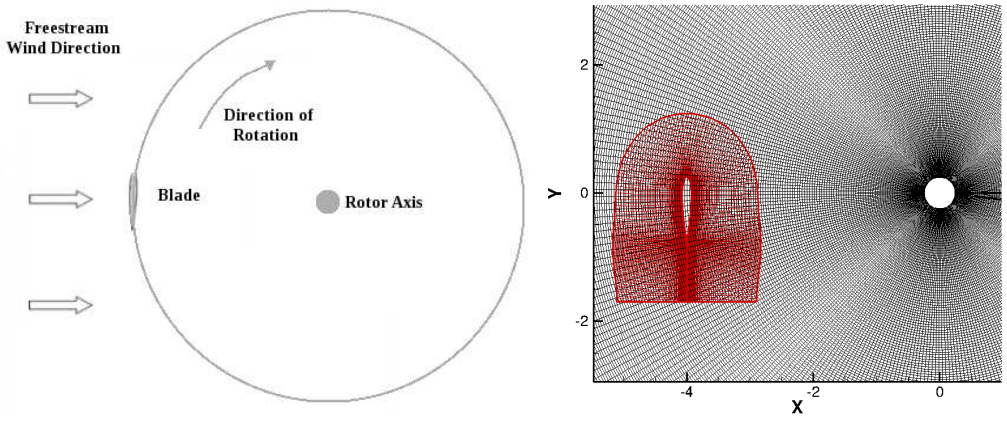

(a) Schematic (b) Overset mesh system

Figure 3.4: Schematic and Computational Mesh for the Vertical Axis Wind Turbine

3.3.1 Dynamic Stall Flow Visualization

Figure 3.5 shows a comparison of vorticity contours between the PIV results of Ferreira et al. and the OVERTURNS CFD results for various azimuthal angles along the cycloidal rotor cage. Figure 3.6 displays the comparison for azimuthal angles of 90° and 98° in more detail. Note that in this case, contrary to the convention displayed in Figure 1.1 and used in all other sections, the azimuthal angle is measured clockwise rather than counterclockwise from the $-y$ axis. It can be seen from the vorticity contours that OVERTURNS accurately simulates the dynamic stall observed through PIV for all angles. The numerical results successfully capture the details in the vortex structure on the upper surface of the airfoil that are indistinct in the PIV measurements, and resolve the

region of negative vorticity past the trailing edge of the airfoil. Furthermore, the magnitudes obtained through OVERTURNS are comparable with experimental results, one notable exception being the region of strong vorticity from mid-span to 75% chord in the $\Psi = 98°$ case which is underpredicted by CFD.

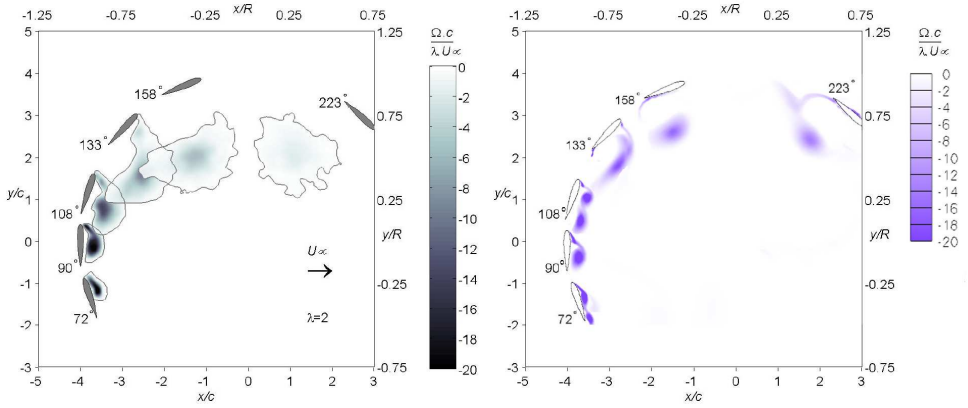

(a) PIV Measurements of Ferreira et al. (b) OVERTURNS results

Figure 3.5: Comparison of vorticity contours between the PIV results of Ferreira and CFD for six different azimuthal angles.

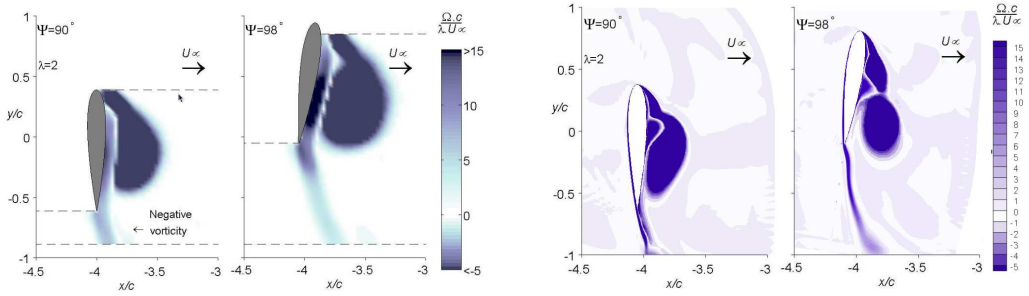

(a) PIV Measurements of Ferreira et al. (b) OVERTURNS results

Figure 3.6: Comparison of vorticity obtained by PIV and OVERTURNS numerical results for $\Psi = 90°, 98°$.

3.3.2 Comparison of Normal and Tangential Force Coefficients

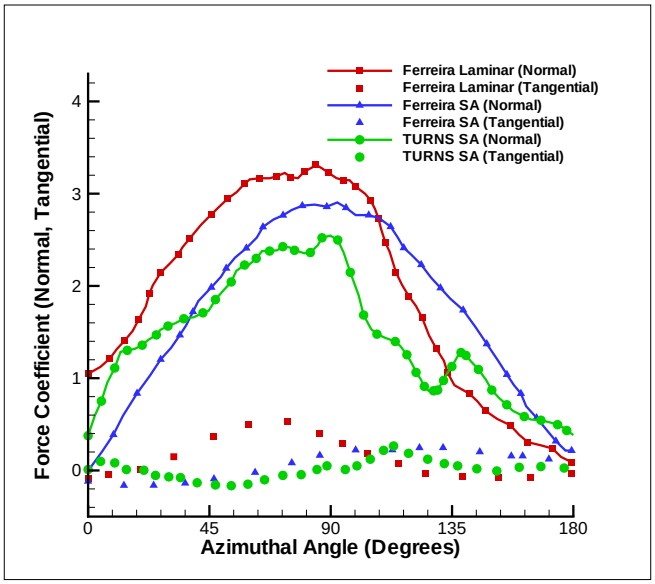

Figure 3.7: Comparison of C_N and C_T on the VAWT for the Spalart-Allmaras Turbulence Model from $\Psi = 0°$ to $180°$

Figure 3.7 shows the comparison of tangential (C_T) and normal (C_N) force coefficients (non-dimensionalized by the chord length of the airfoil and the rotational velocity) for Ferreira's CFD results assuming laminar flow, Ferreira's CFD results using the SA model, and OVERTURNS using the SA model. Though there is no unsteady time history provided by Ferreira for the experimental results, Ferreira states that his CFD simulations with the laminar model most closely matched experiment. From the figure, it can be seen that OVERTURNS captures the magnitude of the tangential force well, but the trend is closer to Ferreira's SA model results. For the normal force, OVERTURNS initially follows the trend of Ferreira's laminar results, but then follows the SA results past an azimuthal angle of $\Psi = 45°$. It underpredicts the peak normal force of ei-

ther Ferreira's SA or laminar models at $\Psi = 90°$. After 90° azimuth, it again begins following the trend of the laminar model. Despite the underprediction of magnitude, the TURNS results may better predict unsteady shedding than Ferreira's SA results and may be closer to experiment since it mostly follows the laminar model. To reinforce this, Ferreira stated that his laminar simulation better captures the development of the large leading edge separated vorticity and the rolling up of the counter-clockwise vorticity at the trailing edge past the $\Psi = 90°$ location which he observed in experiment; this phenomenon manifests as a rapid drop in C_N for the laminar time history in Figure 3.7. TURNS predicts this drop as well, despite the fact that using the SA model assumes fully turbulent flow. Ferreira previously stated that his SA simulations had suppressed the development of the leading edge separation at this azimuthal location and therefore deviated from experiment. However, since OVERTURNS captures this even with a fully turbulent assumption, OVERTURNS is seen to correlate better with Ferreira's laminar results and therefore predict results closer to experiment.

3.4 Summary

As seen from this section, TURNS predicts reasonably well the performance of steady airfoils at low Reynolds numbers and unsteady pitching airfoils. It was shown that:

- While TURNS captures the trends for the steady NACA 0009 airfoil at $Re = 50,000$ extremely well, the region between $-5° < \alpha < 5°$ where the laminar separation bubble forms is slightly less well captured as the magnitude of C_l is slightly overpredicted, and C_d is slightly under-, then

overpredicted for this region.

- For the unsteady pitching airfoil results, the linear trends observed during the upstroke in the lift and moment coefficients correlate very closely with experiment, and are predicted better than Tuncer's simulation. TURNS overpredicts the lift and moment peaks, however, and underpredicts the drag peak. On the downstroke, it does not captured regions of separated flow well, and as a result deviates somewhat from experiment. Overall, however, trends match relatively well between TURNS and McAlister's experiments.

- The unsteady airfoil rotation to test TURNS' predictive capability for highly separated flow showed that quantitatively, TURNS performed well in capturing the flowfield seen in Ferreira's PIV results. Qualitatively, TURNS predicted C_T well, and TURNS more closely followed the laminar (and therefore experimental) trend in the unsteady C_N time history despite using the SA model with a fully turbulent assumption. This suggests that this assumption is not altogether inappropriate for the TURNS flow solver in the low Reynolds, low Mach unsteady flow environment characteristic of both VAWTs and MAV-scale cycloidal rotors.

The validation of these simple cases allows the creation of a basic framework upon which more difficult cases can be tested, with the confidence that the results produced by the numerical solver are physically accurate. In the following chapter, numerical simulations of the cyclocopter will be described in detail and the performance results from the solver will be compared with experiment.

Chapter 4

Comparison of Cycloidal Rotor CFD Results with Experiment

With validation of the solver achieved from the previous chapter, the current chapter describes CFD pertaining specifically to the cyclocopter, including numerical methods employed to emulate the experiment to a high level of accuracy. Comparisons between CFD predictions and experimental measurements will be presented in the latter sections.

4.1 Experimental Setup for Validation

For the cycloidal rotor, experimental results of Benedict et al. [14] were used to validate the predictions of the 2-D and 3-D flow solvers. Benedict et al. tested both twin- and quad-rotor MAV-scale cyclocopter configurations with two to five blades per rotor cage. He used a symmetric airfoil with design attributes listed in Table 4.1. Figure 4.1 shows the experimental setup. The blades were constrained at the root and tip onto two carbon fiber end plates connected by a carbon fiber rod in the center. Measurements of vertical and sidewise force

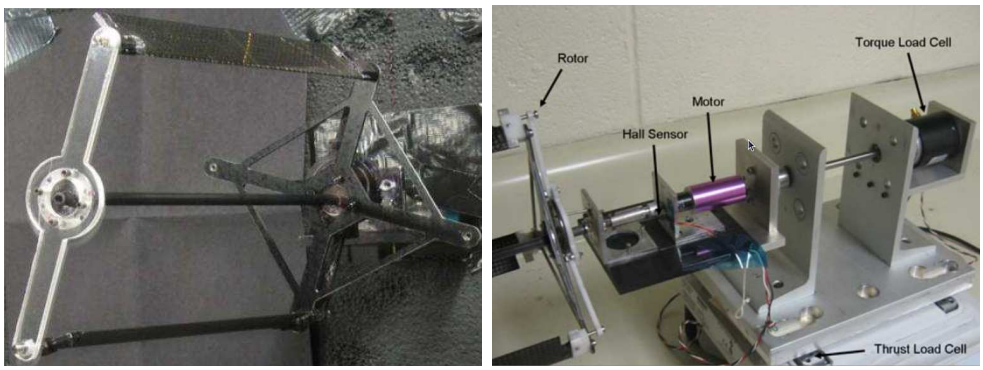

(a) 2-bladed cycloidal rotor cage (b) Experimental measurement setup

Figure 4.1: Experimental setup of Benedict et al. (Ref. 16)

were obtained on the cyclocopter using a thrust load cell. A torque cell was used to measure the torque which, when combined with Hall sensor measurements of the rotor RPM, allowed for calculation of total power. In turn, the aerodynamic power was obtained by taking the total measured power and subtracting the power consumed by spinning the structure without blades.

Parameter	Value
Chord Length	$0.0274m$
Radius	$0.0706m$
Span	$0.1411m$
Number of Blades	$2-5$
Rotating Speed	$400-2000RPM$
Maximum Pitch Angle	$25°-40°$
Airfoil Section	NACA 0010

Table 4.1: Cyclocopter design parameters based on the experimental setup of Benedict et al.

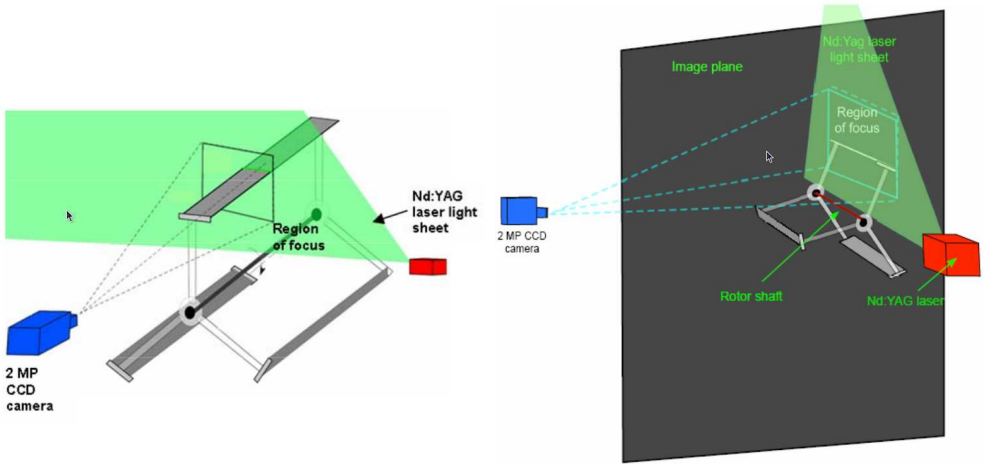

(a) PIV setup for studying chordwise flow (b) PIV setup for studying spanwise flow

Figure 4.2: Schematic for PIV setup of Benedict et al. (Ref. 16)

4.1.1 Flow Visualization

Benedict et al. conducted Digital Particle Image Velocimetry (DPIV) measurements to visualize the flow through the cycloidal rotor cage. The laser light sheet was placed at two different orientations: at the mid-span of the rotor to capture chordwise flow velocities, and parallel to the span of the blade to study trailed vortices as well as wake contraction. The camera was placed orthogonal to the laser light sheet in both the cases; the schematic is shown in Figure 4.2.

To capture flow velocities, Benedict et al. tracked the position of the seed particles. Sampling was taken at a rate up to 15 Hz, and this correlated with the speed at which the laser light sheet was capable of being pulsed. This was then synchronized with rotor frequency to illuminate planes in the rotor flowfield at any required azimuthal angle. Hence, a time history of the particle motion as well as a time average could be constructed from combining the separate frames. To process the image, Benedict used deformation grid correlation, which adds

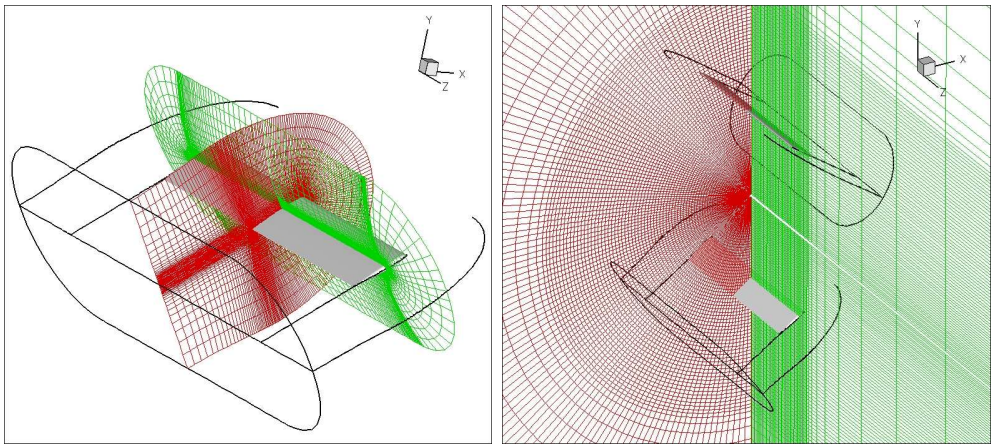

(a) Blade mesh (267×181×51) (b) Background mesh (247×168×255)

Figure 4.3: Three-dimensional blade and background meshes for the cyclocopter.

shearing to the window shifting technique to measure the high velocity gradients inside rotor wake flows.

4.2 2-D and 3-D Grid Systems

To simulate the Benedict et al. experimental setup, the 3-D flow solver was run on both "fine" and "coarse" overset background and blade meshes. These are shown in Figure 4.3, and the size of these grids are denoted in Table 4.2.

The number of points in the "fine" body-fitted curvilinear C-O type blade mesh was chosen such that there was enough resolution to capture flow phenomena near the blade. The points in the cylindrical background mesh were distributed to provide sufficient refinement for resolution of tip vortex evolution 4-5 chords below the rotor cage, as well as allow for a seven-point overlapped periodic boundary condition per circular plane. However, as this is computationally expensive to run, every other point was removed in the spanwise direction in the blade mesh, and every other spanwise and radial point was taken away for

the background mesh to comprise a "coarse" overset mesh. This "coarse" mesh was used to predict rotor performance and compare to the thrust and power values obtained from experiment. However, from Figure 4.4, which compares forces obtained from one cyclocopter blade starting at $\Psi = 0°$ with 40° pitch amplitude and 1400 RPM, it can be seen that the time histories of the coarse and fine mesh are nearly identical, and this indicates grid convergence.

The 2-D grids were taken at the mid-span section of the fine mesh. 2-D runs were used to gain quick insight into the physics of the flowfield without the computational cost of the 3-D runs. In addition, when compared to the 3-D runs, the 2-D runs provide an anchor to explore the effect of three-dimensionality on the flowfield, as 2-D assumes infinite span. As will be discussed later in Chapter 4.4, while the 2-D results provide comparable results to 3-D with regard to performance predictions, the qualitative comparison of the flowfield shows significant difference in flow phenomena captured.

Though the cylindrical background mesh was used for all cyclocopter CFD runs, another background grid was generated with the purpose of capturing more

		Coarse Mesh	Fine Mesh
Blade	Tangential	267	267
	Normal	51	51
	Spanwise	181	91
Background	Tangential	247	247
	Radial	168	84
	Spanwise	255	128

Table 4.2: Number of grid points in both fine and coarse background and blade meshes.

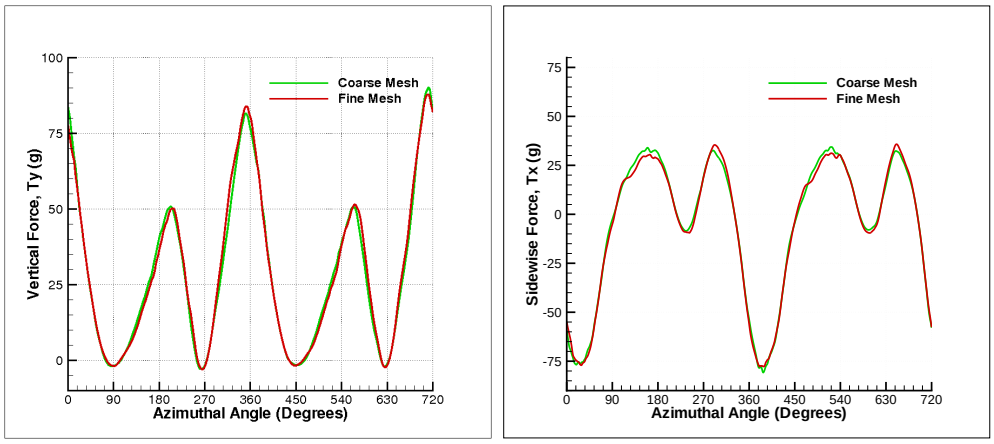

(a) Vertical Force, T_y (b) Sidewise Force, T_x

Figure 4.4: Comparison between forces obtained from coarse and fine meshes for one blade.

detailed flow phenomena in the wake. This mesh utilizes a cylindrical shape for the "top" of the cyclocopter cage, but an extruded trapezoid at the bottom with more gridpoints to provide more consistent cell volume in the wake region. Details of this mesh can be found in Appendix C.

4.3 Cyclocopter Blade Deformations

Deformations caused by the rotation of the cyclocopter were calculated using the computational structural dynamics (CSD) code provided by Benedict et al. [21], as discussed earlier in section 2.3.3. As aerodynamic forces were found to contribute less than 10% of the total force as compared with centrifugal forces, their effects were neglected.

Specific to the current cyclocopter analysis, the blades tested by Benedict had NACA 0010 cross-sections and were fabricated from carbon fiber with a foam core, of which detailed structural testing was conducted to determine the

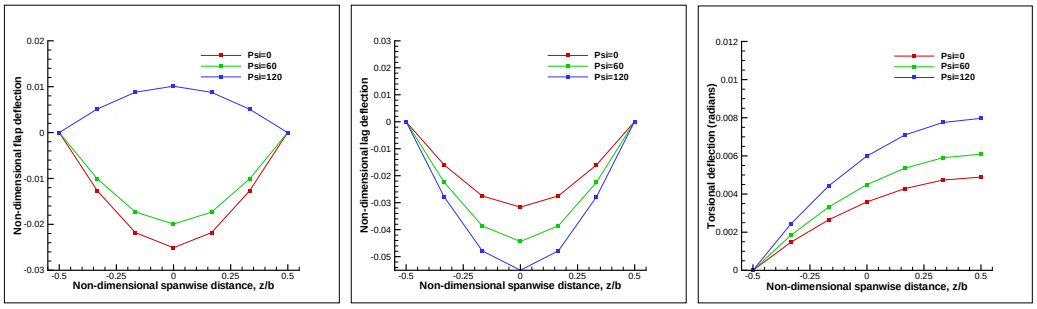

(a) Radial Bending (b) Tangential Bending (c) Torsion

Figure 4.5: Structural deformations generated by the CSD code of Benedict et al. for 1400 RPM, 40° pitch amplitude.

bending and torsional stiffness. With these blades operating at 1400 RPM with 40° collective pitch amplitude, the spanwise deflections from the CSD code at different azimuthal locations are shown in Figure 4.5. All the tangential bending, radial bending, and torsion values are non-dimensionalized by chord. Since the blades are fairly rigid and the tests were run at relatively low RPMs, the geometrical deflections due to centrifugal force are small. However, the blade deformations cannot be neglected for a more flexible blade and while operating at higher RPMs. Figure 4.6 compares the blade shape and chordwise mesh before and after the deformations have been prescribed for the above case.

In addition, the four-bar pitching motion prescribed into the solver based

Pitch Amplitude, θ	L_2
25°	0.1811
30°	0.2126
35°	0.2441
40°	0.2756

Table 4.3: Table of L2 pitch linkage values based on pitch amplitude.

on the lengths of the pitch linkages are described below. For equations 2.6 - 2.8 presented in Chapter 2, the L_1, L_3, and L_4 linkage lengths specific to the cyclocopter are 3, 3.0165 and 0.4331 respectively. L_2 varies with pitch amplitude and is consistent with the L_2 offset distance described earlier in section 2.3.2; its values are shown in Table 4.3.

4.4 Performance Comparisons

The performance predicting capability of the 2-D and 3-D CFD solver was tested by undertaking an RPM and a collective pitch angle sweep simulation and comparing the predicted performance data with the available experimental data. The RPM sweep spanned from 400-2000 RPM, corresponding to $5500 < Re < 28000$ and $0.01 < M_{rot} < 0.047$ for a fixed 35° pitch; the collective pitch angle sweep extended from 25° to 40° maximum pitch amplitude at a fixed 1400 RPM. In each case, the CFD simulations were run for at least six revolutions or until a

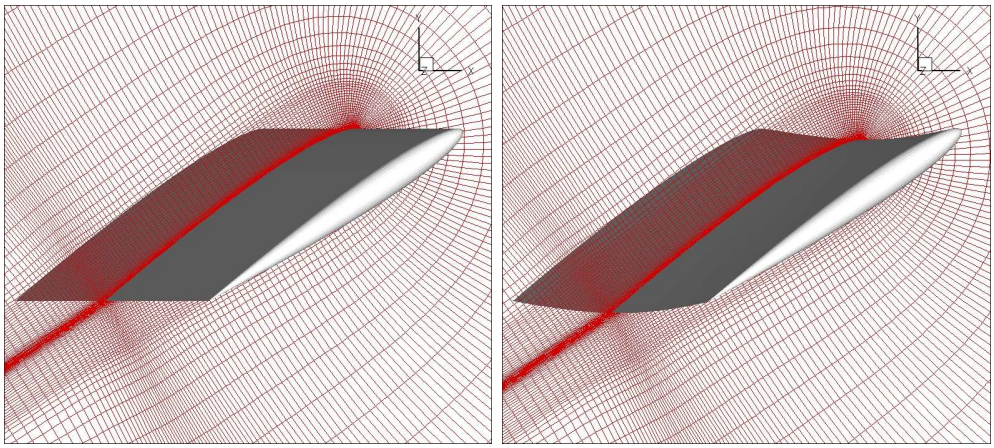

(a) Undeformed blade mesh (b) Deformed blade mesh

Figure 4.6: Comparison between deformed and undeformed blade meshes at 1400 RPM, 35° pitch amplitude.

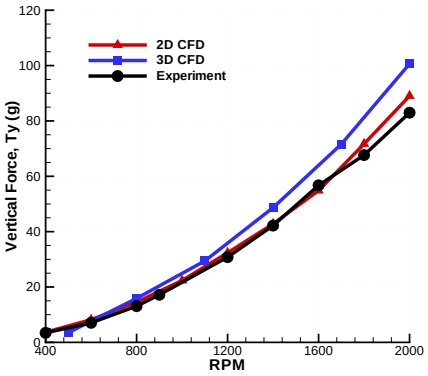

(a) Vertical force, T_y

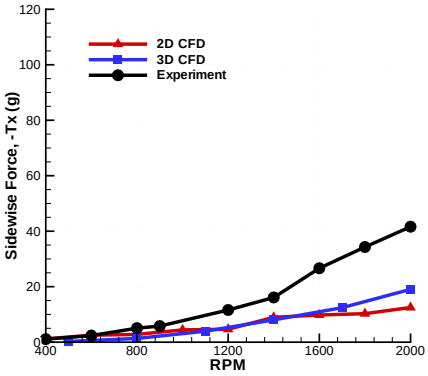

(b) Sidewise force, T_x

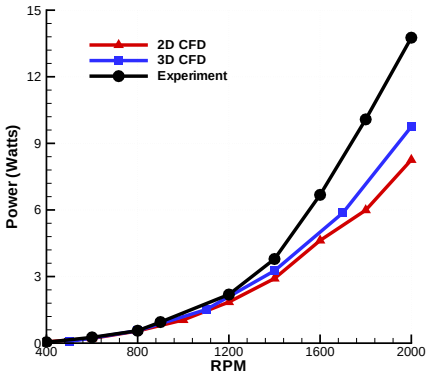

(c) Aerodynamic power

Figure 4.7: Comparison of CFD vs. experiment for 400-2000 RPM at 35° pitch.

converged and fairly periodic solution was achieved.

4.4.1 Thrust and Aerodynamic Power Comparisons

Figures 4.7(a)-(c) show the vertical force, sidewise force, and aerodynamic power comparisons between CFD and experiment for both the 2-D and 3-D RPM sweeps at 35° pitching amplitude with a two-bladed configuration. From the plots, it can be seen that vertical force predicted by CFD corresponds well with

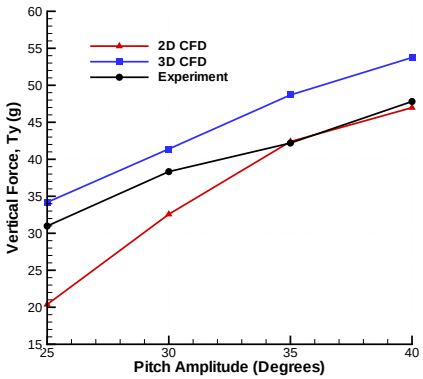

(a) Vertical force, T_y

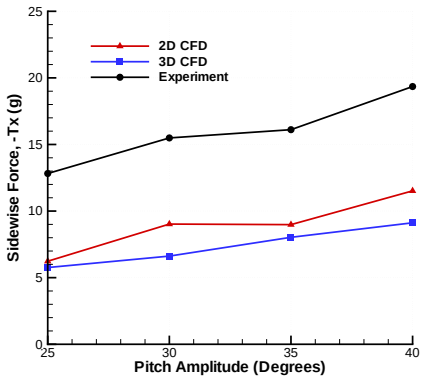

(b) Sidewise force, T_x

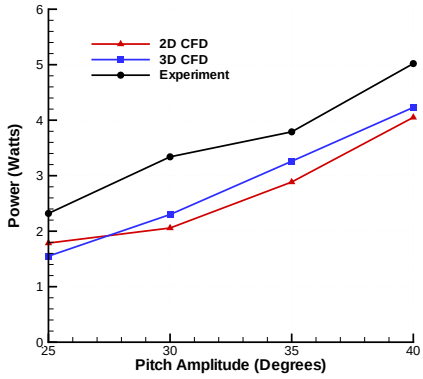

(c) Aerodynamic power

Figure 4.8: Comparison of CFD vs. experiment for $25° - 40°$ pitch at 1400 RPM.

experiment for both the 2-D and 3-D models: within 15% for all RPMs. For sidewise (or horizontal) force, which acts in the $-x$ direction with respect to the axes presented in Fig. 1.1, the 3-D model largely follows the 2-D model and underpredicts the sidewise force. The 2-D model can capture the inflow through the rotor cage in only an $x - y$ planar cut through the rotor cage, and assumes that the same inflow distribution exists for all spanwise stations, while the 3-D model can capture the distribution of inflow across the span as well. However,

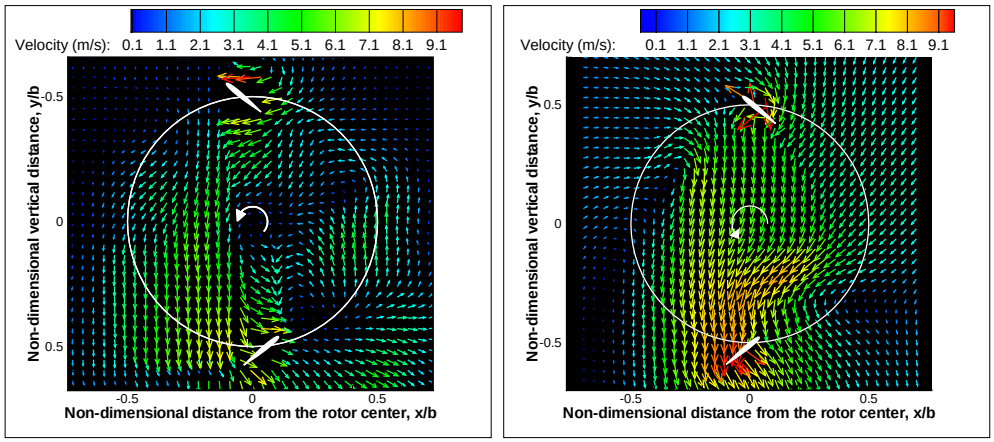

(a) DPIV results at $\Psi = 0°$ (b) 2-D CFD Results at $\Psi = 0°$

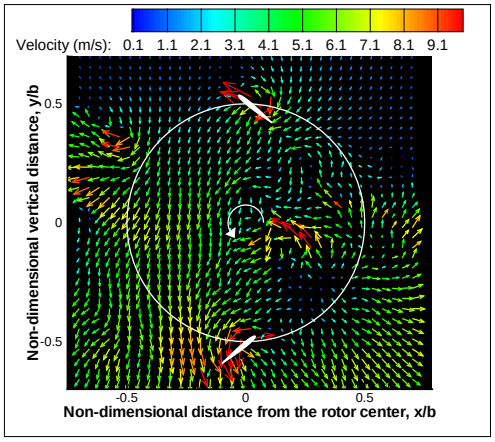

(c) 3-D CFD results at $\Psi = 0°$

Figure 4.9: Mid-span velocity vectors inside the 2-bladed rotor cage at 1400 RPM, 40° pitch amplitude, $\Psi = 0°$.

despite the inability of the 2-D model to capture this non-uniform spanwise inflow as well as induced velocity, the 2-D model is fairly consistent with the 3-D model and performs well until about 1600 RPM. This indicates that the mean spanwise inflow value predicted by the 2-D solver is relatively consistent with 3-D results, and roughly corresponds to an average of the inflow values at every spanwise blade station as predicted by the 3-D solver. Thus, the assumption of infinite span in the 2-D solver may not be entirely inappropriate for performance

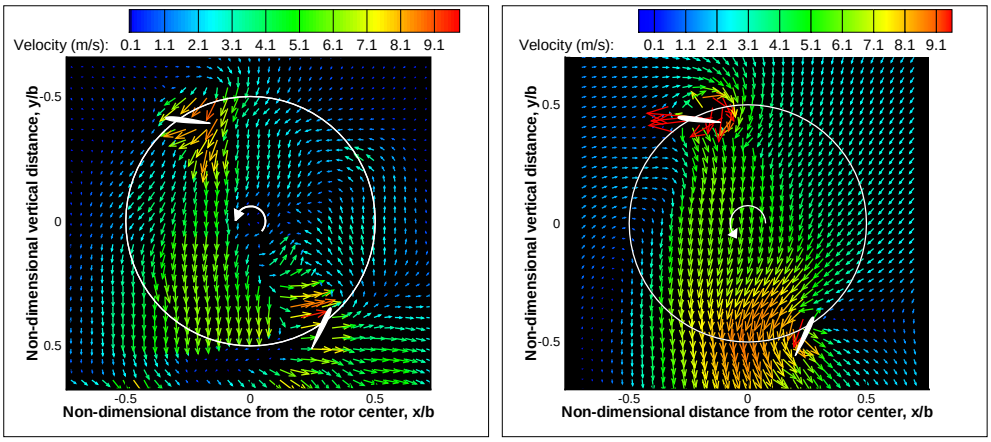

(a) DPIV results at $\Psi = 30°$ (b) 2-D CFD Results at $\Psi = 30°$

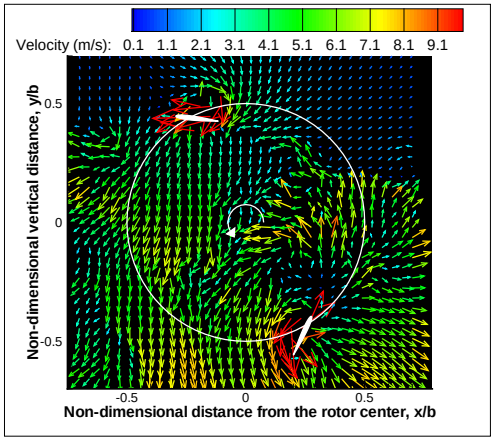

(c) 3-D CFD results at $\Psi = 30°$

Figure 4.10: Mid-span velocity vectors inside the 2-bladed rotor cage at 1400 RPM, 40° pitch amplitude, $\Psi = 30°$.

calculations.

Figure 4.8 shows the vertical and sidewise forces and aerodynamic power generated from the collective pitch angle sweeps at 1400 RPM for two blades. For the vertical forces, the 3-D model somewhat overpredicts while the 2-D CFD underpredicts for smaller collective angles, but the 2-D captures both 35° and 40° pitch amplitude to within 5% accuracy. The sidewise force is again underpredicted for all values of pitch amplitude, mirroring the RPM sweep. For

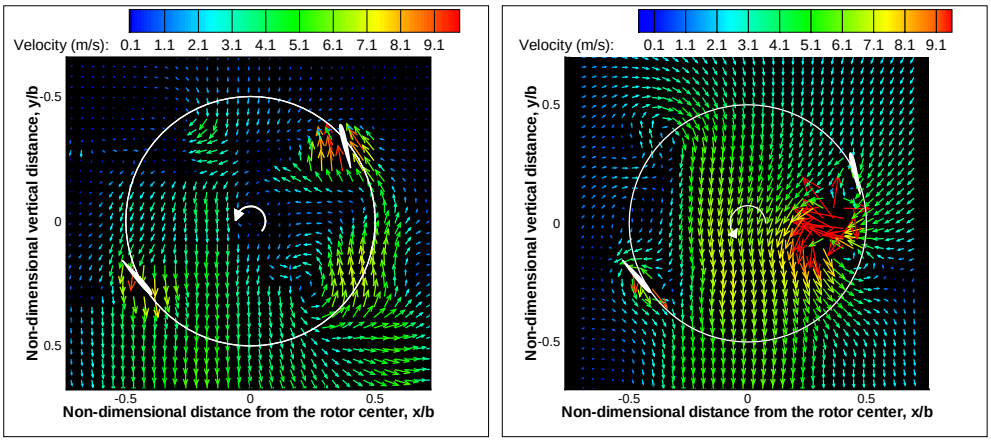

(a) DPIV Results at $\Psi = 120°$ (b) 2-D CFD Results at $\Psi = 120°$

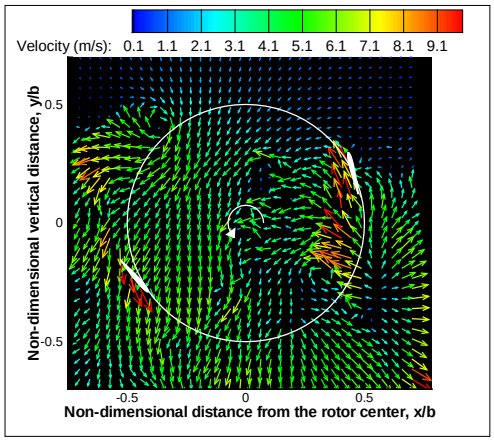

(c) 3-D CFD Results at $\Psi = 120°$

Figure 4.11: Mid-span velocity vectors inside the 2-bladed rotor cage at 1400 RPM, 40° pitch amplitude, $\Psi = 120°$.

aerodynamic power, a constant difference between the 2-D and 3-D CFD simulations and experiment is observed in the results. This suggests that although Benedict et al. did remove the tare from the support structures while calculating the aerodynamic power, there might be some additional tare which is not accounted for.

To assert this, the experimental and computational aerodynamic power obtained at zero degree collective pitch for a three-bladed rotor were compared. At

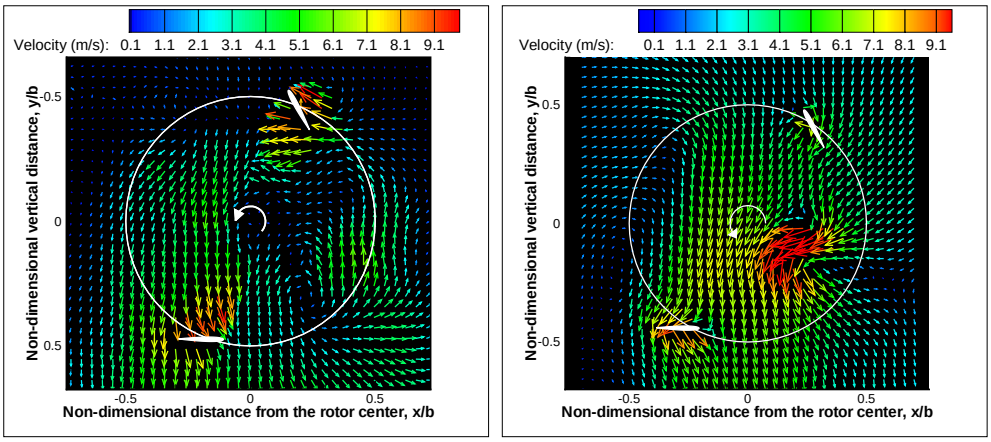

(a) DPIV Results at $\Psi = 150°$ (b) 2-D CFD Results at $\Psi = 150°$

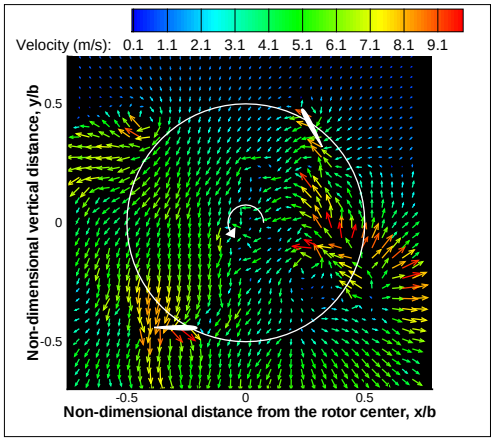

(c) 3-D CFD Results at $\Psi = 150°$

Figure 4.12: Mid-span velocity vectors inside the 2-bladed rotor cage at 1400 RPM, 40° pitch amplitude, $\Psi = 150°$.

1400 RPM, the experimental profile power obtained was 1.4 Watts, while CFD only predicted 0.2 Watts. The profile power obtained from the simulations correspond to an effective profile drag coefficient, C_{d_0}, of 0.029. The profile power obtained from experiment, however, corresponds to a C_{d_0} value of 0.2, which is unrealistic for any well-designed airfoil. This further confirms the assumption that there is a tare not accounted for in the experiments.

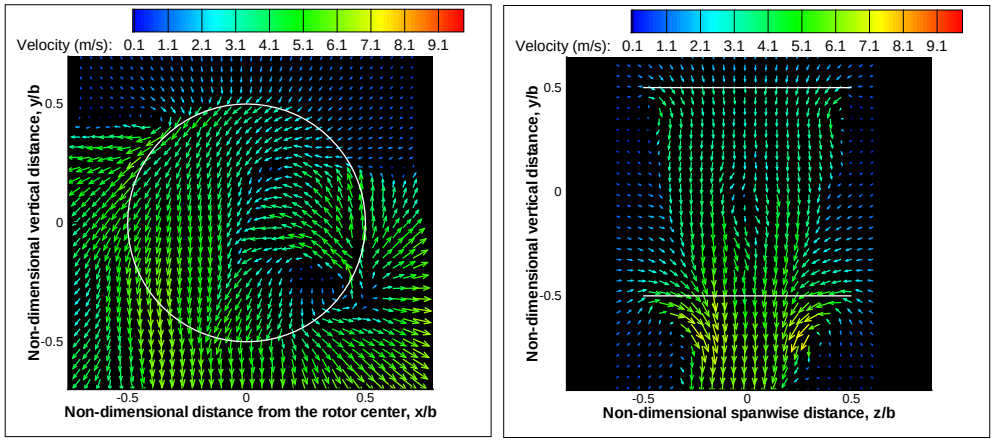

(a) X-Y plane at mid-span (b) Y-Z plane at x = 0

Figure 4.13: Time-averaged velocity vectors inside the 2-bladed rotor cage at 1400 RPM, 40° pitch amplitude

4.4.2 Velocity Vectors

With the available DPIV experimental data from Benedict et al. [14], the flowfield predicted by 3-D CFD using the fine mesh can be validated. The first subplot in each of the Figures from 4.9 - 4.12 show the velocity vectors obtained via DPIV by Benedict et al. for the mid-span flowfield at $\Psi = 0°$, $\Psi = 30°$, $\Psi = 120°$, and $\Psi = 150°$. The third set of subplots display the computational solutions of the 3-D CFD model with unsteady pitch approximated using the four-bar blade kinematics model discussed above. In these and the following flow-visualization plots, the "rotor center" corresponds to the $y - z$ plane at $x = 0$. It should be mentioned here that the mesh used to plot the computed velocity vectors does not correspond to the actual mesh used for the simulation. The solution from CFD mesh was interpolated onto a Cartesian mesh to provide a comparative view with the experimental data. Both the CFD and experimental result show inflow in the $-y$ direction through the left half of the

rotor cage with equivalent velocity magnitudes, although the DPIV results show this vertical trend explicitly for the left side (less than $x = 0$), whereas the 3-D results extend this region only to $x = -0.1$. A high level of unsteadiness is captured by CFD in the right half of the rotor cage due to the accumulation of shed vortices from the top blade near $\Psi = 90^\circ$, as confirmed later in the plots of iso-surfaces of q-criterion (method developed by Jeong and Hussain [49]), though this unsteadiness is larger than that observed through DPIV.

The DPIV data shows significant skewing of the wake in the $+x$ direction immediately downstream of the rotor cage; this phenomenon is also visualized in CFD. A reverse flow region in the upward direction at $\Psi = 90^\circ$ in the experimental velocity vector field is captured at all azimuthal angles in the 3-D CFD. From the inflow plots shown later, this region of upward flow is clearly visualized as a positive inflow peak at mid-span halfway up the rotor cage. Moreover, the vortical structure in the upper-left quadrant near $\Psi = 225^\circ$, most prominent in Fig. 4.11(a), is captured by CFD. Overall, the 3-D results are highly unsteady and capture general trends of the DPIV velocity vectors, but seem to overpredict the magnitude of these vectors.

The second set of subplots in Figures 4.9 through 4.12 visualize the same azimuthal angles with the 2-D flow solver. Although there are large-scale similarities between the 2-D and 3-D velocity vectors, the 2-D solver does not fully capture the unsteadiness present in the right half of the rotor cage. It also suffers from overprediction of the magnitude of velocity vectors as compared with DPIV. As apparent in all of the azimuthal angles, the 2-D solver captures fairly steady, linear top-to-bottom inflow within the entire rotor cage. Furthermore, especially evident at $\Psi = 0^\circ$ and $\Psi = 30^\circ$, there is a region of higher velocity

magnitudes near the bottom of the rotor cage at the $x = 0$ position. Both these phenomena are not present in the experimental results, and can be attributed to the inability of the 2-D solver to capture 3-D effects, further discussed below.

The 2-D solver can only capture shed vortices from the blade, while the 3-D solver can capture trailed vortices in addition to shed vortices. This may serve to explain the much larger unsteadiness in the 3-D results as compared with the 2-D. However, it seems that both the 2-D and 3-D models overpredict the unsteadiness in the left half of the rotor cage; this is particularly pronounced in the 3-D results for rotor cage angles from $\Psi = 225^\circ$ to $\Psi = 315^\circ$ for all instantaneous blade locations tested. The reason for this increased level of unsteadiness in the CFD results as of yet is unknown. Furthermore, in the 2-D results at the $x = 0.3$ location mid-plane through the rotor cage, there is an extremely strong shed vortex from the blade after it has passed the $\Psi = 90^\circ$ azimuth angle, as shown in Figures 4.11(b) and 4.12(b). Assuming the same amount of circulation around the airfoil for both the 2-D simulation and mid-span cut from the 3-D simulation, this would indicate that when the vortex is shed from the blade, it is shed entirely in the chordwise direction on the 2-D solver, but can propagate in both the chordwise and spanwise directions in the 3-D solver. This may serve to explain the much stronger shed vortex on the 2-D CFD simulation at this location as compared with the 3-D simulation, since some of the vortex strength is allowed to dissipate in the spanwise direction in the 3-D solver.

Figure 4.13 shows the flow time-averaged at all azimuthal locations for the 3-D CFD simulation; 4.13(a) is a cut in the $x - y$ plane at mid-span and 4.13(b) is a cut in the $y - z$ plane at the rotor center ($x = 0$). The time-averaged plots have largely dissipated the transient solution so that the general trend of

inflow through the rotor cage can be observed. In Figure 4.13(a), the fairly linear flow in the downward direction on the left half of the rotor cage, as well as the upward flow region at $\Psi = 90^\circ$ can clearly be observed. This mirrors to the instantaneous DPIV results well. Skewing of the wake below the rotor cage in the $+x$ direction is also obvious. The stationary vortical structure at $\Psi = 45^\circ$ has not dissipated, indicating that this is a permanent fixture in the flow. In Figure 4.13(b), the wake contraction can clearly be seen from the top to bottom blades, and below the bottom blade. The small region of upwash at the tips of the bottom blade will be better visualized later in the spanwise vorticity contours. Some unsteadiness is seen at the center of the wake from the top blade, corresponding to the region of accumulated shed vortices visualized in the iso-surfaces of q criterion plot, also shown later. Furthermore, the skewing of the wake on the bottom rotor towards the $-z$ direction will reappear while looking at vorticity contour in the next chapter.

4.5 Summary

This chapter described the specific methodology used to simulate the cyclocopter experiments of Benedict et al., as well as provided performance and flowfield comparisons of the CFD solver with experiment. From this chapter, it was shown that:

- The overset mesh system consisted of a body-fitted curvilinear C-O type blade mesh and a cylindrical background mesh. A "fine" 3-D overset mesh system was used for flowfield visualization and a "coarse" mesh was used for performance measurements in the simulation. The 2-D mesh corresponded

to the mid-span section of the "fine" 3-D mesh. Comparisons of the time histories of both meshes showed grid convergence.

- Blade deformations were prescribed using Benedict's computational structural dynamics code. In addition, the pitch linkage lengths specific to the cyclocopter for the numerical approximation to the four-bar equation were described in the current chapter.

- The thrust and aerodynamic power comparisons between CFD and experiment showed that the vertical forces were captured well, with sidewise force being underpredicted and power offset by a tare. To support the assumption that a tare power was unaccounted for in experiment, the profile power was compared for a rotor at zero pitch. From this, the profile drag coefficient obtained from the simulations was much more reasonable than that obtained from experiment for a well-designed symmetric airfoil.

- The velocity vector comparison between 3-D CFD and experiment shows good qualitative agreement. However, the 2-D code fails to capture a large amount of the unsteadiness present in the flow.

With reasonable correlation achieved, the following chapter explores CFD-specific results to provide additional insight into the flowfield.

Chapter 5

CFD Predictions

Chapter 4 compared the flow solver predictions to the performance results obtained from experiment. It was shown that vertical thrust was well-predicted, while sidewise thrust was less-well predicted and, though the trend was captured for aerodynamic power, the value of the prediction was offset by a tare factor. This overall asserts reasonable correlation with experiment. In addition, the qualitative comparisons of the flowfield with the PIV results showed that both the 2-D and 3-D models obtained fairly good results. Taking this into consideration, the following sections qualitatively explore characteristics of the flowfield in ways difficult or impossible to obtain from experiment. It also seeks to explain the discrepancies between CFD performance predictions and experiment through investigations of time-varying quantities within the flowfield. With the validations performed in the previous section, the following predicted solutions can be taken to exhibit reasonable physical accuracy.

5.1 Variation in Force and Power Over Time

The experimental setup described in Chapter 4 was only optimized to measure the time-integrated values of thrust and power, not their unsteady variations over time. Thus, the flow solver provides a powerful tool to understand azimuthal variations of these values.

Figure 5.1 shows the variation in vertical force (T_y), sidewise force (T_x), and

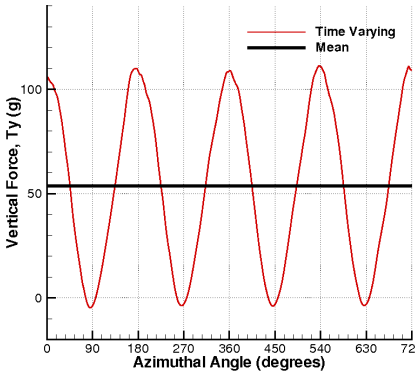

(a) Vertical force, T_y

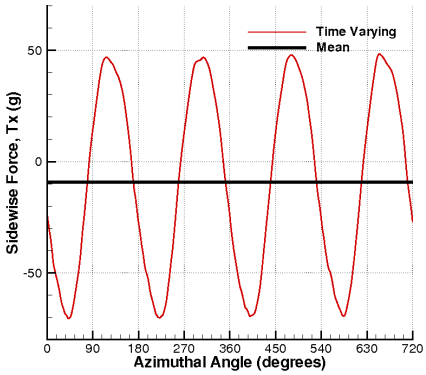

(b) Sidewise force, T_x

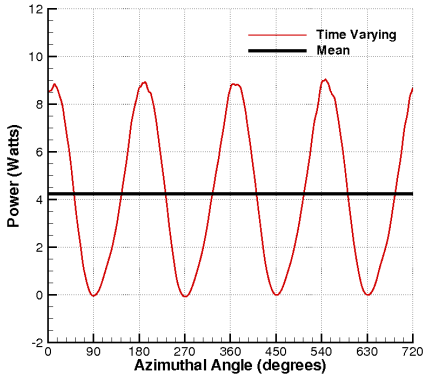

(c) Aerodynamic power

Figure 5.1: Variation in thrust and power over two revolutions at 1400 RPM and 40° pitch amplitude for Blade 1 and Blade 2 combined.

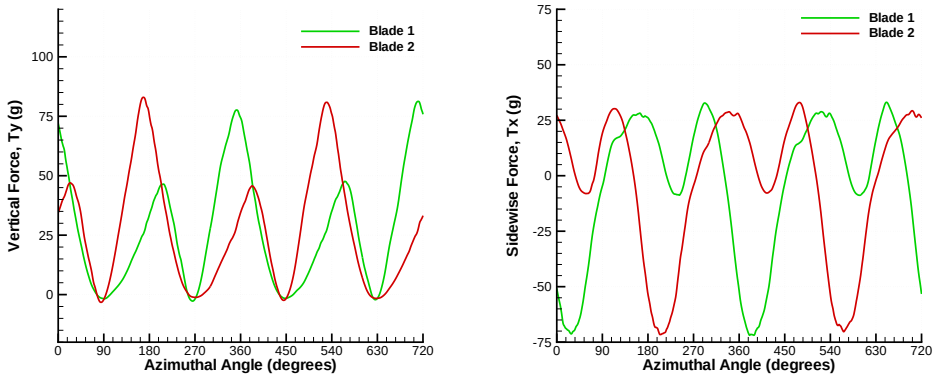

(a) Vertical force, T_y

(b) Sidewise force, T_x

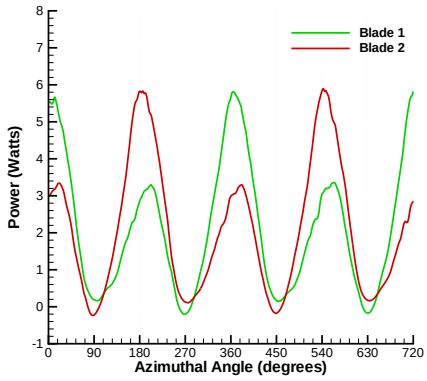

(c) Aerodynamic power

Figure 5.2: Variation in thrust and power over two revolutions at 1400 RPM and 40° pitch amplitude.

aerodynamic power for the entire rotor system at 1400 RPM and 40° pitching amplitude for two revolutions. These results were taken from the 3-D flow solver for a 2-bladed case. As seen in the figure, the variation over time of these quantities is highly unsteady, and occur periodically at 2/rev over the azimuth. The x-axis as defined in this plot corresponds to the azimuthal locations of Blade 1, which starts at the bottom of the cyclocopter cage. The variation of forces and

power in revolution two ($360° < \Psi < 720°$) is highly similar to revolution one, ($0° < \Psi < 360°$), thus reinforcing the assertion that periodicity was attained in the unsteady flow solution. The RMS values obtained for the time histories of T_x, T_y, and power are 21.56 grams, 34.34 grams, and 2.77 Watts respectively. All of the RMS values are significantly high (on the same order or higher than mean values), signifying a large amount of fluctuation from the mean value.

While CFD can be employed to observe the fluctuations in thrust and power over the entire rotor, the solution can also be decomposed into the timewise variations of these quantities over each blade, as seen in Figure 5.2. At zero azimuthal angle ($\Psi = 0°$) in the plot, Blade 1 is at the lowest y-axis position, while Blade 2 is opposite Blade 1 at the highest y-axis position. Periodicity is clearly evidenced via the trends in the solution from each blade: the force and power values for Blade 2 look almost identical to Blade 1 but phase shifted by 180°, and also from one revolution to another if only one blade is considered. The plot clearly shows large variation in all the integrated values; whereas the variation in thrusts over the entire rotor was relatively sinusoidal, the thrusts over each individual blade show highly different trends. Analysis of these trends, as undertaken in the following two sections, disclose details about blade performance at various azimuthal locations in the cyclocopter cage.

5.1.1 Vertical Force and Aerodynamic Power Variation over Time

From Figure 5.2(a), one can observe that the maximum vertical force and aerodynamic power is attained when the blade is at the *lowest* azimuthal position, i.e. when the blade is at the bottom of the cyclocopter cage. This is counter-

intuitive, as intuition states that the inflow produced by the top of the rotor cage would decrease the angle of attack of the bottom half of the cage, and therefore one would expect the largest values to be attained at the top. Further, if we consider that at the instant in time when the airfoils are opposite each other at $\Psi = 0^\circ$ and $\Psi = 180^\circ$ that the blades can be thought of as two actuator disks, momentum theory models of coaxial rotors [50] state that since the lower rotor operates in the slipstream of the upper rotor, for a given value of thrust its net induced velocity is higher and hence its net efficiency is lower. Though the lower rotor is seeing a greater inflow velocity over half its disk area due to the downwash from the top rotor, the complexity of the rotor flowfield and interaction between the vortices shed by the top rotor on the lower rotor blades cause an overall loss in efficiency on the lower disk. Thus, following this logic, one would expect that the lower blade of the cyclocopter produces less lift; however, this is contradicted by the time-varying results. As will be discussed later in Section 5.1.4, the trends observed from CFD are attributed to the virtual camber effect.

The timewise variation in aerodynamic power is similar to the vertical force time history. However, maximum aerodynamic power is achieved simultaneously by the upper and lower blades at the maximum positive and negative y-axis directions. This is different from T_y, where the maximum vertical force of the upper blade is phase-shifted about $+30^\circ$ relative to the lower blade.

5.1.2 Sidewise Force Variation over Time

The time history plot of sidewise force shows large unsteady variations due to the pitching motion of the cyclocopter. As shown in Figure 5.2(b), the peak amplitude of instantaneous sidewise force is *up to* 15 *times* the mean value ob-

tained for Figure 4.7. Therefore, this signifies that the mean value of sidewise force is extremely sensitive to changes in blade pitch or deformation. A small error in the blade pitch or deformation from experiment can directly result in small changes to the time history of the sidewise force. These small variations can, in turn, lead to significant changes in the mean sidewise force. Therefore, performance in the sidewise direction is very difficult to predict with CFD.

5.1.3 Comparison Between Deformed and Undeformed Blades

As discussed in Section 2.3.3, radial bending, tangential bending, and torsional blade deformations obtained from Benedict's structural dynamic code were prescribed into TURNS. A comparison of the force generated by the undeformed blades and blades with prescribed deformations for a 2-bladed cyclocopter operating at 1400 RPM, 40° pitch amplitude is given in Figure 5.3. As seen in the figure, over two revolutions there is very little difference between inclusion and negation of structural deflections in the numerical simulation. The deformed blades generally attain a higher vertical force peak and a lower $+y$ sidewise force peak, but these differences are to within 14% of the undeformed model for all quantities calculated. Hence, it is largely unnecessary to prescribe blade deformations for the cyclocopter for this configuration, since the blades are fairly rigid and the RPM is low. For more flexible blades at higher RPMs, however, the structural deformations cannot be as easily neglected.

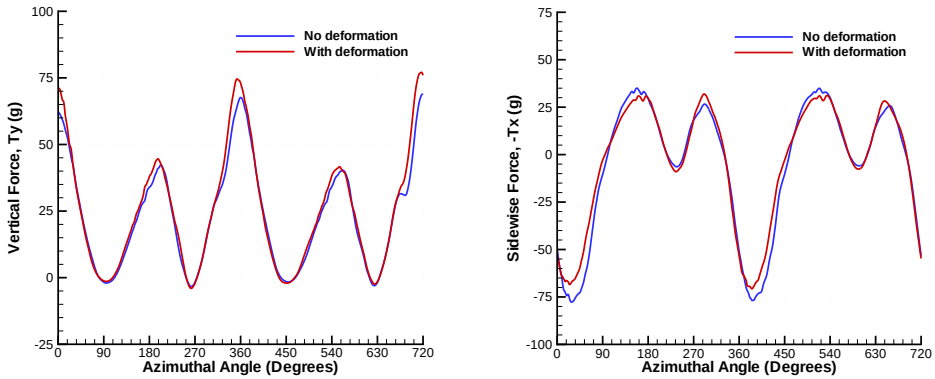

(a) Vertical force, T_y

(b) Sidewise force, T_x

Figure 5.3: Comparison between deformed and undeformed blades over two revolutions at 1400 RPM and 40° pitch amplitude for Blade 1.

5.1.4 Cambered Airfoil Analysis

As discussed in Section 5.1.1, the discrepancy in vertical thrust and power obtained in the unsteady time history at the "bottom" ($\Psi = 0°$) or "top" ($\Psi = 180°$) location on the rotor cage is due to the virtual camber effect. The virtual camber effect was first noticed by the vertical axis wind turbine community, but more recently for cyclocopter MAVs by Yun et al. [17] and Benedict et al. [16]. In the cycloidal rotor, since the blades travel on a circular path about the cage, and the ratio of chord length to radius of the circle is relatively large, the symmetric airfoil shown in 5.4(a) will not see the same angles of attack along the chord at zero pitch. At any instant, the leading edge will experience a negative angle of attack; the pitching axis (at quarter-chord for the cyclocopter) will have no angle of attack with respect to the freestream; and increasing chordwise positions from the pitching axis towards the trailing edge will experience increasingly positive angles of attack; this corresponds effectively to a cambered

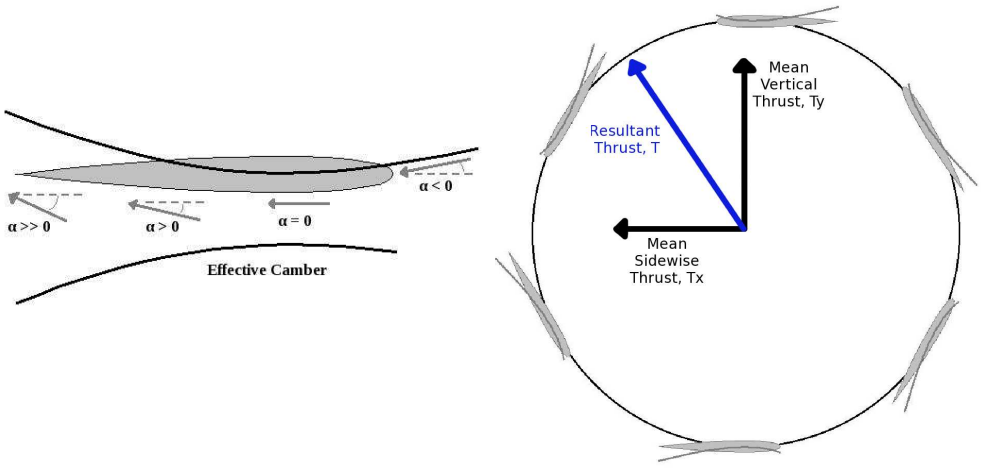

(a) Virtual camber effect on a symmetric airfoil

(b) Virtual camber effect over the cyclocopter cage

Figure 5.4: Illustration of the virtual camber effect on a cycloidal rotor at zero pitch.

blade geometry. From Figure 5.4(b), if we superimpose this effective camber onto the symmetric airfoil around the cyclocopter cage, then $\Psi = 0°$ is the point of maximum positive virtual camber, and $\Psi = 180°$ relates to maximum negative virtual camber. The virtual camber effect tries to negate the influence of inflow by increasing thrust at the bottom and decreasing thrust at the top, as will later be seen in the inflow flow visualizations. For a relatively small rotor radius-to-chord ratio as in the current situation, the effect of virtual camber is very significant. Therefore, the virtual camber effect overcomes the disadvantage posed by downwash from the upper blade on the lower blade, and as a result the lower blade actually produces *more* lift than the upper blade.

A cambered airfoil which can counteract the effect of virtual camber was tested to possibly improve the performance of the cycloidal rotor. From intuition, one can deduce that an airfoil with its camber line lying along the curvature

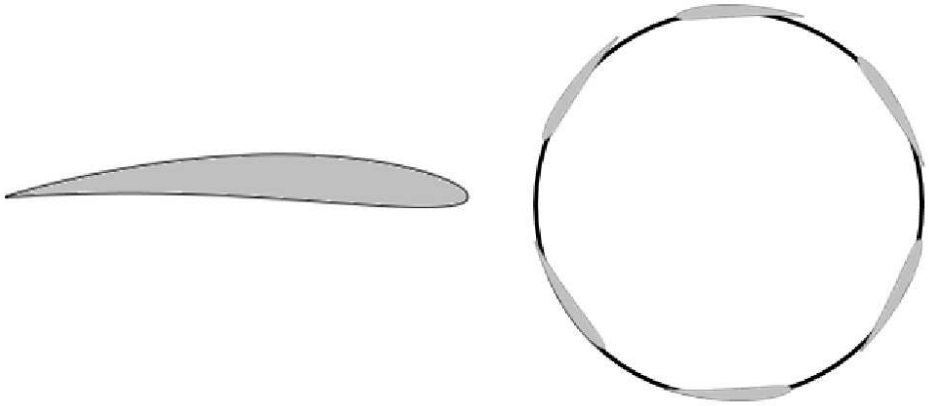

(a) NACA 0010 profile superimposed on 4.5% camber line.

(b) Cambered airfoil placement inside the rotor cage

Figure 5.5: Cambered airfoil design to negate the virtual camber effect.

of the cage should have no virtual camber effect at zero pitch. Such an airfoil may not be able to completely negate the virtual camber effect when the blade is at non-zero pitch, but it still can counteract most of its effect. Using this logic, with regard to dimensions of the current experimental setup, the cambered airfoil that needs to be used should have 4.5% camber. To obtain a comparative performance with the symmetric NACA 0010 run, an airfoil geometry is constructed by superimposing the thickness of the NACA 0010 profile onto the 4.5% circular arc camber line. Then, it is placed in the cyclocopter cage with camber pointed inward towards the center; a schematic of the airfoil and its placement inside the rotor cage is shown in Figure 5.5. Performance calculation for this cambered airfoil is done for 40° pitch amplitude 2-bladed case operating at 1400 RPM.

Figure 5.6 shows the comparison between one blade of the cambered airfoil geometry and the symmetric NACA 0010 airfoil for vertical force, sidewise force, and power. The time history of the vertical force clearly shows that use of the

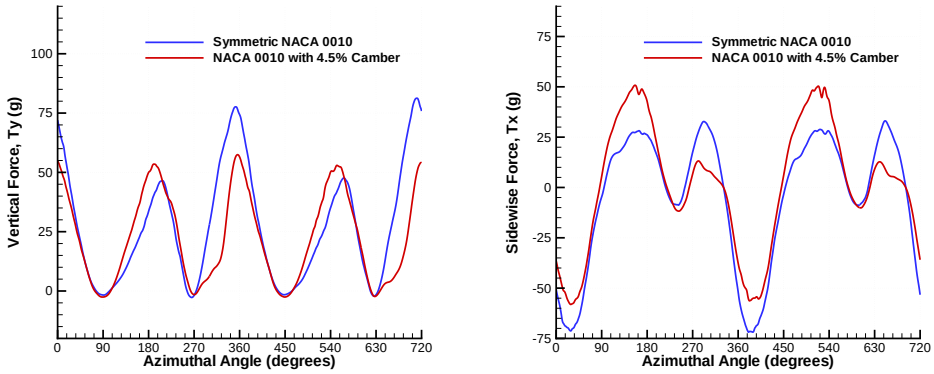

(a) Vertical force, T_y

(b) Sidewise force, T_x

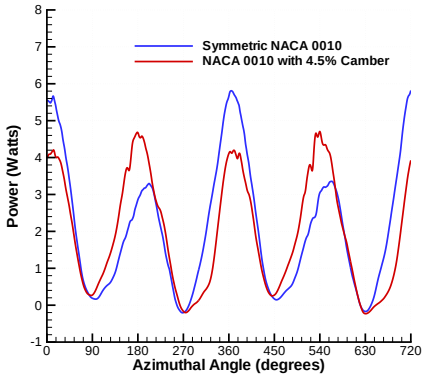

(c) Aerodynamic power

Figure 5.6: Variation in thrust and power on Blade 1 over two revolutions at 1400 RPM and 40° pitch amplitude for the cambered vs. uncambered airfoil.

cambered airfoil has counteracted the effect of virtual camber, as observed with the NACA 0010 airfoil. For the cambered airfoil, the maximum vertical force achieved at the top of the cyclocopter cage is almost identical in magnitude to the bottom of the cyclocopter cage; similar trends are observed for power. However, the peaks in sidewise force are more dissimilar for the cambered as compared to the symmetric airfoil. As a result of this, the integrated sidewise force for the cambered airfoil is smaller compared to that for symmetric airfoil

(−2.58 grams compared to −9.12 grams).

Considering the integrated values of the vertical force and power for the cycloidal rotor using a cambered airfoil, it is seen that although the these values become relatively similar at the top and bottom of the rotor cage, the combined maximum thrust achieved with the cambered configuration is not as high as the symmetric. The mean T_y and power for the cambered airfoil are 44.69 grams and 3.93 Watts; the analogous values for the symmetric airfoil are 53.75 grams and 4.23 Watts, respectively. For the purpose of performance comparison, the power required by the symmetric airfoil is calculated at the thrust produced by the cambered airfoil by interpolating data from Figs. 4.8(a) and (c). Interpolated power for the symmetric airfoil was found to be 3.6 Watts, which is slightly lower than the power for cambered airfoil. Therefore, camber seems to have a slight detrimental effect on the performance. However, a clear conclusion cannot be made on the effect of camber by merely a single performance result. Cambered blades might offer beneficial results at higher pitch angle, as the blades now will have reduced stall due to the reduction in lift peak. Further investigations must be undertaken to ascertain the full effect of using the cambered airfoils.

5.2 Spanwise Thrust Distribution

To gain insight into the three-dimensionality of the flowfield, the spanwise distribution of vertical and sidewise thrust was examined as a function of azimuthal angle. The 3-D CFD simulation results at $1400RPM$ and 40° pitch amplitude with the fine mesh are shown in Figures 5.7 and 5.8. In these plots, the z-axis has been non-dimensionalized with respect to the rotor span, b; this convention applies to all the axes in the ensuing flowfield visualization plots. Also, at any

instant in the revolution, the azimuthal angle of the top blade is always 180° out of phase with respect to the bottom blade.

The spanwise distribution of vertical and sidewise thrust show significant changes over the span at most azimuthal locations. Three main phenomena which cause variation of these quantities along the span are described below:

- The tip vortex generated near the ends of the blade cause a local peaking of the thrusts before it drops down to zero at the tip.
- Unsteady shedding causes fluctuations to the distribution near the mid-span sections of the blade, most apparent for Blade 1 at the 30° and 60° azimuth locations in part (b) and (c) of the spanwise distribution plots.
- Different inflow velocities due to wake contraction from one blade cause the mid-portion of the other blade to produce significantly higher or lower thrust compared to its outer portion. This variation is seen at almost all the wake-ages on both the force distributions, but most prominently in the sidewise force distribution when the blade is at the right most part of the cage, $\Psi_{B1} = 90°$. In this plot, there is a clear demarcation between the higher thrust region at $-0.25 < z/b < 0.25$, and lower thrust outer regions $-0.5 < z/b < -0.25$ and $0.25 < z/b < 0.5$.

For further exploration into the third phenomenon described above, the instantaneous inflow normalized by rotational speed has been plotted for the quarter-chord line along the span, as shown in Figure 5.9. From the plot, it can be seen that at all azimuth locations other than the locations from 60° to 120° azimuth, there is a downwash across the span of the rotor. At 60° to 120° azimuth locations, the inflow acts in the upward direction. Note that, this upward

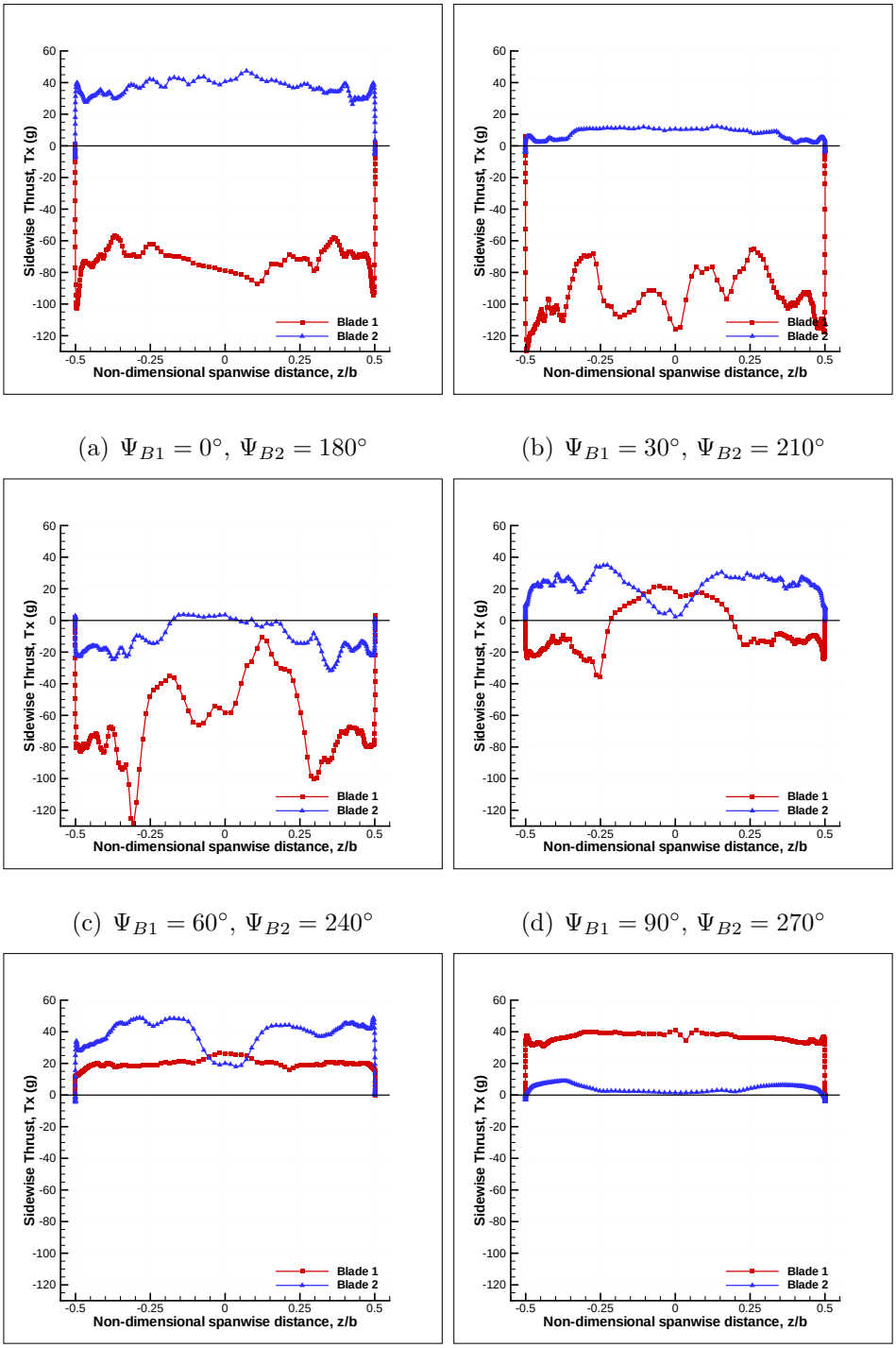

(a) $\Psi_{B1} = 0°$, $\Psi_{B2} = 180°$

(b) $\Psi_{B1} = 30°$, $\Psi_{B2} = 210°$

(c) $\Psi_{B1} = 60°$, $\Psi_{B2} = 240°$

(d) $\Psi_{B1} = 90°$, $\Psi_{B2} = 270°$

(e) $\Psi_{B1} = 120°$, $\Psi_{B2} = 300°$

(f) $\Psi_{B1} = 150°$, $\Psi_{B2} = 330°$

Figure 5.7: Sidewise force, T_x along the span for 1400 RPM, 40° pitch amplitude.

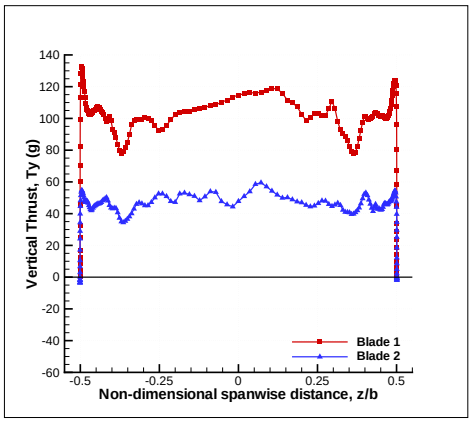

(a) $\Psi_{B1} = 0°$, $\Psi_{B2} = 180°$

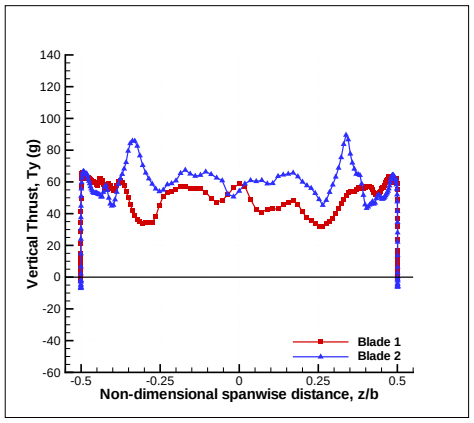

(b) $\Psi_{B1} = 30°$, $\Psi_{B2} = 210°$

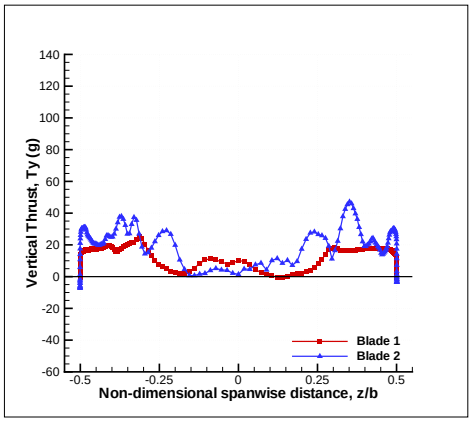

(c) $\Psi_{B1} = 60°$, $\Psi_{B2} = 240°$

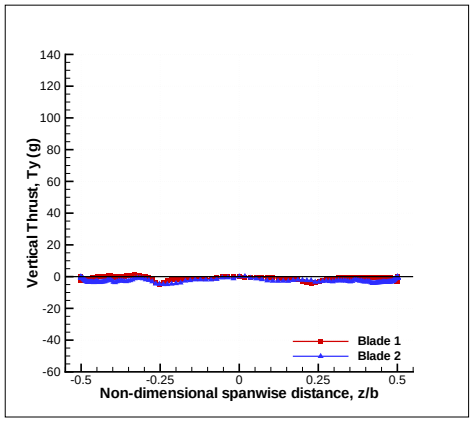

(d) $\Psi_{B1} = 90°$, $\Psi_{B2} = 270°$

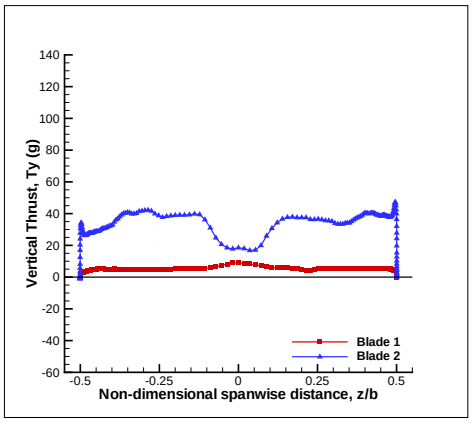

(e) $\Psi_{B1} = 120°$, $\Psi_{B2} = 300°$

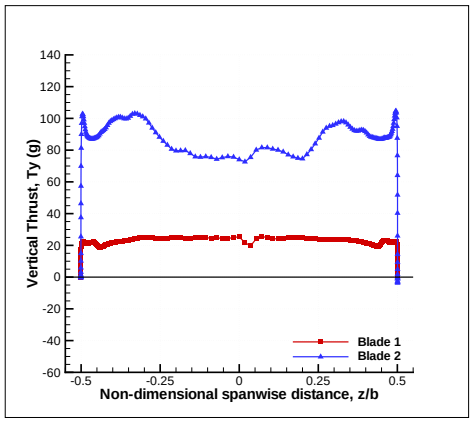

(f) $\Psi_{B1} = 150°$, $\Psi_{B2} = 360°$

Figure 5.8: Vertical force, T_y along the span for 1400 RPM, 40° pitch amplitude.

flow region was observed in both CFD and experimental velocity vector plots shown earlier. The important feature to notice from these plots is that the inflow at all azimuth locations has higher absolute value around the mid-sections of the blade, and almost linearly drops down to zero towards the tip. The extent of this high inflow mid-section region varies with azimuthal location and is determined by the amount of wake contraction at that location. When observed carefully, it can be noticed that the spanwise thrust distribution plots clearly correlate well with the inflow plots at most of the azimuth locations. As expected, the inflow velocities acting downward (negative value) are seen to decrease the thrust and the velocities acting upwards (positive value) increase the thrust.

Overall, from the plots presented in this section, it is observed that there is significant variation in the spanwise thrust distribution, attesting to the high level of three-dimensionality in the flowfield. Thus, although good performance predictions were obtained using 2D CFD calculations, a 3D calculation is essential to understand the details of the flow physics.

5.3 Time-Averaged Inflow Distribution

Inflow distribution, as was shown in the previous section, is largely related to the spanwise thrust, and thus can provide a good precept to characterize the thrust distribution over the blade at a given azimuthal position. Furthermore, inflow can also prove a useful tool to visualize the flow velocities over the entire rotor system.

Figure 5.10 shows surface plots of inflow normalized by rotational speed taken at different cuts in the $x - z$ plane along the y-axis. At $y = +0.8R$, the inflow ratio is fairly small across the rotor, with the largest inflow being observed at

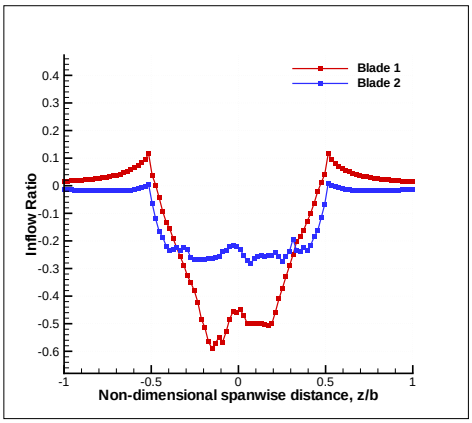

(a) $\Psi_{B1} = 0°$, $\Psi_{B2} = 180°$

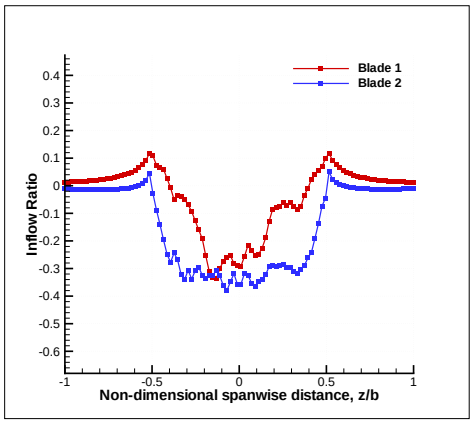

(b) $\Psi_{B1} = 30°$, $\Psi_{B2} = 210°$

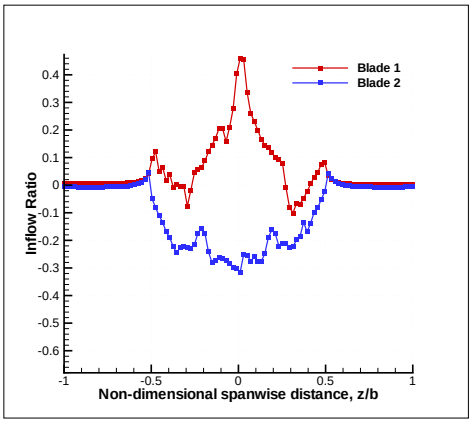

(c) $\Psi_{B1} = 60°$, $\Psi_{B2} = 240°$

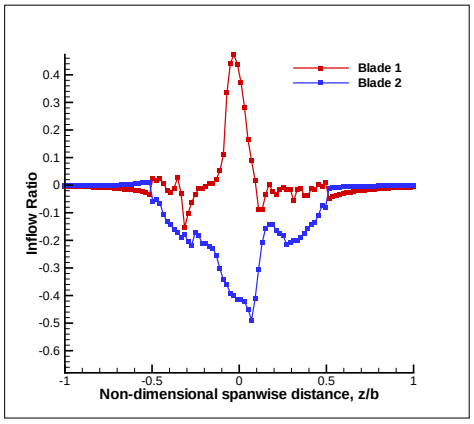

(d) $\Psi_{B1} = 90°$, $\Psi_{B2} = 270°$

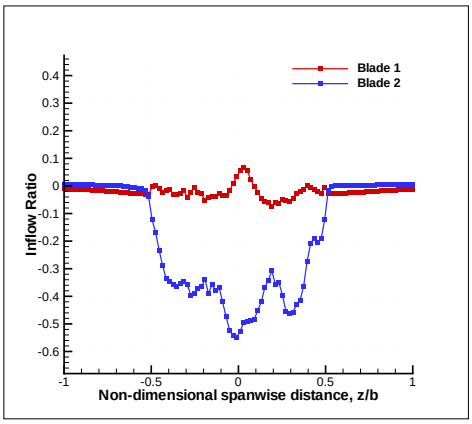

(e) $\Psi_{B1} = 120°$, $\Psi_{B2} = 300°$

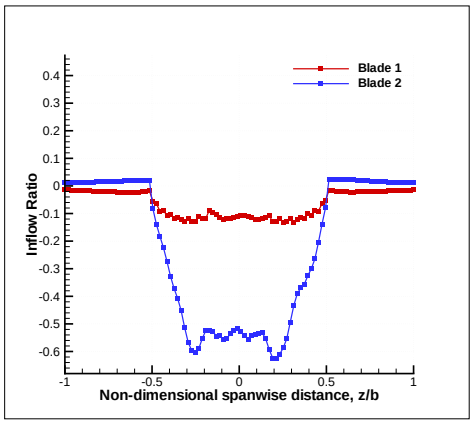

(f) $\Psi_{B1} = 150°$, $\Psi_{B2} = 330°$

Figure 5.9: Inflow vs. spanwise location at the quarter-chord position of each blade for 1400 RPM, 40° pitch amplitude.

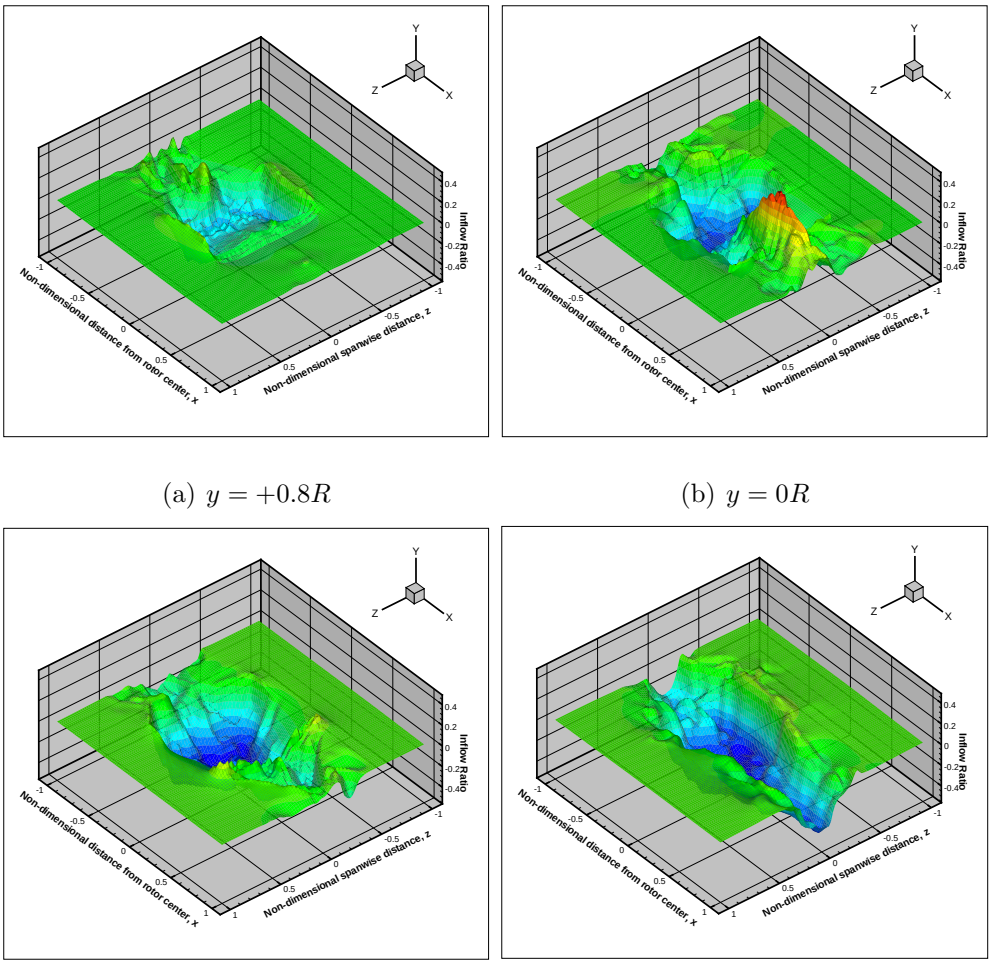

(a) $y = +0.8R$ (b) $y = 0R$

(c) $y = -0.8R$ (d) $y = -2R$

Figure 5.10: Surface plots of time-averaged inflow in $x - z$ plane at 1400 RPM, 40° pitch amplitude.

the center of the rotor cage and some unsteadiness noticed in the negative x direction. With successively lower $x - z$ planes through the cage, however, the maximum inflow ratio is still observed at the rotor center, but with larger peak negative inflow values. At $y = 0R$, the region of reversed flow near $\Psi = 90°$ as observed in the DPIV results is now clearly seen as a peak in the inflow ratio in the right half of the rotor, at center span. At $y = -0.8R$, the unsteadiness observed in $-x$ has now traveled to the $+x$ half of the rotor cage. By $y = -2R$,

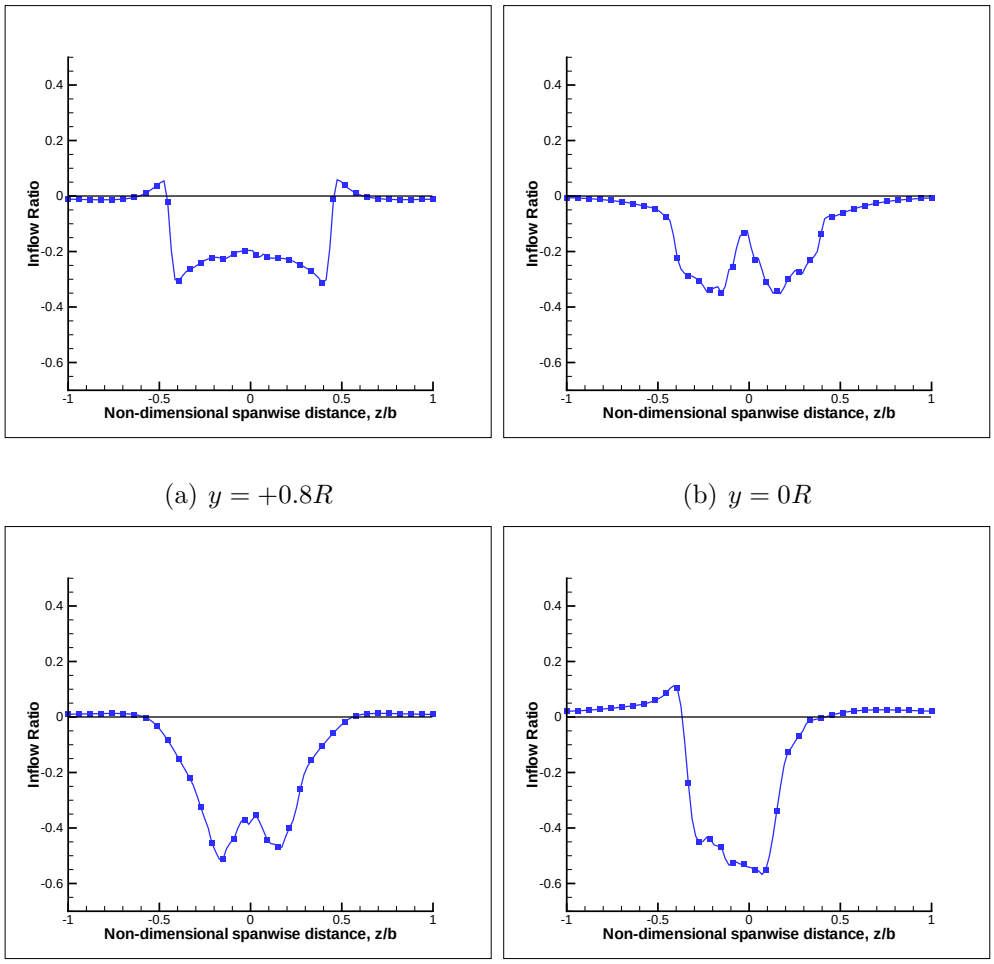

(a) $y = +0.8R$ (b) $y = 0R$

(c) $y = -0.8R$ (d) $y = -2R$

Figure 5.11: Inflow vs. spanwise location at the rotor center for 1400 RPM, 40° pitch amplitude

most of the unsteadiness of the rotor cage has dissipated in the wake, but the skewness of the wake from the rotor cage towards the $+x$ direction, as observed in the lower-right quadrant of the PIV measurements in Figure 4.9, is noticed here by the large negative inflow ratio in the $+x$ half of the surface plot.

Though the surface plots provide a good qualitative overview of the time-averaged inflow on the rotor system, it does not allow for quantitative analysis. A better quantification of the inflow as well as visualization of wake contraction is

attained by plotting the spanwise distribution at the rotor center at various y-axis heights. The wake contraction is clearly observable in Figure 5.11 at $y = +0.8R$, corresponding to the top of the rotor cage, the inflow is fairly constant and distributed quite evenly across the span. However, as one progresses down the y-axis, the inflow region decreases in spanwise length due to the wake contraction and, as consistent with the conservation of momentum, the negative inflow ratio peak increases due to the larger downward component of vertical velocity.

5.4 Flow Visualization

A better understanding of the three-dimensionality of the flowfield can be obtained by looking at the iso-surfaces of q-criterion. The following results were obtained from a fine mesh for a 2-bladed cyclocopter configuration at 40° pitch and 1400 RPM with NACA 0010 blades. Figure 5.12 shows the iso-surfaces of q-criterion colored by x-vorticity contour for $q = 4$. In this plot and henceforth, wake age will be analogous to the Ψ location of "Blade 1". From the figure, a highly complex flowfield is observed, and there is extreme unsteadiness within the cyclocopter cage. For the bottom blade at $\Psi_{B1} = 0°$ wake age, there is a roll-up of strong vortices at the blade tips which follow the circumference of the rotor cage, as well as a fair amount of unsteady shedding along the span. These tip vortices detach from the blade at around $\Psi_{B1} = 150°$ wake age and acquire a significant amount of twist before being shed into the wake. The tip vortices formed by the top blade at $\Psi_{B2} = 180°$ wake age are relatively weaker, as the thrust there was smaller (as shown in Fig. 5.2), and detach at $\Psi_{B2} = 270°$, about four chord lengths away from the trailing edge of the upper blade. These shed vortices may contribute to the large amount of unsteadiness in the rotor

center as they convect down between the $\Psi_{B2} = 300^\circ$ and $\Psi_{B2} = 360^\circ$ wake ages; indeed, it can be seen in the iso-surface of q-criterion plots that the vortical structures at the center are created as a result of the shedding from upper blade tip vortices during previous revolutions. The tip vortices formed by the bottom blade are directly shed into the rotor wake and do not interact with the rotor center.

The contours of x-vorticity from the $y - z$ plane taken from the rotor center are shown in Figure 5.13(a); one can clearly observe the roll-up of the tip vortices from the top blade and their convection downwards through the rotor cage. The wake contraction in the downwash of the top blade shows that its *vena contracta* extends for roughly half its geometrical length, and hence half the area of the lower blade is operating effectively in an axial climb condition induced by the top blade. There is more unsteady shedding and stronger tip vortices produced by the lower blade due to higher thrust, and its wake contraction is generally observed to be less pronounced than the top blade, with skewing towards the $-z$ direction possibly due to the asymmetry of the blade deformation. The high level of unsteadiness captured by the iso-surfaces of q-criterion plot is also seen here at the center of the rotor cage convecting downwards. Overall, the cyclocopter presents an extremely complex and unsteady flow environment.

5.5 Summary

This chapter explored CFD predictions of cyclocopter unsteady performance and flow three-dimensionality. Some specific observations follow:

- The unsteady forces and power were seen to be highly periodic, with large

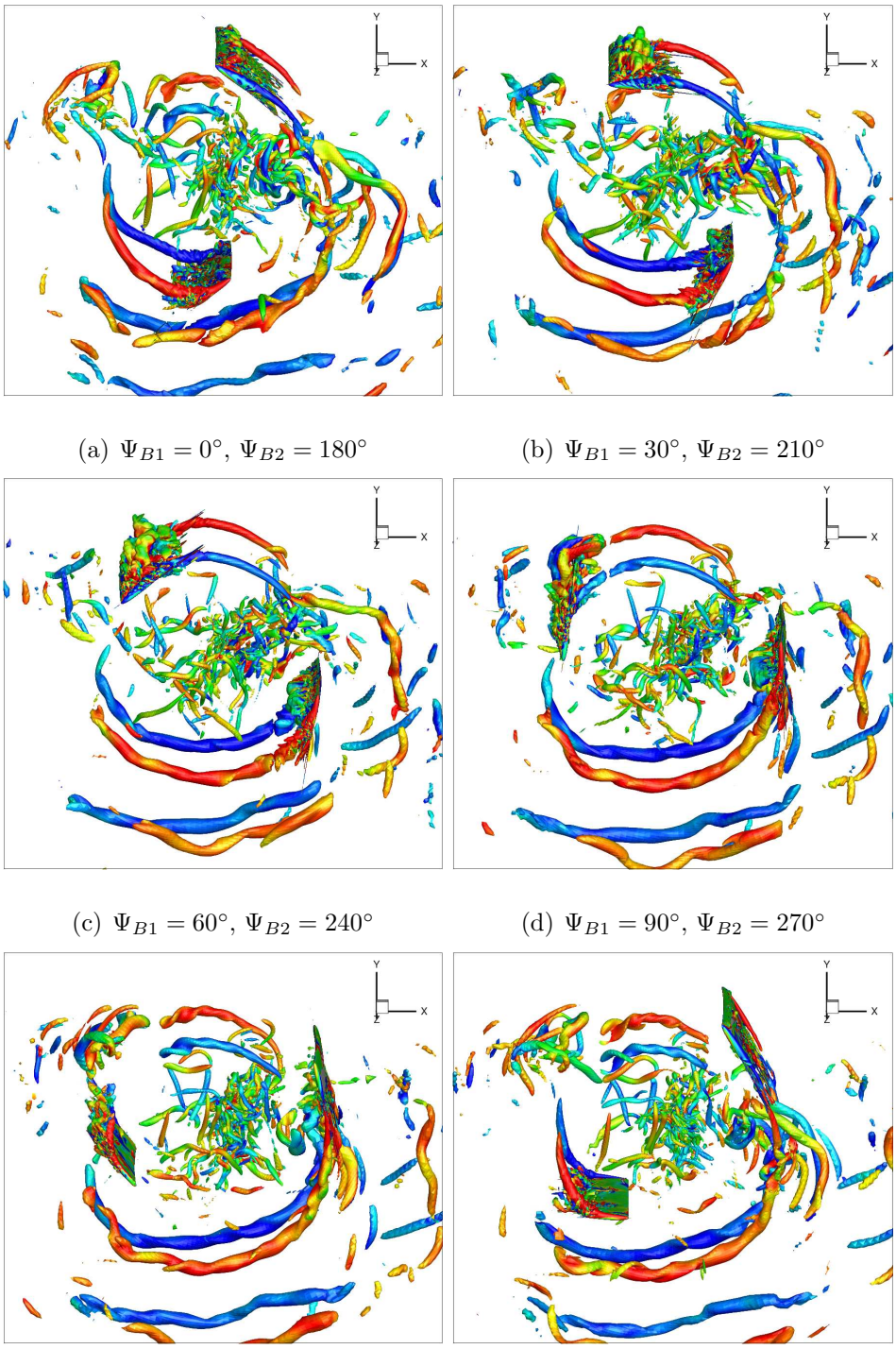

(a) $\Psi_{B1} = 0°$, $\Psi_{B2} = 180°$

(b) $\Psi_{B1} = 30°$, $\Psi_{B2} = 210°$

(c) $\Psi_{B1} = 60°$, $\Psi_{B2} = 240°$

(d) $\Psi_{B1} = 90°$, $\Psi_{B2} = 270°$

(e) $\Psi_{B1} = 120°$, $\Psi_{B2} = 300°$

(f) $\Psi_{B1} = 150°$, $\Psi_{B2} = 330°$

Figure 5.12: Iso-surfaces of azimuthal vorticity contour for q-criterion, $q = 4$ at 1400 RPM, 40° pitch amplitude.

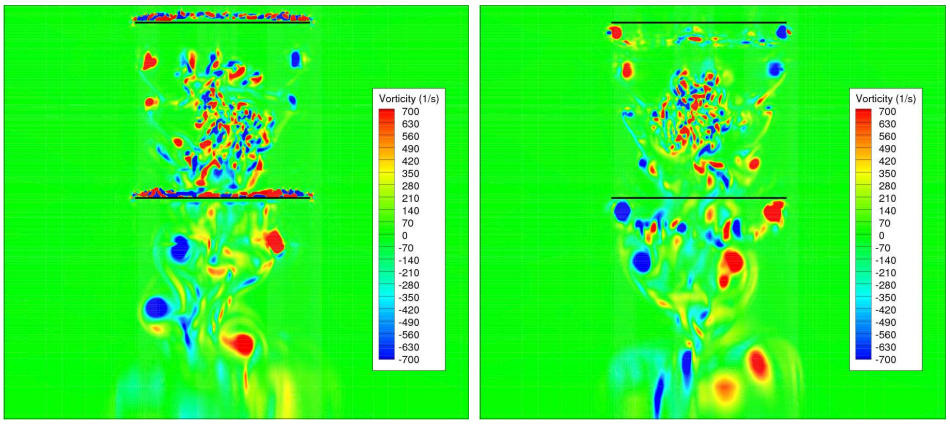

(a) $\Psi_{B1} = 0°$, $\Psi_{B2} = 180°$ (b) $\Psi_{B1} = 30°$, $\Psi_{B2} = 210°$

(c) $\Psi_{B1} = 60°$, $\Psi_{B2} = 240°$ (d) $\Psi_{B1} = 90°$, $\Psi_{B2} = 270°$

(e) $\Psi_{B1} = 120°$, $\Psi_{B2} = 300°$ (f) $\Psi_{B1} = 150°$, $\Psi_{B2} = 330°$

Figure 5.13: Contours of spanwise vorticity at 1400 RPM, 40° pitch amplitude.

RMS values signifying a large amount of fluctuation from the mean value.

- Variations of vertical force and aerodynamic power over each blade show that the virtual camber effect plays a large role in the performance of the cyclocopter, and causes a degradation in performance for the blade at the "top" of the cyclocopter cage, in comparison to the "bottom" blade. The sidewise force variation indicated that its mean value was highly sensitive to changes in blade pitch or deformation. Since small deviations in pitch or deformation predictions can result in changes to the time history, thus leading to large changes in the mean value. Therefore, performance in the sidewise direction is very difficult to predict with CFD.

- Since the blades were fairly rigid and the RPM used in the experiments was relatively low, the solution obtained from prescribing blade deformations matched closely to the solution with no deformations. Thus, for this case, it is largely unnecessary to include blade deflections.

- The cambered airfoil analysis showed that for the case tested, cambered airfoils tended to negate the virtual camber effect but caused an overall degradation in performance. However, additional work needs to be done to ascertain the full benefit or detriment of using cambered blades.

- The spanwise thrust distribution was highly three-dimensional, and is resultant from three different flow phenomena: the tip vortex, unsteady shedding from the mid-span, and inflow velocities due to wake contraction. As expected, it was found that inflow velocities acting downward decrease the thrust, and velocities acting upward increase the thrust.

- The time-averaged inflow surface plots showed a large inflow through the

center of the rotor cage, with a region of reversed flow (upward) near $\Psi = 90°$. The iso-surfaces of q-criterion plots exhibited the extreme amount of unsteadiness within the cyclocopter cage and the highly complex flow structure; the contours of spanwise vorticity captured the wake contraction.

From the above results, it is seen that with CFD, significant insight into the flow physics can be obtained in ways difficult to replicate in the laboratory.

Chapter 6

Conclusions

Within the last decade, interest in Rotary Wing Micro Air Vehicles (MAVs) has grown due to their extreme versatility for a number of different mission scenarios. However, the poor performance of conventional rotor designs at low Reynolds numbers have allowed a flood of new, unconventional rotor designs to be tested for MAVs. The rotor configuration described in this work was the cycloidal rotor, essentially a "horizontal axis rotary wing" wherein the blades pitch and revolve parallel to the rotational axis.

Previous experimental studies on the cycloidal rotor had mostly been undertaken in the early 20th century, but problems with characterizing the complex aerodynamics coupled with control issues due to the large centrifugal force from rotor revolution forced the abandonment of the idea before it could be implemented on aircraft. Recent studies of the cycloidal rotor have been focused on the MAV-scale, since this rotor configuration allows for instantaneous thrust vectoring plus extreme maneuverability. However, thus far only simple analytical models and preliminary, low-resolution CFD simulations have been used to characterize the performance of the cycloidal rotor.

This current work sought to form a computational methodology by which

the performance of the cyclocopter could be predicted to reasonable accuracy. Also, it focused on conducting unprecedented flowfield visualizations for the cyclocopter to understand the complex aerodynamics in ways unachievable by experiment. The following sections provide a brief summary of the contributions made in this work, list specific observations obtained from the CFD analysis, and suggest future research to further understanding of this unique rotor configuration.

6.1 Summary

The objective of this work was to develop a high-fidelity, high-resolution computational methodology to study the performance of the cyclocopter as well as provide unprecedented insight into the flowfield. To accomplish this, an existing compressible Reynolds-Average Navier-Stokes (RANS) Solver, OVERTURNS, was modified to simulate the flight regime and blade motion of the cyclocopter.

The solver was first tested against a series of simple problems for verification and validation before being applied to the cycloidal rotor. From the test cases, the solver showed that it was adept at predicting the performance for both a symmetric airfoil in steady, freestream conditions, and an unsteady, pitching airfoil undergoing dynamic stall at high angles of attack. Dynamic stall flow features were well captured as compared to 2-D VAWT experimental PIV measurements. With confidence gained in the accuracy of the solver, the cycloidal rotor could be simulated.

The cyclocopter experiments of Benedict et al. were chosen as a validation case for numerical simulations of the cycloidal rotor. The hovering cyclocopter rotor simulations were performed on structured body-fitted C-O blade mesh

overset onto a structured cylindrical background mesh. To compare performance, both an RPM sweep with a fixed blade pitch amplitude and a collective pitch sweep with a fixed RPM were tested. In addition to quantitative performance comparisons to experimental results, a qualitative comparison was also made between the PIV flow visualization and CFD results. In addition, cambered blades were tested to negate the virtual camber effect, and preliminary results were obtained for this design decision.

With validation of the flow solver accomplished, the flow physics were studied with CFD predictions to characterize unsteady phenomena and understand the three-dimensionality of the flowfield. The spanwise distribution of thrust was investigated as a function of azimuthal angle, and the relationship between inflow and spanwise distribution was closely examined. Furthermore, the extreme unsteadiness of the flowfield was visualized with the iso-surfaces of q-criterion and vorticity contours, after which observations were made.

6.2 Specific Observations

Detailed conclusions drawn from the CFD analysis on the cycloidal rotor are enumerated below.

1. Both the 2-D and 3-D solver were generally adept at obtaining vertical forces comparable to experiment, while not capturing the sidewise force well and underpredicting the power by a tare factor.

2. The total variation of thrust and power over time is easily obtained from CFD but extremely difficult to achieve with experiments. The time histories of all the integrated values were periodic with large variations. Com-

paring one blade at different revolutions, or both blades shifted 180° relative to each other, the histories look very similar.

3. The sidewise force time history is particularly sensitive to changes in pitch or deformation because the RMS value is much greater than the mean value. Therefore an accurate mean value comparable to experiment is difficult to predict with CFD.

4. The maximum vertical force and aerodynamic power for the cycloidal rotor design is attained when the blade is at $\Psi = 0°$, the lowest azimuthal position. This is due to the virtual camber effect from blade rotation which effectively imposes a positive camber on the symmetric airfoil at the bottom of the cyclocopter cage, and a negative camber at the top. However, testing of a 4.5% camber geometric configuration to counteract virtual camber was not as effective as assumed: although the mean sidewise force had reduced greatly, moderate decreases were observed for the thrusts and powers produced.

5. The velocity vector plots between 3-D CFD and experimental DPIV show a high level of accuracy in flow visualization for the CFD model. Almost all of the flow structures captured in the time-averaged vector plots were confirmed with other flowfield visualization methods.

6. The sidewise and vertical forces produced over the span show that the spanwise forces are highly three-dimensional, and cannot be captured by 2-D CFD. Three main types of spanwise variation are observed: the effect of tip vortex near the ends of the blade which cause local peaking of the thrusts before dropping to zero at the tip; fluctuations due to unsteady

shedding from the blade at certain azimuthal locations; and different inflow velocities seen by the mid and outboard spanwise sections due to wake contraction.

7. The surface plots of time-averaged inflow as well as slices in the z-direction corresponding to y-axis heights of various azimuthal locations clearly show the skewing of the inflow as well as wake contraction through the rotor cage, both phenomena observed through velocity vectors and vorticity contours. A region of upwash was observed that was consistent with experiment.

8. The iso-surfaces of q-criterion from the 3-D results show a massive amount of unsteadiness within the cyclocopter cage and larger tip vortices generated for the bottom blade than the top blade. The vorticity contours clearly show the wake contraction from the top and bottom rotors as well as skewing in the $-z$ direction past the lower blade, previously observed in the time-averaged spanwise velocity vectors. The strength of the tip vortex shed by the bottom blade is larger due to the higher thrust produced at this azimuthal location.

6.3 Future Work

Though the current CFD solver reasonably predicted performance and characterized the flowfield for the cycloidal rotor, there still remains a significant amount of work to be undertaken for gaining further insight into the cycloidal rotor.

- The discrepancies in power and sidewise force remain to be resolved. These discrepancies between CFD and experiment could possibly be reduced through modeling of the support structures.

- A major potential for research is a two-way coupled CFD-CSD model of the cyclocopter. The current study only initially prescribes grid deformations onto the blade mesh based on the steady blade periodic response obtained from the structural dynamics code. In essence, the simulation uses pre-deformed blades; a separate structural dynamics model is not being used to consider the deformations caused by the aerodynamic forces during the simulation. Hence, the power required to deform the blades is not accounted for in the numerical analysis. This may account for the power discrepancy between CFD and experiment.

- Newer designs can be easily tested with CFD that would otherwise be difficult with experiment. Such new designs may include looking at asymmetric pitch variation, camber, pitch axis location etc. to improve performance capability.

- Though the effect of cambered airfoils was studied, only preliminary results stemming from one test case were obtained. An RPM and collective sweep, followed by investigation into the flow physics, is truly required to ascertain if there is any benefit to be obtained from this blade design.

- The aerodynamics of the cyclocopter were only studied for hover in this work. Studies of this rotor in forward flight or maneuvers have yet to be conducted.

- An extension to the current work is the application of the cycloidal rotor to extract power in a "cycloidal wind turbine" configuration. By forcing the cycloidal rotor to act as if it were effectively in axial descent, the drag power that can be obtained from the wind may be greater than a conventional

vertical axis wind turbine. However, preliminary tests by the author of this work showed a significant dearth in the performance capability of the flow solver to characterize cycloidal wind turbine performance trends, especially at high tip speed ratios. Large-scale modifications to the code, possibly with the implementation of a transition model, need to be undertaken to correctly capture the flow physics of the cycloidal wind turbine. This remains an area with significant potential for investigation.

Furthermore, future experiments can be conducted to additionally validate the accuracy of the CFD prediction. Of these, paramount importance should be given to a validation for the unsteady fluctuations of vertical and sidewise force and power over time. Since only the integrated values of force and power were compared between CFD and experiment, it is not known how well the CFD solver performs at specific instances of the cyclocopter rotation. This validation would be particularly important for the sidewise force which, as was discussed earlier, had a mean predicted value which was particularly sensitive to changes in blade pitch or deformation. Therefore, while discrepancies between CFD and experiment may have been small for instantaneous values, these discrepancies could build up over one rotor revolution to cause a large difference between the mean value between CFD and experiment. An unsteady force and power measurement would allow much better understanding of the solver's performance as compared with experiment, as well as suggest at which instantaneous values of azimuth the solver prediction needs to improve. However, this requires a very high sampling rate for the experiment, which may be difficult to achieve.

Appendix A

Numerical Work on Cycloidal Wind Turbines

The first half of this appendix is to provide a comprehensive literature survey of the numerical work on vertical axis and cycloidal wind turbines. Background information on state-of-the-art simple analytical models and CFD analyses are described here, with the the express purpose that future work on this topic may be facilitated.

The latter half of this appendix is to present CFD validations with experiment performed within the scope of the current work.

A.1 Numerical Work in Literature on VAWT and CWT

A.1.1 Simple Analytical Models

Simplified numerical models of the VAWT have been developed by Paraschivoiu and Allet [51] and Mertens et al. [52]. Paraschivoiu and Allet used incidence delay

methods to obtain aerodynamic performance predictions of dynamic stall on Darrieus Wind Turbines and found that they correlate well the experimental data of Sheldahl for a 17-m Sandia Wind Turbine. Mertens et al. used a combination of axial momentum and blade element theory for an actuator plate representation of the rotor to develop a multiple stream-tube model of skewed flow over a roof-mounted H-Darrieus rotor. In addition, Reddy [53] used a multiple streamtube model with the standard blade element theory applied to each of the streamtubes to calculate the induced flow velocity on a Darrieus Wind Turbine. In turn, this was used to estimate the force on each of the rotor blade elements. He additionally explored the effects of changing geometrical parameters such as blade solidity and rotor height-to-diameter ratios, as well as studied the transient behavior of the rotor for a step change in wind speed or torque output.

A.1.2 CFD Simulations

Early CFD work on the VAWT was performed by Rajagopalan and Fanucci [54], who used control volumes in cylindrical coordinates to map the computational domain and modeled the turbine blades using a 2-D porous cylindrical shell; a finite difference procedure was employed to solve the conservation of mass and momentum equations. Allet et al. [55] numerically investigated the 2-D unsteady flow around a NACA 0015 airfoil undergoing Darrieus rotational motion using an incompressible Navier-Stokes solver with a Streamline Upwind Petrov-Galerkin finite element method for discretization of the spatial terms. Ferreira et al. [48] simulated dynamic stall on the blades of a 2-D straight-bladed H-Darrieus VAWT and achieved validation of the results through comparison with experimental measurements of blade loads and vorticity. Takahashi et al. [10]

used Direct Numerical Simulation (DNS) to model their VAWT experimental setup and found that the results showed somewhat reasonable correlation with experiment, though had difficulty predicting the exact trend of power coefficient vs. TSR. Horiuchi et al. [56] investigated the flowfield around a VAWT using Detached-Eddy Simulation with STAR-CD and examined the velocity profiles at different locations downstream of the rotor. Numerical analysis for the cycloidal rotor has been limited to the work of Hwang et al. [57], who used the STAR-CD compressible flow solver to assess the pitch and phase angles for optimum power generation on the cycloidal wind turbine.

A.1.3 Other Numerical Studies

Optimization studies have been performed to find the ideal pitching motion which maximizes power generation on each blade as it travels around the azimuth of the VAWT configurations. Paraschivoiu et al. [58] equated forces obtained from blade element theory with actuator disk theory to iteratively converge upon coefficients for a sinusoidal equation which describes optimal pitch for a prescribed wind condition. Staelens et al. [59] expounded upon this previous work to realize a sinusoidal function of local blade angle of attack that improved power output while being mechanically feasible to implement.

A.2 Preliminary CFD Validation in the Current Work

A CFD validation for the CWT was performed in the scope of the current work. The TURNS code was previously validated against the VAWT PIV results and

force coefficients obtained by Ferreira et al. [8], as shown earlier in section 3.3. For the CWT, the results of Hwang et al. [57] were used to examine the predictive capabilities for unsteady time force history, as will be discussed in detail below.

A.2.1 Cycloidal Wind Turbine Validation

Due to the scarcity of experimental results in literature for a CWT, the numerical results of Hwang et al. were used to verify the predictive accuracy of OVERTURNS. However, these do not have experimental validation. The pitching motion of Hwang's CWT is expressed through a pure sinusoidal variation represented by the equation:

$$\theta = \theta_{max} \sin(\Psi - \phi_e) \tag{A.1}$$

where ϕ_e represents the angle of eccentricity of the offset (i.e. phase angle), θ_{max} indicates the pitch amplitude, and Ψ denotes the position of the blade around the azimuth, equal to the product of the total time elapsed and the rotational rate. The CWT setup is extremely similar to the schematic of the cycloidal rotor shown in Figure 1.1.

Hwang et al. conducted numerical experiments for a four-bladed cycloidal wind turbine using a symmetric NACA 0018 airfoil with a 0.45 m chord, a rotational-radius-to-chord ratio of 3.56 and a span -to-chord ratio of 4.44. MSC/ PATRAN Command Language (a general purpose software for 3D geometry creation and grid generation) was used to generate a structured 8-node hexahedral mesh. STAR-CD was employed with a $k - \varepsilon$ high Reynolds turbulence model to run this case. The optimum scenario for power generation as determined by Hwang et al. was at a freestream wind speed of 13 m/s and a blade-tip speed

to wind-speed ratio of 2, which corresponds to the freestream Mach, blade tip Mach, and Reynolds numbers of 0.038, 0.076, and 1.125×10^6, respectively. The optimum pitch angle was 8° and the phase angle 0°. For verification, OVERTURNS was run with these optimal parameters using four blade meshes and a circular background mesh (shown in Figure A.1(b) in a similar manner as presented above for the vertical axis wind turbine case. The Baldwin-Lomax turbulence model was used to determine eddy viscosity in this highly dynamic flow environment.

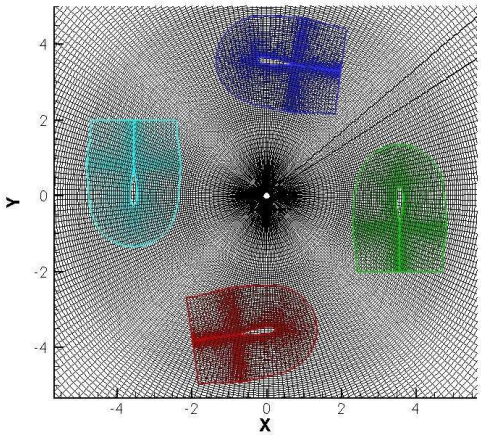

Figure A.1: Computational Mesh for the Cycloidal Axis Wind Turbine

A.2.2 Tangential Force Comparison

Figure 3 compares the results of tangential force obtained from OVERTURNS with those calculated by Hwang et al. for one blade and the entire rotor. For the single blade on Figure A.2(a), OVERTURNS predicts the global maximum and minimum very well for the tangential force and captures the general trend of the STAR-CD simulation. There is a phase shift of approximately 10°, however, immediately past the initial peak value between the azimuthal angles of $\Psi = 90°$

to $\Psi = 180°$. Figure A.2(b) presents the tangential force summed over all blades. The mean value from the OVERTURNS results is within 5% of Hwang et al.'s results. The OVERTURNS solution has a phase lag of about 45° with respect to Hwang's results, and only predicts about three-quarters the amplitude of unsteadiness. Overall, though, the OVERTURNS results capture the magnitude and behavior of Hwang et al.'s results well.

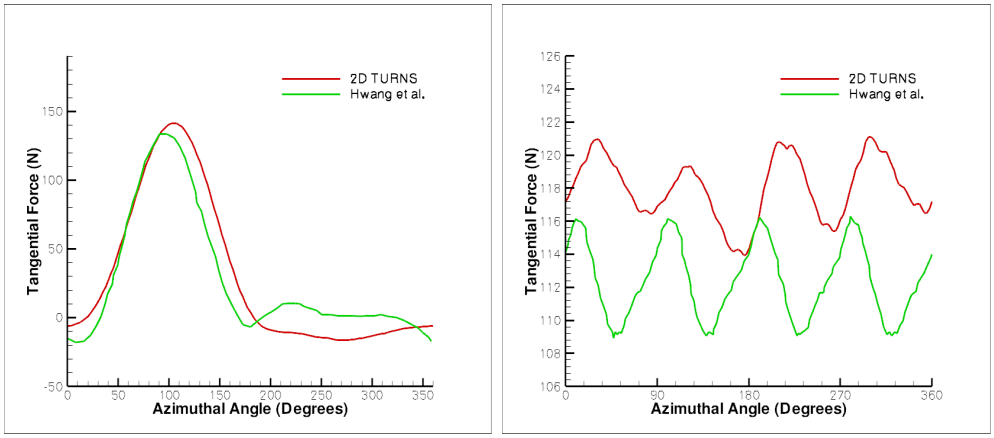

(a) Tangential force of each blade (b) Tangential force of the rotor

Figure A.2: Comparison of OVERTURNS and Hwang et al. for tangential force generated by the cycloidal wind turbine

While the unsteady results of tangential force correlate well with literature, further TURNS validation via a TSR sweep similar to the RPM sweep conducted for the cyclocopter in Section 4.4 revealed deficiencies in the predictive accuracy of the flow solver. While Hwang predicts a drop in the power-generating capacity of the CWT past a TSR of 2, analogous to the drop for VAWTs seen by Takao et al. [9] and Takahashi et al. [10], OVERTURNS does not predict this. Instead, it predicts a continued and indefinite increase in power-generating capacity with continually increasing TSR. The occurrence of these unphysical solutions from TURNS may be due to an incorrect fully turbulent assumption for the CWT,

or due to TURNS' inability to capture separated flow. Further investigation is needed into this issue, possibly with the future implementation of a transition model into TURNS.

A.2.3 Summary

In this appendix, it was seen that experimental as well as numerical investigation into the performance of VAWTs and CWTs is still relatively limited. Though certain preliminary studies have been performed to predict the aerodynamic forces on VAWTs, there have been no comprehensive insights into the flow physics of the VAWT or CWT in literature. Preliminary CFD studies by the current work into the performance of the CWT show that while TURNS can qualitatively visualize the flowfield well and capture the unsteady aerodynamics for low tip speed ratios, the CFD predictions become unphysical with higher TSRs. Much future work remains for modifying the flow solver to generate accurate predictions of the VAWT flowfield, and VAWTs and CWTs continue to be a largely unexplored area of potential research.

Appendix B

CFD Simulation of an Unsteady Pitching Airfoil at Low Reynolds Numbers

Unsteady lift, drag, and moment coefficient results were obtained for the NACA 0010 airfoil for pitching amplitudes of 0-30 with respect to freestream conditions of $Re = 30,000$ and $M_\infty = 0.047$ at increments of 5°, as consistent with the experimental setup of Benedict et al. However, these are merely CFD predictions and do not have any experimental validation. The results for coefficient of lift, drag, and moment at quarter-chord position for pitch amplitude of 30° are presented in Figure B.1.

From the plots, distinct changes in the flow can be noted through their effect on lift, drag, and moment, and through examination of the pressure contours over the airfoil. As the airfoil pitches up from zero degrees, there is a somewhat steady rise of C_l, C_d, and a small drop followed by a region of constant C_m from $0 - 23°$ due to the formation of low pressure suction peak at the leading edge on the upper surface and a high pressure stagnation region on the lower

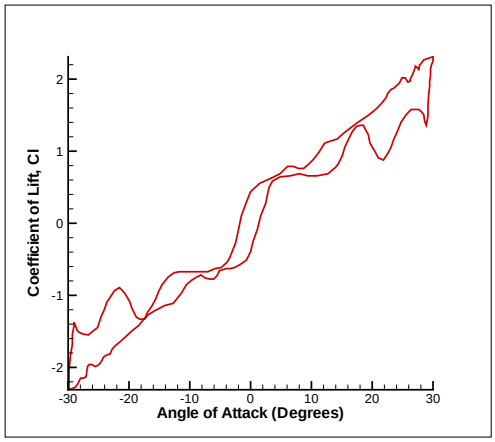

(a) Coefficient of Lift, C_l

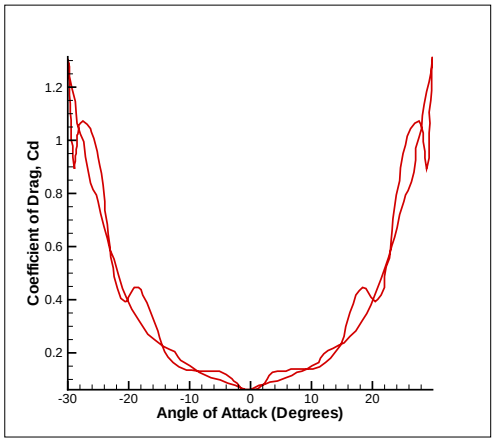

(b) Coefficient of Drag, C_d

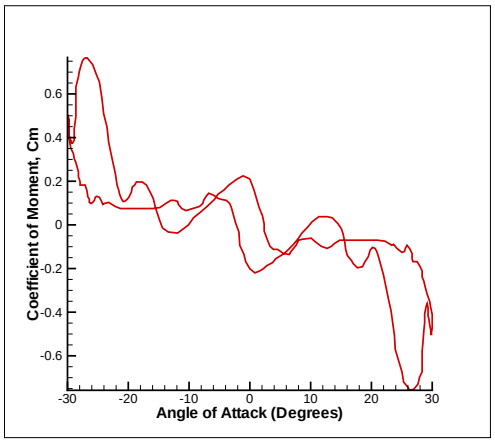

(c) Coefficient of Moment, C_m

Figure B.1: Unsteady pitching NACA 0010 airfoil time histories at $Re = 30,000$, $M_\infty = 0.047$

surface. As the airfoil pitches from $23 - 30°$, the rollup and detachment of the leading edge vortex leads to oscillations in C_l, large increases in C_d and steady decrease of C_m nose-down. From $30 - 27°$ pitching down, a large vortex is shed from the upper surface at around 3/4-chord. There is also the formation of a small, albeit strong vortex at the trailing edge of the airfoil, and the interaction between these two vortices leads to a sharp drop in C_l, C_d, and C_m (nose-down pitching moment). From $27 - 4°$ pitching down, the intensification of the vortex formed on the trailing edge at 27°, and the large region of low pressure formed by the shedding of this vortex which extends from 3/4-chord position downstream, leads to decrease in C_l and C_d with large oscillations, and a nose-up C_m. From $-4°$ to $4°$ pitch down, the shedding of this low pressure region and its interaction with other small vortices that form on the trailing edge leads to a drop in C_l, somewhat constant C_d and another nose-up pitching moment. The rest of the lower pitching cycle from $-4°$ to $-30°$ back to $0°$ is a repetition of the upper pitching cycle on the lower surface.

Appendix C

A New Background Grid for Resolution of the Cycloidal Rotor Wake

A $321 \times 151 \times 151$ background grid which was designed to capture more detailed flow phenomena in the wake is described here. Though all of the cycloidal rotor simulations in this work used a simple algebraic cylindrical background mesh, implementation of the current mesh may be desirable for future work.

Figure C.1 shows the 3-D cylindrical mesh. For the spanwise $y-z$ planes, A region of even point distribution is clustered near the blade up to one chord length away from each blade tip; then, Vinokur stretching is employed to determine point distribution to the farfield. For the $x-y$ planes, a circular geometry is meshed for the "top" of the background mesh (with respect to the orientation of the cage); a trapezoidal geometry exists at the "bottom" of background mesh. Relatively even clustering is concentrated in both the rotor cage and the wake region below the cage, allowing for better preservation of the vortices shed from the blades. The numerical implementation of this geometry is detailed below.

In Figure C.2(a), a completed $x-y$ plane of the mesh is seen. Figure C.2(b) shows each section that was generated separately of the others before being

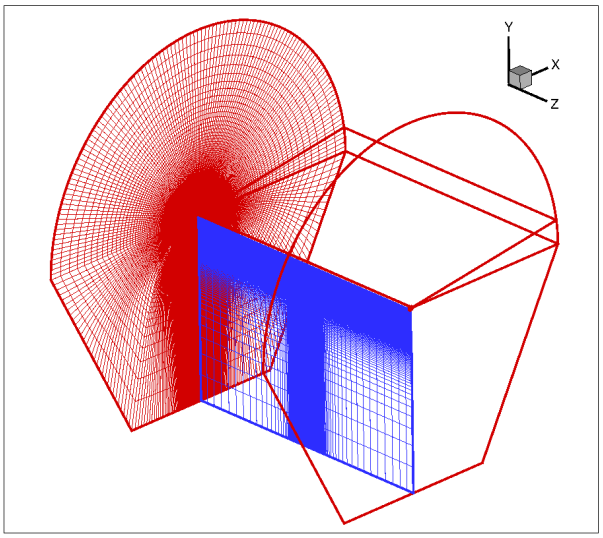

Figure C.1: The new 3-D background mesh showing both an $x-y$ and a $y-z$ planar section.

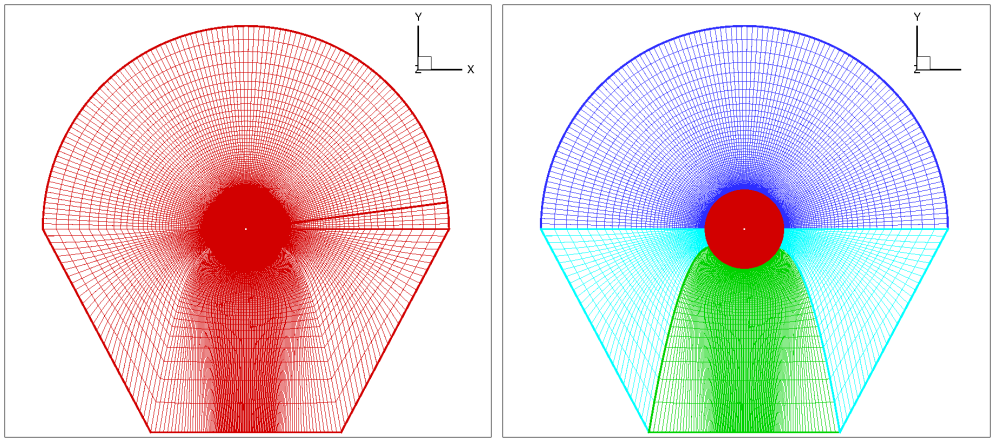

(a) A complete $x-y$ plane.

(b) An $x-y$ plane showing separate sections meshed by different grid generation methods.

Figure C.2: $x-y$ plane section of the new background mesh.

integrated into the framework of the entire mesh geometry. In this figure, the "center" rotor cage region (in red) was generated completely using an algebraic distribution with constant spacing in both the tangential and radial directions, such that all the flow features near the rotor cage could be captured to a high resolution and accuracy. The upper cylindrical region (in blue) was generated using even algebraic spacing in the spanwise direction and Vinokur stretching in the radial direction. For the lower trapezoidal distribution, the parabolic boundary between the lower side regions (in cyan) and the lower center region (in green) was determined using a least squares fit through a number of points as prescribed by the user. Thus, the lower center region is variable in size and can be enlarged or compressed based on the cycloidal rotor case of interest. The points along the radial direction of the parabolic line, as well as the clustering at the bottom of the lower center region, were distributed using Vinokur stretching. For all the mesh points within the lower side regions and the lower center region, a crude algebraic distribution was first generated. Then, Poisson-based elliptic grid generation method was used to provide a smooth distribution for the interior nodal points, given the boundary point distribution. More information on elliptic grid generation can be found in Thompson [26].

Bibliography

[1] Sachse, H., "Kirsten-Boeing Propeller," Technical Memorandum no. 351, NACA, 1926.

[2] Strandgren, C. B., "The Theory of the Strandgren Cyclogiro," Technical Memorandum no. 727, NACA, 1933.

[3] Wheatley, J. B., "Simplified Analysis of the Cyclogyro Rotating Wing System," Report no. 467, NACA, 1933.

[4] Wheatley, J. B. and Windler, R., "Wind Tunnel Tests of a Cyclogiro Rotor," Technical Note no. 528, NACA, 1935.

[5] Darrieus, G. J. M., "Turbine Having its Rotating Shaft Transverse to the Flow of the Current," *U.S. Patent no. 1,835,018*, 1931.

[6] Sheldahl, R. E., "Comparison of Field and Wind Tunnel Darrieus Wind Turbine Data," Report SAND80-2469, Sandia National Laboratories, Aerothermodynamics Division, Sandia National Laboratories, Albuquerque, New Mexico, 1981.

[7] Sheldahl, R. E. and Klimas, P. C., "Aerodynamic Characteristics of Seven Symmetrical Airfoil Sections Through 180-Degree Angle of Attack for Use in

Aerodynamic Analysis of Vertical Axis Wind Turbines," Report SAND80-2114, Sandia National Laboratories, Albuquerque, New Mexico, 1981.

[8] Ferreira, C. S., van Bussel, G., and van Kuik, G., "2D PIV Visualization of Dynamic Stall on a Vertical Axis Wind Turbine," *45th AIAA Aerospace Sciences Meeting and Exhibit*, No. AIAA 2007-1366, Reno, NV, Jul. 2007.

[9] Takao, M. et al., "Experimental Study of a Straight-Bladed Vertical Axis Wind Turbine with a Directed Guide Vane Row," *Proceedings of the 28th International Conference on Ocean, Offshore, and Arctic Engineering*, Honolulu, HI, Jun. 2009.

[10] Takahashi, S., Ohya, Y., Takashi, K., and Watanabe, K., "Numerical and Experimental Studies of Airfoils Suitable for Vertical Axis Wind Turbines and an Application of Wind-Energy Collecting Structure for Higher Performance," *The Fourth International Symposium on Computational Wind Engineering (CWE 2006)*, Yokohama, Japan, 2006, pp. 327–330.

[11] Kiwata, T. et al., "Performance of a Vertical Axis Wind Turbine with Variable-Pitch Straight Blades using a Linkage Mechanism," *Journal of Environment and Engineering*, Vol. 5, No. 1, 2010, pp. 213–225.

[12] Hwang, I. et al., "Experimental Investigation of VTOL UAV Cyclocopter with Four Rotors," *48th AIAA/ASME/ASCE/AHS/ASC Structures, Structural Dynamics, and Material Conference*, No. AIAA 2007-2247, Honolulu, HI, Apr. 23–26 2007.

[13] Yu, H., Bin, L. K., and Rong, H. W., "The Research on the Performance of Cyclogiro," *6th AIAA Aviation Technology, Integration, and Operations Conference*, No. AIAA 2006-7704, Wichita, KS, Sep. 25–27 2006.

[14] Benedict, M., Ramasamy, M., Chopra, I., and Leishman, J. G., "Experiments on the Optimization of MAV-Scale Cycloidal Rotor Characteristics towards Improving their Aerodynamic Performance," *American Helicopter Society International Specialists Meeting on Unmanned Rotorcraft*, Phoenix, AZ, Jan. 20–22 2009.

[15] Benedict, M., Jarugumilli, T., and Chopra, I., "Design and Development of a Hover-Capable Cyclocopter Micro Air Vehicle," *American Helicopter Society 65th Annual Forum*, Grapevine, TX, May 27–29 2009.

[16] Benedict, M., Jarugumilli, T., and Chopra, I., "Experimental Performance Optimization of a MAV-Scale Cycloidal Rotor," *Proceedings of the AHS Specialists' Meeting on Aeromechanics*, San Francisco, CA, Jan 20–22 2010.

[17] Yun, C. Y. et al., "A New VTOL UAV Cyclocopter with Cycloidal Blades System," *American Helicopter Society 60th Annual Forum*, Baltimore, MD, June 7–10 2004.

[18] McNabb, M. L., *Development of a Cycloidal Propulsion Computer Model and Comparison with Experiment*, Masters Thesis, Mississippi State University, Department of Aerospace Engineering, December 2001.

[19] Garrick, I. E., "Propulsion of a Flapping and Oscillating Airfoil," Report no. 567, NACA, 1937.

[20] Parsons, E., *Investigation and Characterization of a Cycloidal Rotor for Application to a Micro-Air Vehicle*, Masters Thesis, University of Maryland, Department of Aerospace Engineering, 2005.

[21] Benedict, M., Mattaboni, M., Chopra, I., and Masarati, P., "Aeroelastic Analysis of a MAV-Scale Cycloidal Rotor," *Proceedings of the 51st AIAA/ASME/ASCE/AHS/ASC Structures, Structural Dynamics, and Materials Conference*, Orlando, FL, Apr. 12–15 2010.

[22] Iosilevskii, G. and Levy, Y., "Experimental and Numerical Study of Cyclogiro Aerodynamics," *AIAA Journal*, Vol. 44, No. 12, 2006, pp. 2866–2870.

[23] Lakshminarayan, V. K. and Baeder, J. D., "High Resolution Computational Investigation of Trimmed Coaxial Rotor Aerodynamics in Hover," *Journal of the American Helicopter Society*, Vol. 54, No. 4, 2009, pp. 042008–1 – 042008–21.

[24] Lakshminarayan, V. K., *Computational Investigation of Micro-Scale Coaxial Rotor Aerodynamics in Hover*, Ph.D. Dissertation, University of Maryland, Department of Aerospace Engineering, 2009.

[25] Vinokur, M., "On One-Dimensional Stretching Functions for Finite Difference Calculations," *Journal of Computational Physics*, Vol. 50, 1983, pp. 215–234.

[26] Thompson, J. F., Soni, B. K., and Weatherill, N. P., *Handbook of Grid Generation*, CRC Press, 1999.

[27] Thompson, J. F., *Aspects of Numerical Grid Generation - Current Science and Art*, Masters Thesis, Mississippi State University, NSF Engineering Research Center for Computational Field Simulation, 1993.

[28] Alsalihi, Z., "Two-Dimensional Hyperbolic Grid Generation," Technical Note 162, von Karman Institute for Fluid Dynamics, 1987.

[29] Cordova, J. Q. and Barth, T. J., "Grid Generation for General 2-D Regions Using Hyperbolic Equations," *26th AIAA Aerospace Sciences Meeting*, Reno, NV, Jan. 1988.

[30] Kinsey, D. W. and Barth, T. J., "Description of a Hyperbolic Grid Generating Procedure for Arbitrary Two-Dimensional Bodies," Technical Memorandum TM-84-191, Flight Dynamics Laboratory, Air Force Wright Aeronautical Laboratories, Wright-Patterson Air Force Base, 1984.

[31] Chan, W. M. and Steger, J. L., "A Generalized Scheme for Three-Dimensional Hyperbolic Grid Generation," *AIAA Paper 91-1588-CP*, 1991.

[32] Lee, Y., *On Overset Grid Connectivity and Automated Vortex Tracking in Rotorcraft*, Ph.D. Dissertation, University of Maryland, Department of Aerospace Engineering, 2008.

[33] Sitaraman, J., *CFD Based Unsteady Aerodynamic Modeling for Rotor Aeroelastic Analysis*, Ph.D. Dissertation, University of Maryland, Department of Aerospace Engineering, 2003.

[34] Hodges, D. H. and Dowell, E. H., "Nonlinear Equations of Motion for the Elastic Bending and Torsion of Twisted Nonuniform Rotor Blades," Technical Note D-7818, NASA, 1974.

[35] White, F. M., *Viscous Fluid Flow*, McGraw-Hill, Inc., New York, NY, 1991.

[36] Baldwin, B. S. and Lomax, H., "Thin Layer Approximation and Algebraic Model for Separated Turbulent Flows," *AIAA Paper 78-257*, 1978.

[37] Spalart, P. R. and Allmaras, S. R., "A One-equation Turbulence Model for Aerodynamic Flows," *30th AIAA Aerospace Sciences Meeting and Exhibit*, No. AIAA 1992-0439, Reno, NV, Jan. 1992.

[38] van Leer, B., "Towards the Ultimate Conservative Difference Scheme," *Journal of Computational Physics*, Vol. 32, No. 1, 1979, pp. 101–136.

[39] Roe, P. L., "Approximate Riemann Solvers, Parameter Vectors and Difference Schemes," *Journal of Computational Physics*, Vol. 135, No. 2, 1997, pp. 250–258.

[40] Turkel, E., "Preconditioning Techniques in Computational Fluid Dynamics," *Annual Review of Fluid Mechanics*, Vol. 31, 1999, pp. 385–416.

[41] Jameson, A., "Time Dependent Calculations Using Multigrid, with Applications to Unsteady Flows Past Airfoils and Wings," *AIAA Paper 91-1596*, 1991.

[42] Hirsch, C., *Numerical Computation of Internal and External Flows, Vol. 2*, Wiley Publishers, 1990.

[43] Pulliam, T. H. and Chaussee, D. S., "A Diagonal Form of an Implicit Approximate Factorization Algorithm," *Journal of Computational Physics*, Vol. 39, No. 2, Feb. 1981, pp. 347–363.

[44] Lutz, T., Wurz, W., and Wagner, S., "Numerical Optimization and Wind-Tunnel Testing of Low Reynolds Number Airfoils," *Fixed and Flapping Wing Aerodynamics for Micro Air Vehcile Applications*, edited by T. J. Mueller, AIAA, 2001, pp. 169–190.

[45] McAlister, K. W., Pucci, S. L., McCroskey, W. J., and Carr, L. W., "An Experimental Study of Dynamic Stall on Advanced Airfoil Sections, Pressure and Force Data," Technical Memorandum TM-84245, NASA, 1982.

[46] Tuncer, I. H., Wu, J. C., and Wang, C. M., "Theoretical and Numerical Studies of Oscillating Airfoils," *AIAA Journal*, Vol. 28, No. 9, 1990, pp. 1615 – 1624.

[47] Coene, R., "Elements of the Aerodynamic Theory of Cyclogyro Wing Systems with Concentrator Effects," Technical Report LR-338, Delft University of Technology - Aerospace Faculty, Delft, the Netherlands, Oct. 1983.

[48] Ferreira, C. S. et al., "2D CFD Simulation of Dynamic Stall on a Vertical Axis Wind Turbine: Verification and Validation with PIV Measurements," *45th AIAA Aerospace Sciences Meeting and Exhibit / ASME Wind Energy Symposium*, Reno, NV, Jan. 2007.

[49] Jeong, J. and Hussain, F., "On the Identification of a Vortex," *Journal of Fluid Mechanics*, Vol. 285, 1995, pp. 69–94.

[50] Leishman, J. G., *Principles of Helicopter Aerodynamics*, Cambridge University Press, New York, NY, 2006.

[51] Paraschivoiu, I. and Allet, A., "Aerodynamic Analysis of the Darrieus Wind Turbines Including Dynamic Stall Effects," *Journal of Propulsion and Power*, Vol. 4, No. 5, 1988, pp. 472–477.

[52] Mertens, S. et al., "Performance of a High Tip Speed Ratio H-Darrieus in the Skewed Flow on on a Roof," *41st AIAA Aerospace Sciences Meeting and Exhibit*, No. AIAA 2003-0523, Reno, NV, Jan. 2003.

[53] Reddy, G. B., *The Darrieus Wind Turbine: An Analytical Performance Study*, Masters Thesis, Texas Tech University, Department of Mechanical Engineering, 1976.

[54] Rajagopalan, R. and Fanucci, J., "Finite Difference Model for Vertical Axis Wind Turbines," *Journal of Propulsion and Power*, Vol. 1, No. 6, 1985, pp. 432–436.

[55] Allet, A. et al., "Numerical Simulation of Dynamic Stall Around an Airfoil in Darrieus Motion," *Journal of Solar Energy Engineering*, Vol. 121, Feb. 1999, pp. 69–76.

[56] Horiuchi, K., Ushiyama, I., and Kazuichi, S., "Straight Wing Vertical Axis Wind Turbines: A Flow Analysis," *Wind Engineering*, Vol. 29, No. 3, 2005, pp. 243–252.

[57] Hwang, I. S. et al., "Efficiency Improvement of a Cycloidal Wind Turbine by Active Control of Blade Motion," Tech. rep., School of Mechanical and Aerospace Engineering, Seoul National University, Seoul, Rep. of Korea, 2006.

[58] Paraschivoiu, I. et al., "H-Darrieus Wind Turbine with Blade Pitch Control," *International Journal of Rotating Machinery*, Vol. 2009, Article ID 505343, 2009.

[59] Staelens, Y. et al., "A Straight-Bladed Variable-Pitch VAWT Concept for Improved Power Generation," *41st AIAA Aerospace Sciences Meeting and Exhibit*, No. AIAA 2003-0524, Reno, NV, 2003.